UNIVERSITY OF CALIFORNIA

RIVERSIDE

# Development of Advanced Label-Free Optical Sensing with Novel Plasmonic Materials

A Dissertation submitted in partial satisfaction
of the requirements for the degree of

Doctor of Philosophy

In

Chemistry

By

Santino Nicholas Valiulis

December 2023

Dissertation Committee:

Dr. Quan Cheng, Chairperson

Dr. Ryan Julian

Dr. Haofei Zhang

The Dissertation of Santino Nicholas Valiulis is approved:

_____

_____

_____

Committee Chairperson

University of California, Riverside

**Acknowledgements**

I have been in higher education for the better part of my life. My time at UCR has been the most of it, and I say that with love as I couldn't have asked for a better place to get my PhD. When I was going to graduate from my undergraduate institution, I didn't know what I wanted to do in my life, let alone what type of chemistry I really wanted to end up doing. I decided to go to grad school as I figured more school couldn't hurt. At the same I was working in the lab of Dr. Frank Gomez, at CSULA, and there were two areas in his lab, biosensors and battery development, both focused on microfluidics. I applied to grad school thinking I wanted to do material science and ended up in lab who uses materials for biosensing purposes. I feel very lucky in where I ended up today. There's an innumerable amount of people with whom I want to thank.

Dr Jason Cheng, you've been my advisor for 7 years now. I sincerely could not have asked for anyone better. You taught me to be a scientist, how to think about research and always supported me. I always appreciated that you fostered a place where you treated your students as people first, it made me motivated to work for you as I always wanted to give you the quality of science you deserved. I will never forget the karaoke parties, I know we haven't had them in recent years but they were some of my favorite.

To my other committee members, Dr Ryan Julian I will always remember my first quarter at UCR taking your mass spectrometry class, I think about it fondly, and to Dr Haofei Zhang who the chair of my orals and committee and very supportive in that process.

To my lab mates. As currently the most senor student in the Cheng lab I've been around for a lot of them, so I'll keep it brief. Dr Pete Shanta, you sat behind me and taught me some of the early ropes of grad school and were always a kind voice. Dr Kelvin Tran, you taught me basically every instrument we had in lab, you had an encyclopedic knowledge of everything in the lab and I learned so much from you. Dr Zhengdong Yang, you are always so kind, I'll always remember the day you brought me Cane's chicken as you heard it was the most like KFC back home. Dr Bochao Li, we joined at the same time and you were always so kind and thoughtful. Dr Fatimah Abouhajar, it was wonderful working with you and thank you for being so kind. Dr Nor Akmaliza Rais, you always made me laugh and made the lab a brighter place. Dr Alexander Lambert, I was always honored to be your lab mate, and always appreciated it when you'd come to me to bounce ideas off. Dr Alexander Malinick, it's amazing to see your growth and your advice throughout the years has been invaluable. I'm glad to call you my friend. Daniel Stuart, my lunch buddy, whether we talked politics or science it was always a time I'll never regret.

To my parents, you've both been so supportive of my entire time in grad school. Mom, I can't thank you enough for how much you understood the trials and tribulations of being a grad student. Dad, I always appreciated how sincerely interested in what I was doing and talking to you about my research has made me better at communicating my science into laymen's terms.

To my friends, Sam, Giancarlo, and Elias. Thanks for always being there. Whenever I would disappear for a bit doing work you never gave me a hard time and

welcomed me back with open arms. Truly the best friends someone could ask for. Seeing you at my hooding ceremony was amazing.

To my wonderful girlfriend Monet, I know we only started dating towards the end of my PhD but your consistent support throughout this time has been a godsend. You're the best and I can't imagine life without you.

The Southern California LARP community you provided me with a wonderful hobby, and I cannot thank you enough.

To Dr Richard Maddox, you directed the EEP program which let me get into college early. Thank you for always believing in me.

Angela Madira, thanks for being one of my best friends throughout the years. I hope being a medical doctor treats you well.

My students throughout the years, thank you. Teaching is something I've always felt is satisfying. I learned so much through teaching and its an experience I feel so lucky to have had.

And to everyone else. Truly. Every interaction I've had has brought me here today and I am so happy with the person I am. Thank you.

## Copyright Acknowledgement

ABSTRACT OF THE DISSERTATION

Development of Advanced Label-Free Optical Sensing with Novel Plasmonic Materials

by

Santino Nicholas Valiulis

Doctor of Philosophy, Graduate Program in Chemistry
University of California, Riverside, December 2023
Dr. Quan Cheng, Chairperson

The development of biosensors provides effective tools for the study of life sciences and the improvement of human health. The capabilities of sensors are directly dependent on sensitivity and versatility built through smart designs. Biosensors are commonplace, including colorimentric COVID tests, electrochemical glucometers, and a variety of sensors allowing for tracking of blood oxygen level and sleeping habit. One particular technique, surface plasmon resonance (SPR), has found a broad range of usages as a label-free surface-based biosensor method with high sensitivity and real time detection, with SPR imaging further allowing for multiplexed detection. SPR has been used for kinetic analysis and drug binding assays, and relies upon the material underpinning the plasmonic effect. Further study of these materials and improvements of the plasmonic properties enhance SPR sensor technology. This Dissertation discusses theoretical and practical aspects of plasmonic sensors and the development of novel methodologies to improve the performance of SPR sensors and surface enhanced Raman spectroscopy, as well as their applications towards demanding biomedical measurement.

Chapters 2, 3 and 4 focus on the development of aluminum based plasmonic sensing and the use of thin film and Kretschmann configuration for SPR measurement, which has not been previously explored as compared to the standard metal gold. Chapter 2 focuses on characterizing the fundamental optical properties of aluminum and aluminum oxide for usage as SPR sensors. Novel plasmonic behavior could be achieved with formation of an oxide waveguide that demonstrates specific sensitivity to surface and bulk changes, allowing for understanding and quantification of any surface binding events. Chapter 3 applies the confirmed concepts of the previous chapter towards a focused approach with existing SPR instrumentation, including surface characterization of aluminum thin films, and experimental confirmation of high sensitivity performance as compared to the standard gold counterpart. Chapter 4 sees the usage of the thin film aluminum substrate as an SPR biosensor in the detection of an anti-myelin associated glycoprotein, an antibody that is associated with autoimmune induced neuropathy. Chapter 5 takes a different approach to plasmonic sensors, with the fabrication of self-assembled gold nanoparticles at a liquid-liquid interface, which has been demonstrated as a SERS enhancement surface in the detection of environmental pollutants.

## TABLE OF CONTENTS

**List of Figures**

# Chapter 1 Introduction and Background

## 1.1 Introduction

Plasmonic materials have showed a variety of sensing capabilities due to their unique electrical and chemical properties. As work has progressed towards the development of higher quality sensing systems, there have been two main approaches, analyte capture and fundamental material changes. Plasmonic sensors are only as good as the substrate they are made with and as such furthering the materials used both in type and application is a key part of sensor development and furthering the field. Novel plasmonic materials discussed in this writing will demonstrate strides taken in SPR and SERS sensing. Notably, a new material in SPR that competes with the standard gold films and methods in which consistent and sensitive SERS substrates are fabricated using benchtop techniques. In this chapter the field of plasmonic sensors and the various associated fields will be discussed to contextualize the work presented later.

## 1.2 Theoretical Basis of Plasmonics

Plasmons are the oscillations of the electron cloud of a material, most commonly a metal, and are associated with the function of the material to absorb and reflect varying frequencies of light. When this effect is coupled to an incident light source the plasmons on the surface of the material form a surface plasmon polariton (SPP). The SPP is sensitive to the environment which surrounds it, and through taking advantage of this information can be elucidated of a surface. This function can be used in a variety of ways which will be discussed in this work, and therefore a fundamental understanding of the formation and

propagation of the SPP's is necessary. In addition, the adoption of SPP's for a series of techniques is discussed in specifics as these will be used in multiple chapters of this work.

### 1.2.1 Total Internal Reflection and Evanescent Waves

Plasmonic absorption interacts with light in a multitude of ways and is dependent upon the angle and frequency of the incident light. [1, 2] To measure the plasmonic absorption, light is measured in either a transmission or reflection mode, to best match the specific system, and the resonances present. This can be applied to a variety of techniques including but not limited to surface enhanced Raman scattering as well as, surface enhanced fluorescence and extraordinary optical transmission. [3-6] SPR most commonly involved a reflection mode in a total internal reflection (TIR) arrangement, wherein the incident light is reflected at the interface of two mediums with differing refractive indexes, $n_1$ and $n_2$. At the critical angle, the light will undergo TIR and little to no light will be transmitted or refracted. The critical angle is defined by[7]:

$$\theta_c = \sin^{-1}\left(\frac{n_2}{n_1}\right) \quad (1.1)$$

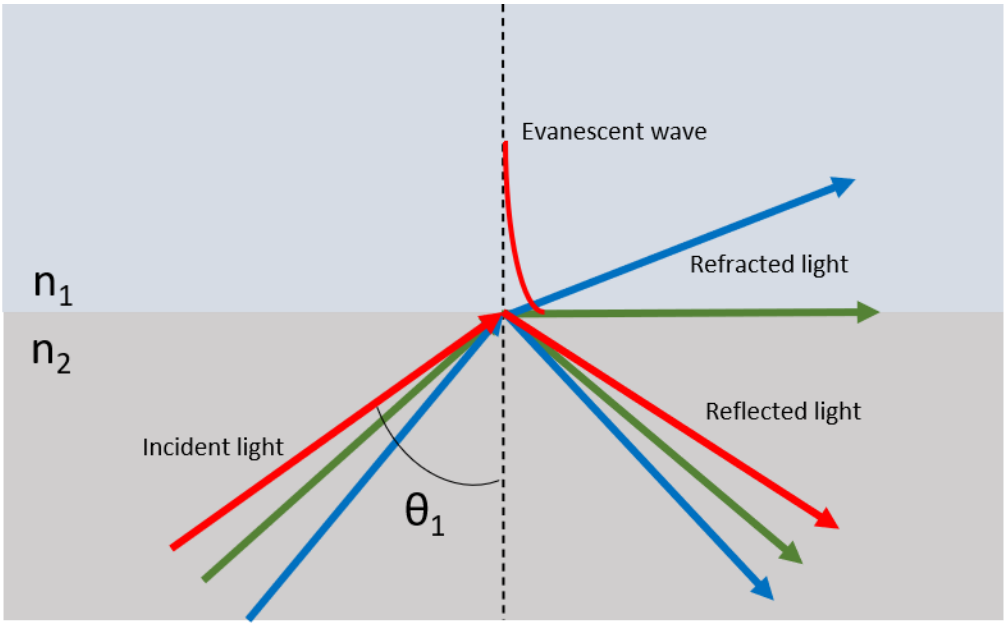


Figure 1.1: Reflection and refraction of light, dependent upon the incident angle.

When this feature is taken advantage of in an analytical context, $n_1$ is the material of analytical interest, and $n_2$ is frequently a high refractive index material. TIR is most frequently seen in fiber optic technologies, wherein light is transmitted long distances with relatively little loss due to this effect.[8] When the light performs TIR, an evanescent field of oscillating electrons is formed at the $n_1$ surface. The amplitude of the waves decays exponentially and can be described through the wave vector of the evanescent field, $k_{ev}$. The equation to solve for $k_{ev}$ is as follows[9]:

$$k_{ev} = \frac{\omega}{c}\sqrt{\varepsilon_p}\sin\theta \qquad (1.2)$$

Where c and ω are the speed of light in a vacuum and the angular frequency of the light respectively. Alternatively, the equation $2\pi c = \lambda\omega$ can be used. If the media is

assumed to be non-dispersive the refractive index is the square root of the permittivity ε. Therefore, the equation can be arranged to form:

$$k_{ev} = \frac{2\pi}{\lambda} n \sin\theta \qquad (1.3)$$

The penetration depth of the evanescent field can then be described in terms of the wavelength of the incident light and is frequently defined as λ/2. The critical angle is dependent on both refractive indexes of the respective materials, and so changes to the refractive index can be seen through a change in the critical angle. A variety of optical and electrical materials can be used to sense changes outside the surface as the matching conditions change in which the critical angle is formed. Commonly this is found in waveguide-based fiber optic sensors. [10, 11]

### 1.2.2 Surface Plasmon Resonances

When the previously described TIR effect occurs as the interface between a high refractive index dielectric, frequently a prism, and a metal surface, surface plasmons are formed. Akin to the evanescent field generated under TIR conditions, surface plasmons arise as an oscillating electron cloud present in the conducting band of the metal at the opposite interface of the metal and dielectric coupler. Surface plasmons can be mathematically predicted through applications of Maxwell's equations for material surfaces. The effect was first predicted in 1957[12] and was subsequently experimentally verified in 1959.[13] However, technological limitation inherent to the material necessities of the system prevented widespread usage until the 1980's. For SPR to occur, the electrons

in the conducting band of the metal are excited through the momentum transfer of an incident photon with specific energy and momentum. Photons of this specific nature are absorbed and are therefore not reflected under the TIR conditions in which SPR occurs. This causes a distinct gap in the reflected light spectrum known as the plasmonic dip, at angle greater than the critical TIR angle. This can be predicted through the Fresnel equations which require the empirically determined real and imaginary portions of the refractive index denoted by *n* and *k* respectively. The multilayer Fresnel equations can be used to model a two-layer system with the following equations[14]:

$$r_s = \frac{\boldsymbol{n}_1 \cos\theta_i - \boldsymbol{n}_2 \cos\theta_t}{\boldsymbol{n}_1 \cos\theta_i + \boldsymbol{n}_2 \cos\theta_t} \qquad (1.4)$$

$$r_p = \frac{\boldsymbol{n}_2 \cos\theta_i - \boldsymbol{n}_1 \cos\theta_t}{\boldsymbol{n}_2 \cos\theta_i + \boldsymbol{n}_1 \cos\theta_t} \qquad (1.5)$$

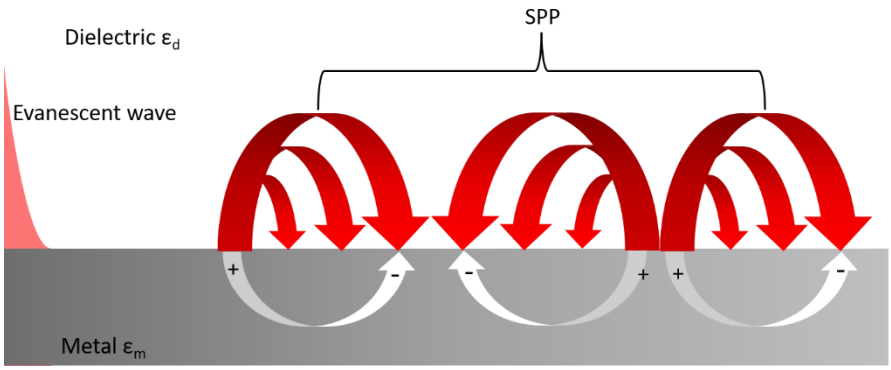


**Figure 1.2**: The formation of the SPP at the dielectric/metal interface when excited with incident light

In these equations $\boldsymbol{n}$ represents both the real and imaginary parts of the refractive index (as $\boldsymbol{n} = n + ik$), and $r_s$ and $r_p$ represent the differing conditions provided by either s or p-polarized light respectively. As additional layers are added to the Fresnel systems the

equations become increasingly complex. The source of *n* and *k* values of a material can found through the Lorentz-Drude model of electron transport.[15] Based upon this the reflectivity of a given material can be calculated independent of the incident angle based upon this equation:

$$R = \frac{(n-1)^2+k^2}{(n+1)^2+k^2} \qquad (1.6)$$

The *n* and *k* values themselves can be determined based upon the material's relative permittivity ($\epsilon_i$ and $\epsilon_r$) and relative magnetic permeability ($\mu_r$).

$$n = \sqrt{\frac{\mu_r}{2}\left(\sqrt{\epsilon_r^2 + \epsilon_i^2} + \epsilon_r\right)} \qquad (1.7)$$

$$k = \sqrt{\frac{\mu_r}{2}\left(\sqrt{\epsilon_r^2 + \epsilon_i^2} - \epsilon_r\right)} \qquad (1.8)$$

Most metals that are commonly used as plasmonic materials (Au, Ag, Cu, Al, Ti, Pt, etc.) are not ferromagnetic and so it is assumed that the $\mu_r \approx 1$. Furthermore, the permittivity is determined based upon the frequency of the incident light, the metal plasma frequency, and the metal damping frequency, represented by $\omega$, $\omega_p$ and $\Gamma$ respectively.

$$\epsilon_r = 1 - \frac{\omega_p^2}{\omega^2+\Gamma^2} \quad (1.9) \qquad \epsilon_i = \frac{\omega_p^2\Gamma}{\omega(\omega^2+\Gamma^2)} \quad (1.10)$$

The plasma frequency of a materials is a fundamental physical property and is the property that most strongly correlates to the function of a materials plasmonic capabilities and is defined by:

$$\omega_p^2 = \frac{Ne^2}{m\epsilon_0} \qquad (1.11)$$

In this equation N is the free electron density of the metal, *e* and *m* are the charge and mass of an electron respectively and $\epsilon_0$ is the permittivity of free space. Therefore, the function of a plasmonic material is mostly dependent on the free electron density.

### 1.2.3 Surface Plasmon Resonance Spectroscopy

When the plasmonic material is a thin film of metal, the plasmonic absorption is induced based upon the coupling of the evanescent field generated by TIR and plasmonic excitation state of the surface. These form what is referred to as a surface plasmon polariton (SPP) which is a propagating wave along the surface. The wave vector of an SPP can be described by[1]:

$$k_{sp} = \frac{\omega}{c}\sqrt{\frac{\varepsilon_{mr}\varepsilon_s}{\varepsilon_{mr}+\varepsilon_s}} \qquad (1.12)$$

When the $k_{sp}$ matched the $k_{ev}$ of the incident photon, the photon is absorbed into the SPP. As the refractive index at the surface shifts, the angle or wavelength at which the coupling occurs to form the SPP changes. Tracking the change in the angle or wavelength at which the SPP is formed is the basis of SPR spectroscopy.

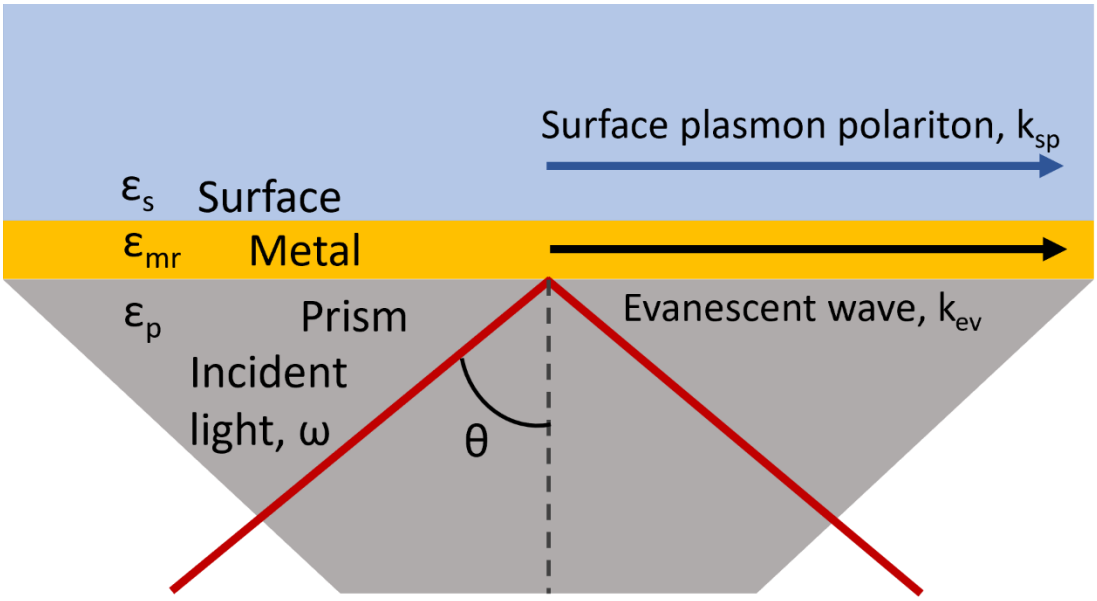


**Figure 1.3** The Krestchmann configuration of an SPR instrument in cartoon form.

SPR instruments most commonly use the Krestchmann configuration, which is an attenuated total reflection arrangement, first proposed in 1968.[16] In this system, the plasmonic material is in contact with the prism and the analyte material of interest. The light source, either an LED or laser, is aimed at a desired angle, and either the wavelength or angle is scanned through to determine the SPP coupling conditions. In an angle scanning setup, either the incident angle is changed through rotation of the prism or light source relative to each other, or the reflected angle is measured using a photodiode array which generates the similar spacial information. In a wavelength scanning instrument, a broadband white light source is used, and a refraction grading separates the reflected light into the measured spectra. Fiber optic SPR is another configuration based upon the Krestchmann configuration in which the metallic thin film is deposited on a waveguide material.[17] This allows for both the incident light and signal to be drawn out in a small

space. This method has practicality as the fiber optic cable can be used as a probe to dip into solutions of interest.[18] However, the system is sensitive to mechanical changes in the probe as the plasmonic response is very sensitive to environmental changes, so control is necessary to isolate analyte response.[19]

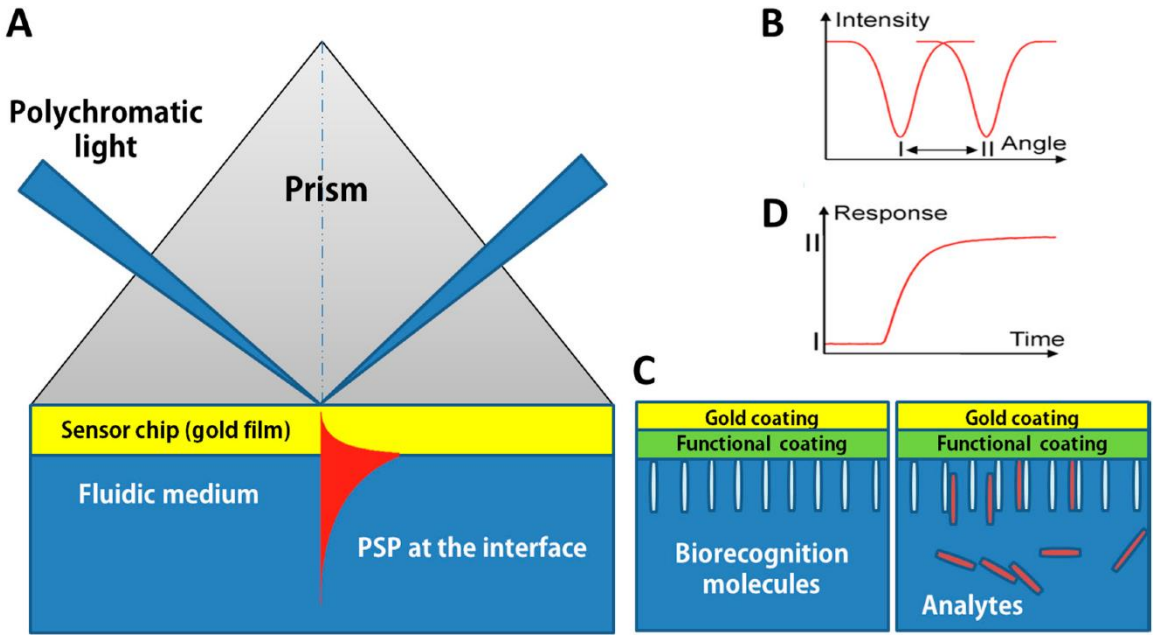


**Figure 1.4** A cartoon demonstration of an SPR instrument and the readout from said instrument demonstrated in the reflectivity curve and sensogram. [22]

Data is experimentally collected as a sensogram shown in Figure 1.4 as a change in the environment surrounding the metallic surface caused a change in the matching conditions of the SPP.[21, 22] The minimum reflected intensity, is tracked as this occurs and the change in angle or wavelength is tracked over time. The shift in the sensogram is correlative to the change in refractive index, and a linear relationship can be determined between the two. [23] Similarly, SPR can be used to determine the thickness and absolute

mass of a dielectric material on the metal surface. [24-26] This is determined based upon the following relationship:

$$R = m(\eta_a - \eta_s)[1 - e^{-\frac{2d}{l_d}}] \qquad (1.13)$$

Wherein R is the reflected signal, m is the sensitivity over small refractive index (RI) increments, ηa is the RI of the adsorbed layer, ηs is the RI of the overall solution, d is the layer thickness, and ld is the decay length of the evanescent field, which is determined based upon the wavelength of the incident light [27].

### 1.2.4 Localized Surface Plasmon Resonance

When the wavelength of the incident light is greater than any dimensions of a plasmonic material, the plasmon oscillates around the nanomaterial instead of propagating.[28] This is referred to as localized surface plasmon resonance or LSPR. The difference in this effect compared to SPR can be seen in Figure 1.5. By ascribing Mie theory as well as Maxwell's equations to this system the electromagnetic field surrounding a metallic nanoparticle can be approximated with[29]:

$$E_{out}(x, y, x) = E_0\hat{z} - \left[\frac{\varepsilon_{in} - \varepsilon_{out}}{\varepsilon_{in} + 2\varepsilon_{out}}\right] a^3 E_0 [\frac{\hat{z}}{r^3} - \frac{3z}{r^5}(x\hat{x} + y\hat{y} + z\hat{z})] \qquad (1.14)$$

Wherein this equation $\varepsilon_{in}$ is the dielectric constant of the metal nanoparticle, and $\varepsilon_{out}$ is the dielectric constant of the surrounding environment. This describes the necessary dielectric constants to produce maximal field enhancement. This occurs when the $\varepsilon_{in}$ value approaches $-2\varepsilon_{out}$. Metals such as gold have an $\varepsilon_{in}$ that is close to this value and so they produce a large EM field. Additional characteristics of the plasmon excitation band can be

found based upon the extinction cross section, $C_{ext}$, which is given by the following equation:

$$C_{ext} = \frac{24\pi^2 a^3 \varepsilon_{out}^{3/2} N}{\lambda \ln(10)} \frac{\varepsilon_i}{(\varepsilon_i + \chi\varepsilon_{out})^2 + \varepsilon_i^2} \qquad (1.15)$$

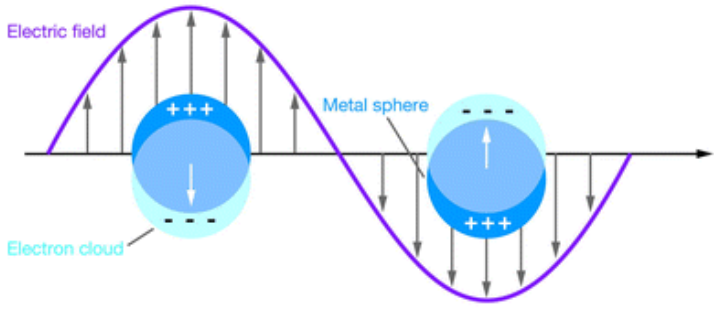


**Figure 1.5** A cartoon demonstration of the localized surface plasmon. [20]

Wherein ε is the complex dielectric constant of the bulk material, N is the electron density and χ is used to dictate the geometry of the nanostructure, with increasing number indicating a more complex geometry.[30] Therefore, the geometry of the nanostructures as well as the material used play a pivotal role in plasmonic enhancement. Similarly, to SPR, LSPR is also sensitive to the refractive index of the surroundings following this $\Delta\lambda = m\Delta n[1 - e^{-\frac{2d}{l_d}}]$ (1.16)

Where m is the bulk refractive index response of the nanoparticles, Δn is the change in refractive index at the surface, d is the thickness of the material, and $l_d$ is the decay length. Contrary to SPR, wherein the decay length of the plasmonic field is relatively far

(~300 nm) LSPR possesses a shorter decay length on the order <40 nm. This allows for specificity to changes close to the surface.[31] As current methodologies to develop nanostructure become more ubiquitous, through synthetic and lithographic methods, more applications have been looked at for LSPR materials. In this regard, LSPR has been used for a variety of sensing purposes including refractive index detection as well as a different approach using surface enhanced Raman spectroscopy.

### 1.2.5 Surface Enhanced Raman Scattering

Raman scattering was first predicted and experimentally confirmed in the 1920's A. Smekal and C. V. Raman.[32, 33] Smekal theoretically demonstrated that when monochromatic light scatters through a material, not only is the same wavelength of light refracted, as well as additional scattered light with higher and lower energies than the excitation source with material dependent properties. Raman scattering can occur without the absorption of a photon, and as such the electronic transition state does not exist. This causes the Raman scattering to be an inherently weak process. Raman measurements were then only frequently used for highly concentrated pure samples to produce signal. However, in the 1970's a technique known as Surface Enhanced Raman Scattering (SERS) was discovered, which made the usage of Raman more common and made it possible to use in a wider variety of systems.[34]

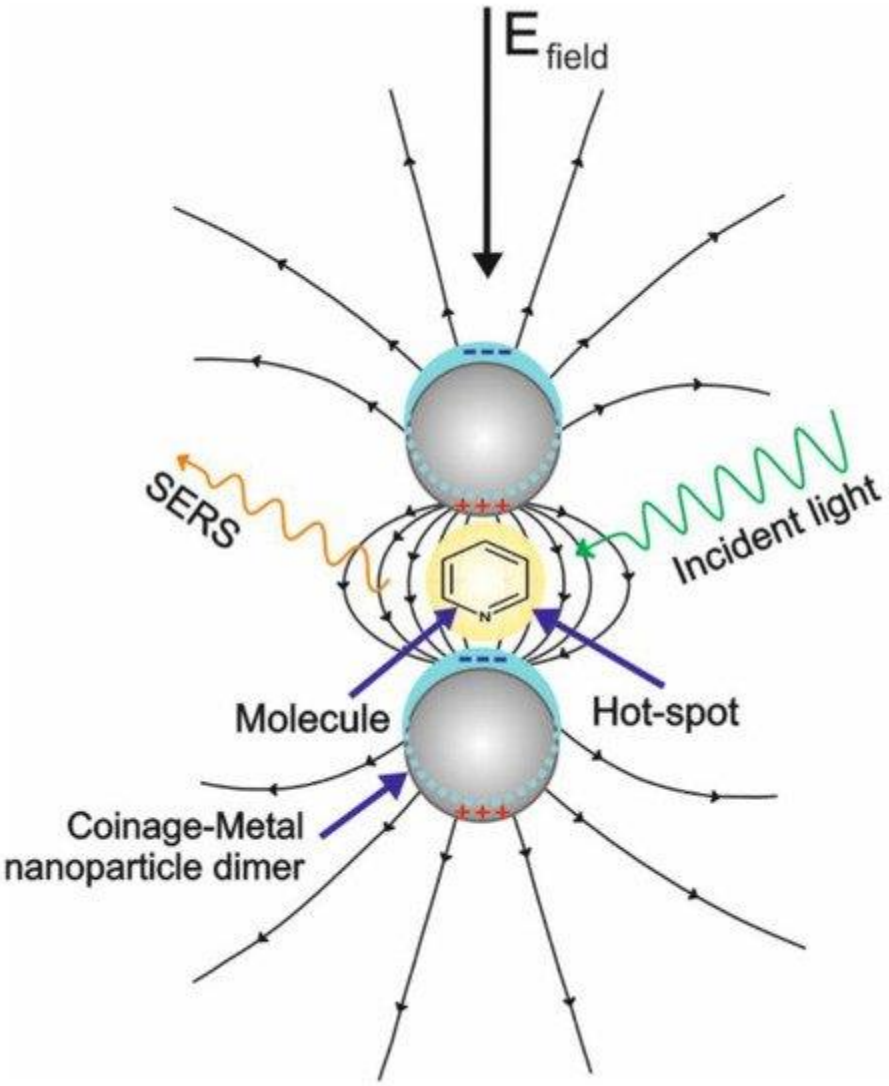


**Figure 1.6** A cartoon demonstrating the fundamentals of SERS and the interaction between the nanoparticle and incident wave, and the analyte and nanoparticle. [35]

There are two main mechanisms that are attributed to the SERS effect, electromagnetic (EM) and chemical enhancement (CE).[36] The EM enhancement effect is generally considered the principal mechanism of SERS and allows for the sub nano-molar detection SERS is capable of. When incident light excites the LSPR of a metal nanoparticle, this energy can transfer from the metal to the analyte, enhancing both the

Stoke and anti-Stokes scattering of molecules close to the metal surface. The EM enhancement effect is heavily distance dependent, based upon the length of the LSPR oscillation and absorptive cross section of the molecule. Evidence supporting the EM enhancement theory is demonstrated by increased enhancement correlative to simulated field enhancement, as well as red and blue shifting of the Raman bands when under SERS configuration. [37, 38] The CE enhancement is due to ordered organization of the analyte onto the surface, and electron charge transfer from the surface to the analyte. This was proven through the usage of non-plasmonic semiconductors with which SERS enhancement was still found. [39, 40] Mathematical models that predict SERS enhancement solely rely on the EM aspect, and do not account for the CE.[41]

SERS enhancement is maximized when the excitation wavelength corresponds to the extinction spectra of the LSPR. Therefore, the methods through which the LSPR substrate is produced need high consistency. Developments of SERS substrates have focused on improvement of the consistency through varying methods of metallic nanoparticle fabrication as well as increasing the number of hotspots. Hotspots are formed at the junction between two nanoparticles, so methods to form consistent oligomers of nanoparticles have been studied.[42-44]

### 1.3 Optical Simulations

Through using the fundamental physics of surface plasmon resonance, the electromagnetic response of a variety of systems can be predicted. This allows for optimization of analytical systems as well as exploration of novel sensing capabilities without requiring the time and resources required for fabrication. There are a variety of

methods with which one can simulate plasmonic systems, depending on the complexity of said system. Simple thin films can be predicted with Fresnel equations whereas complex nanoparticle systems require either Finite-Difference Time Domain or Finite-Element Time Domain simulations.

### 1.3.1 Fresnel Equations

Fresnel equations allow for the solving of absorbance, transmittance and reflectance of a given material based upon its refractive index, thickness and the incident angle of the exciting radiation.[45-47] For a system that contains multiple interfaces, the Fresnel equation must be repeatedly solved for each of these interfaces sequentially, as the incident angle of the exciting light will change upon each refraction. For these calculations the materials in question are reduced to a singular dimension in space and are assumed to extend infinitely in two axes. This simplification of the calculations are the Fresnel equations largest strength and weakness as the simplified equations reduced computational power necessary to solve them but limit the systems that they can applied to. [48]This strength has allowed them to become a powerful tool regarding determination of optimal conditions for thin film plasmonic metal systems.

For a given system, if the refractive indexes are known, the behavior of light when interacting with a thin film of specific thickness can be predicted. This has been used for a variety of systems including: plasmonic sensors, thick film polymers, interferometers, and optical filters among others.[46, 49, 50] Of these plasmonic sensors are of particular focus. In addition to being able to predict traditional plasmonic sensors, more complex systems such as plasmonic waveguides can also be predicted. In particular waveguides benefit from

Fresnel calculations as they are very sensitive to both the refractive index of the materials used as well as the thickness of the material. Through using predictive modeling, optimization and fabrication of waveguides has been streamlined.[51, 52]

### 1.3.2 Finite-Difference and Finite-Element Time Domain

Finite-Difference Time Domain (FDTD) and Finite-Element Time Domain (FETD) are simulation methods that solve Maxwell's equations for three dimensional systems by dividing said system into a high quantity of smaller solvable parts. Both systems have been demonstrated to be powerful tools in the solving of Maxwell's equations for a variety of applications including biological matrices, EM interaction with earth media, and the main focus that is used for this work, in which they are used for the design of metamaterials. [53-55]

FDTD was first proposed by Yee in 1966, in which he described a methodology to used finite equations to solve Maxwell's equations, specifically with the intent to make them solvable using computational methods. In this it is assumed that the boundary conditions are perfectly conducting, and the E and H fields are solved for in all dimensions *i, j* and *k*. Through forming discrete cubes, the conducting materials can be constructed with a series of cubes to best mimic the shape of the material in question. However, when doing so the stability of the EM field must be considered inside each cube. This can be described in equation ()

$$\sqrt{(\Delta x)^2 + (\Delta y)^2 + (\Delta z)^2} > c\Delta t = \sqrt{\frac{1}{\epsilon\mu}}\Delta t \quad (1.17)$$

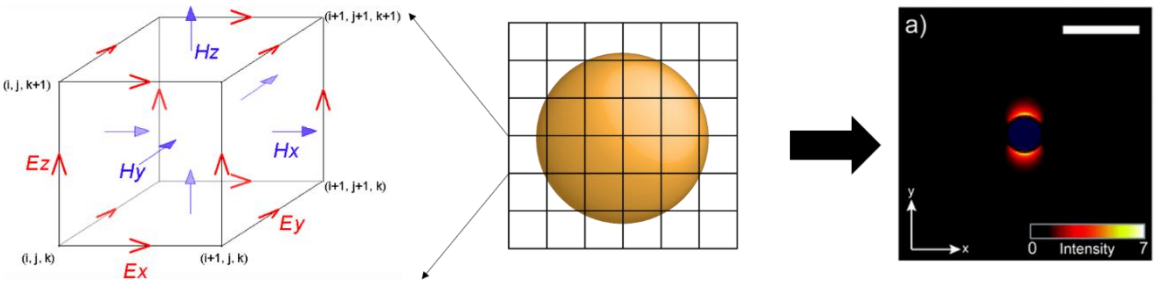


**Figure 1.7** A demonstration going from the fundamental Yee cell (left) to the how a gold nanoparticle would be discretized (middle) to the graphical readout (right).

Wherein c is the speed of light, and ϵ and μ are the permittivity and permeability of the material. This determines the restrictions for the size of the individual cell, wherein the distance the light travels in the time increment is the minimum size for the Yee cell. In each of these cells we will solve the finite formation of Maxwell's equations as follows:

$$E_z^{n+1}(i,j) = E_z^n(i,j) + Z\frac{\Delta\tau}{\Delta x}\left[H_y^{n+\frac{1}{2}}\left(i+\frac{1}{2},j\right) - H_y^{n+\frac{1}{2}}\left(i-\frac{1}{2},j\right)\right] -$$

$$Z\frac{\Delta\tau}{\Delta y}\left[H_x^{n+\frac{1}{2}}\left(i,j+\frac{1}{2}\right) - H_x^{n+\frac{1}{2}}\left(i,j-\frac{1}{2}\right)\right] \quad (1.18)$$

$$H_x^{n+\frac{1}{2}}\left(i,j+\frac{1}{2}\right) = H_x^{n-\frac{1}{2}}\left(i,j+\frac{1}{2}\right) - \frac{1}{Z}\frac{\Delta\tau}{\Delta y}\left[E_z^n(i,j+1) - E_z^n(i,j)\right] \quad (1.19)$$

$$H_y^{n+\frac{1}{2}}\left(i+\frac{1}{2},j\right) = H_x^{n-\frac{1}{2}}\left(i+\frac{1}{2},j\right) - \frac{1}{Z}\frac{\Delta\tau}{\Delta x}\left[E_z^n(i+1,j) - E_z^n(i,j)\right] \quad (1.20)$$

These equations are then solved for in each Yee cell to determine the field strength across an object. The Yee cell size, is key in this process as the smaller the cell, the higher the resolution of the resulting simulation will be. However, smaller cells will require more computing power, as each cell is solved for individually.[56] To help alleviate this problem, the finite element method (FEM) was applied as a different method to divide a material into solvable subsections. Whereas FD uses a uniform grid, FEM uses a mesh of variable sizes and shapes. FEM is advantageous with increasingly complex geometries as well as having a higher accuracy compared to FD. Taking the information and optimization discovered in simulation techniques, they then need to be confirmed experimentally for further testing. [57]

## 1.4 Surface Fabrication

Although a large variety of surface structures can be predicted theoretically, fabrication of said systems requires precise techniques. Fabrication of nano-sized materials requires methods that can consistently and controllably form nanostructures. A wide variety of these methods exist and serve differing purposes depending on the size and material of the surface being fabricated, as well as the specificity of the structure required for the system. In addition to the techniques required to fabricate these surfaces, confirmation is necessary to confirm the structure. Visualization of the real structure can then inform future theoretical models to assess the plasmonic capabilities.

### 1.4.1 Deposition Techniques and Photolithography

There are three main deposition techniques, each with their own advantages and disadvantages. The three techniques are as follows, physical vapor deposition (PVD), chemical vapor deposition (CVD) and plasma spray. The differences between them are dependent on the chemical composition of the material, deposition rate and thickness, surface roughness, microstructures, as well as the environment required to necessitate the techniques. [58]

In the work that will be discussed in further chapters, a subset of PVD, EB-PVD will be used for the deposition of materials such as gold and aluminum. EB-PVD matches the requirements necessary for the formation of films that plasmonically active. The deposition rate of EB-PVD can be tuned and varies from ~2 μm to ~0.5 Angstroms per second, depending on the necessary thickness of the film in question. There are 4-main components necessary for an EB-PVD instrument, also known as an E-beam. The E-beam contains an EB-gun, a crucible (containing the material to be deposited), the substrate, and a vacuum chamber in which all of aforementioned parts are housed. In addition to this, E-beams frequently contain a variety of materials that can be used for multilayered material systems.[59] This is of particular use in the fabrication of gold films for SPR, as gold requires either a titanium or chromium adhesion layer on glass substrates.[60, 61] In the E-beam, a high-power electron beam is focused at the material in question in a vacuum, and a vapor is formed. This vapor will subsequently deposit onto the substrate that has direct line-of-sight to the heated crucible, therefore rotating of the substrate is frequently employed to allow for an even coating. This process is of increasing import as the substrates that are

coated increase in complexity. The mechanism by which the vapor forms onto the substrate is of particular import when microstructures are formed on the surface. [62, 63]

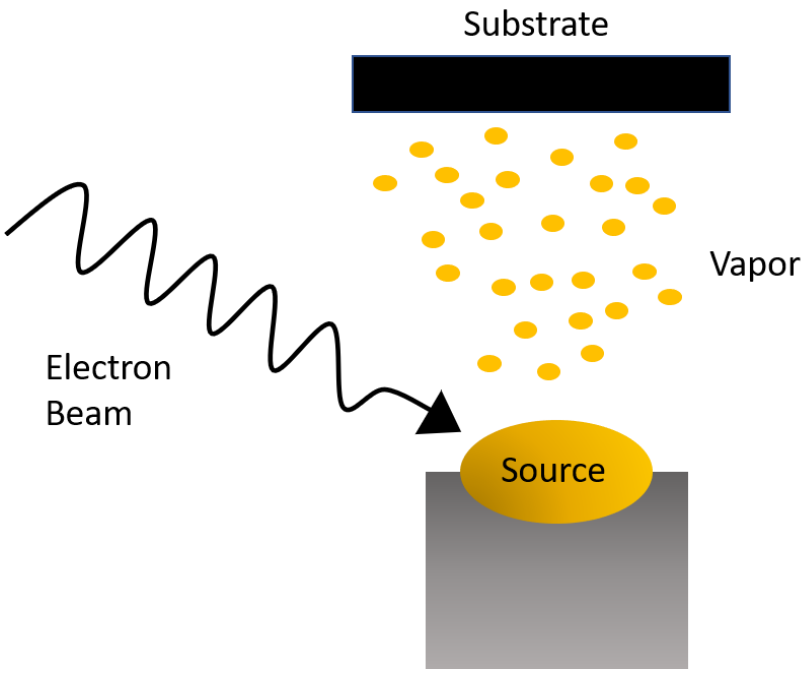


**Figure 1.8** A demonstration of the fundamental components of an EB-PVD.

As previously mentioned, E-beam deposition forms micro or nano granules during deposition. This is caused by nucleation mechanism with which the vapor deposits onto the surface. Vapor will first deposit onto areas with the lowest activation energy necessary for the solid to form. Upon these nucleation points, crystal growth will occur spreading out from these individual particles in all directions. Finally, the granules will converge into a singular film and reorganize to the lowest energy structure. The method by which the granules combine is dependent on the chemical composition as well as the temperature of the system. The formation of the microstructures has been found to be dependent on the melting point of the material ($T_{MP}$), and the temperature of the substrate ($T_{sub}$), as well as

the pressure. In the lowest energy systems ($T_{sub}/T_{MP} < 0.3$) causes microcolumns with large voids between individual columns to form. As the energy of the system increases, the smoothness of the surface increases as the coalescing of the individual granules formed during nucleation becomes prominent. This allows for the formation of highly ordered thin films.[59, 64] This ability to deposit controlled metallic thin films is then combined with photolithography to generate complex metallic microstructures.

Photolithography is a method in which selective etching of a photoactive polymer is achieved through photopolymerization to distinguish between cured and uncured polymer for further chemical treatment to remove the unwanted polymer. A photomask that is designed to match the desired shape is used to direct polymerization.[65] The first step in photolithography is controlled application of the photo-resist to the substrate. This is achieved through spin-coating the photo-resist, which results in a polymer thickness of between 1-3 μm. As the photo-resist is a highly hydrophobic material, pre-treatment of the substrate is occasionally necessary to allow for adhesion of the photo-resist during spin coating. This is mostly commonly needed for glass substrates wherein silanes polymers are used to form a hydrophobic coating. Selection of photo-resist is necessary as the resolution of the structure is dependent on the thickness of the resist after spin-coating. After the photo-resist is spin-coated onto the surface, the photomask is used to physically block incoming light from polymerizing the specified areas. Afterwards, a developing solution is used that will remove the unpolymerized photo-resist. Further surface modification can then be applied to generate either a negative or a positive image of the photo-resist. Finally,

the polymerized photo-resist will be removed to leave only the patterned material required. [66]

### 1.4.2 Solution-Based Nanomaterials

Nanoparticles are generally organized into organic and inorganic particles with further specification in each category.[67] Organic nanoparticles consist, of micelles, vesicles, dendrimers etc. and have found many applications towards drug delivery.[68-70] In addition to this they have been studied for their *in vivo* presence as is the case with exosomes and liposomes present throughout mammalian bodies.[71] Inorganic nanoparticles have a wide range of material, and include metals and metal oxides.[72, 73] There are two main approaches in regards to synthesizing nanoparticles, the top-down approach, wherein a bulk material is degraded into smaller particle sizes, and a bottom-up approach where the nanoparticles are built from individual atoms and agglomeration causes them to form nanoparticles.[74] The further discussion of nanoparticle fabrication will focus on the latter bottom-up approach.

For applications for widespread use, solution-based methods of fabricating nanoparticles are frequently used. This is a bottom-up approach in which the starting materials are dissolved in a solvent, and when mixed nucleation occurs starting the process of nanoparticle formation. From this initial nucleation site, crystalline growth will continue until the reaction is quenched to reach the desired nanoparticle size. This method in which the nucleation site is produced during the same reaction as the crystalline growth is referred to as primary nucleation, however for the synthesis of larger nanoparticles seeding the

reaction with nucleated material is beneficial for decreasing the polydispersity of the nanoparticles. A common example of this is the synthesis of colloidal gold nanoparticles.

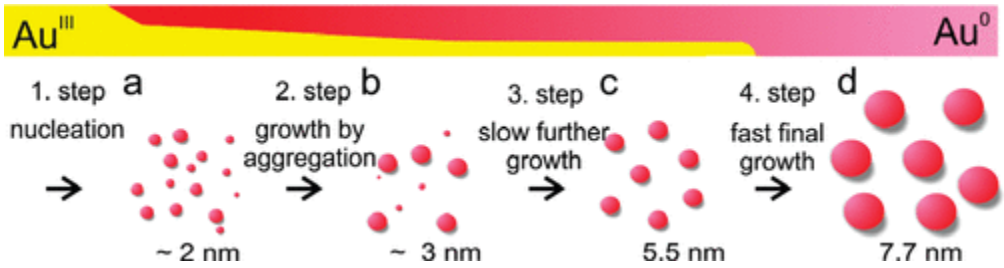


**Figure 1.9** The mechanism by which gold nanoparticles form, starting from $Au^{III}$ progressing to $Au^0$ . [75]

In the synthesis of gold nanoparticles, there are a variety of methods which involve the reduction of $HAuCl_3$ to $Au^0$. The most common method was developed by Turkevich in which trisodium citrate is used as the reducing agent and injected into a solution of boiling tetrachloroauric acid.[76] The gold nanoparticles formed are capped with the citrate allowing for a stable colloid in aqueous solution. However, polydispersity of the nanoparticles in the colloid is a continuous issue. A variety of modifications to the original procedures have been discovered that alleviate this issue. Commonly polymeric stabilizers are added as additional capping reagents, and sodium borohydride is used instead of trisodium citrate as the reducing agent.[77] Commonly used polymers include, thioesters, polyvinyl pyrrolidone, thiol-polyethylene glycol among others. These polymers will cap the particles will still allowing for further chemistry due to active groups present on the polymers.[78] After fabrication of the nanoparticles, further complex structures can be synthesized forming larger macrostructures.

### 1.4.3 Nanoparticle Assemblies

Nanoparticles can be assembled into larger ordered structures to change both the chemical and electromagnetic responses of the particles. This is caused due to the interactions formed in the nanoscale gaps between the nanoparticles.[79] A variety of methods have been developed to form nanoparticle assemblies with consistent spacing and ordering. Common methods include chemical ligands to bind nanoparticles together, polymer surface modification, liquid-liquid interfaces, air-liquid interfaces, and evaporative self-assembly. Each of these range in advantages and disadvantages dependent upon the ease of use, wide range of versatility regarding the nanoparticle substrate, and dispersion of the nanoparticles on the final substrate.[80-82]

Surface modification is a popular technique to form nanoparticle assemblies due to being simple procedures with a wide range of polymers available allowing for the chemical modification of the nanoparticle to be maintained. Initial work towards this was performed with positively charged polymers, allowing for citrate capped gold nanoparticles to self-assemble onto the polymer due to charge-based interactions. Due to the individual nanoparticles repelling each other statically they form an ordered structure on the polymer surface.[83] In addition to this, more direct chemical modifications can be used such as monolayers of alkane thiols, which will covalently bind gold nanoparticles. An alternative method that involves direct synthesis of gold nanoparticles onto the surface has also been performed using polydopamine, which catalyzes the reduction of $HAuCl_3$.[84] However, these systems frequently cause high dispersity of nanoparticles leading to alternatives being popular.

Liquid-liquid interfacial methodologies have grown to be increasingly beneficial for the formation of nanoparticle assemblies. Liquid-liquid methods involve taking advantage of the thin layer of interaction between two immiscible solvents.[85] Nanoparticles that are soluble in one solvent, either aqueous or hydrophobic, will be capped molecules of opposite solubility. This will cause the nanoparticles to assemble at the interface between the liquids, but due to the amphiphilic nature of the nanoparticles they will solely assemble at the interface in a thin layer.[86] This nanoparticle layer can either be used in the liquid phase or can be transferred to a solid substrate for ease of use. Doing this frequently relies upon solid substrate being chemically modified to optimally support the transference of the nanoparticles.[87] In addition to solely relying upon the self-assembly at the liquid interface, the capping agents can effect the spacing of the nanoparticles which is of key importance in their applications, most notably SERS.[88]

### 1.4.4 Surface Characterization

There are a variety of methods with which surface characterization can be achieved, including atomic force microscopy (AFM), surface electron microscopy (SEM), transmission electron microscopy (TEM), x-ray diffraction (XRD), x-ray photoelectron spectroscopy (XPS), and ellipsometry. Of these techniques, AFM, SEM and TEM are all used for structural information regarding the surface of interest. XRD and XPS are used for chemical information, as well as being able to determine the thickness of the material. Ellipsometry can similarly be used to determine the thickness of thin films, and can also be used to determine the refractive index of a thin film if the thickness is known.[89]

AFM relies upon a cantilever with a sharp tip connected to a piezoelectric actuator, with a photodetector used to identify reflected laser light to provide feedback when the cantilever is deflected. As the tip moves across a surface it follows the shape of said surface and the laser light deflected will be detected and be used to determine the degree with which the cantilever moves. The piezoelectric actuator is used to control the specific height or force of the cantilever allowing for a fine control.[90] There are 3 modes in which AFM can be run, contact, non-contact and tapping. Contact mode is most commonly used and measures the repulsive forces of the surface against the tip. This is seen as a change in the resonant frequency of the cantilever and allows for topographic information to be elucidated. Non-contact mode measures the attractive forces between the tip and the surface, and while it has lower resolution than contact mode due to the strength of attractive vs repulsive forces, it is more suitable in applications of soft samples. Tapping mode is similarly applied as a technique to measure soft surfaces and does so through detecting changes in the oscillation frequency of the tapping motion. [91] When compared to other surface characterization techniques, AFM is advantageous as it requires little to no surface modification, is performed at ambient conditions, and has a large working range. However, outside the resolution and magnification of AFM, outside of a few examples, does not compare to that of SEM and TEM.[92]

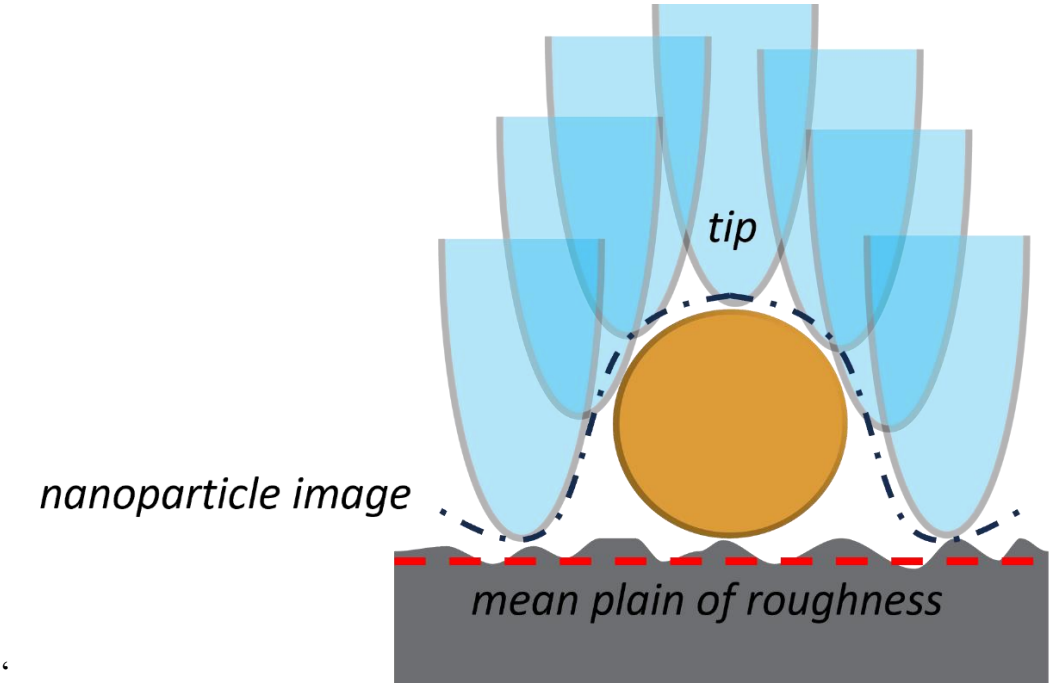


‘

**Figure 1.10** A demonstration of how AFM would measure the size and shape of a nanoparticle, as well as the overall roughness of a surface.

Due to the diffraction limit of light, spatial measurements using optical microscopy are limited. However, using electron emission techniques higher magnification levels can be reached on the order of 300,000x magnification. TEM was the first technique to take advantage of this and can obtain a resolution of down to 0.05 nm in high resolution TEM. The fundamentals of TEM rely upon the interactions between the electrons and the surface, specifically the diffracted electrons and the transmitted electrons. The electron diffraction pattern can determine the crystallographic structure of the material, and is similarly used to image the material. As the electrons must either transmit through or diffract through the material, TEM only functions on materials <100 nm in thickness. [93] In practice, the sample that is being imaged is placed onto a TEM grid, usually comprised of a conductive metal

such as copper, platinum, or gold with a carbon mesh. To enhance TEM contrast in materials that do not contain high atomic number atoms, such as biologics, a stain is used such as uranium or gold that is selected to bind to the specific biological molecule.[94, 95] However, TEM is limited in providing 3D structural information, as well as handling materials that are thicker than 100 nm.[96] To then get this information SEM is used.

SEM uses backscattered electrons and secondary electrons for the production of images. As these electrons are of a relatively low energy, they will only emit from surface of the material, with a depth of only a few nm. For SEM, samples must be highly conductive, and are additionally grounded. Thus, metal substrates require little preparation for SEM, whereas nonconducting materials require a surface coating. This is frequently achieved through sputtering of a metal or graphite to act as the conducting layer. The 3D images present in SEM are caused by the generation of signal being dependent on the angle of incidence of the electron beam. As the signal is dependent on the number of released secondary electrons, the greater the interaction area between the top surface layer and the electron beam, the greater the signal. As such when the surface is perpendicular to the electron beam the signal is lowest and the areas appear darker, and the areas that approach parallel with the electron beam are brighter. [97] In addition to this, changing the pitch and roll of the stage can be used to image the substrate at a different angle providing more information regarding the 3D structure. [98]

### 1.5 Principles of Biosensing

Biosensing is a key component in a variety of fields, including medical analysis, pathogen and disease detection and environmental monitoring.[99-101] Biosensors are

defined by their ability to generate a signal in response to a biological compound of interest. This requires a method through which the biological compound is selected for, and a measurement method that connects the selection of said compound to a readout by a user. The first part, which binds the biologically relevant molecule, is frequently a biological molecule that is a binding partner for the analyte.[102, 103] There is a large interest in this area of research as expanding the available capture methods increases the possible targets for a biosensor. The transference from the biological binding to a readout is done through a system sensitive to physical change, such as that of an electrical pulse for example, and a detector that can detect that physical change through whatever medium is best suited for the system.

The two main categories of biosensors are qualitative and quantitative. A qualitative sensor emphasizes the detection of an analyte of interest while a quantitative sensor provides an exact concentration of the target. A focus of biosensor research is frequently towards disease detection, which is done through analyzing the presence of molecular components such as small molecules like glucose and hormones, proteins such as antibodies or whole cells.[104] This is commonly seen in consumer products such as glucose monitors, pregnancy tests, and COVID tests.

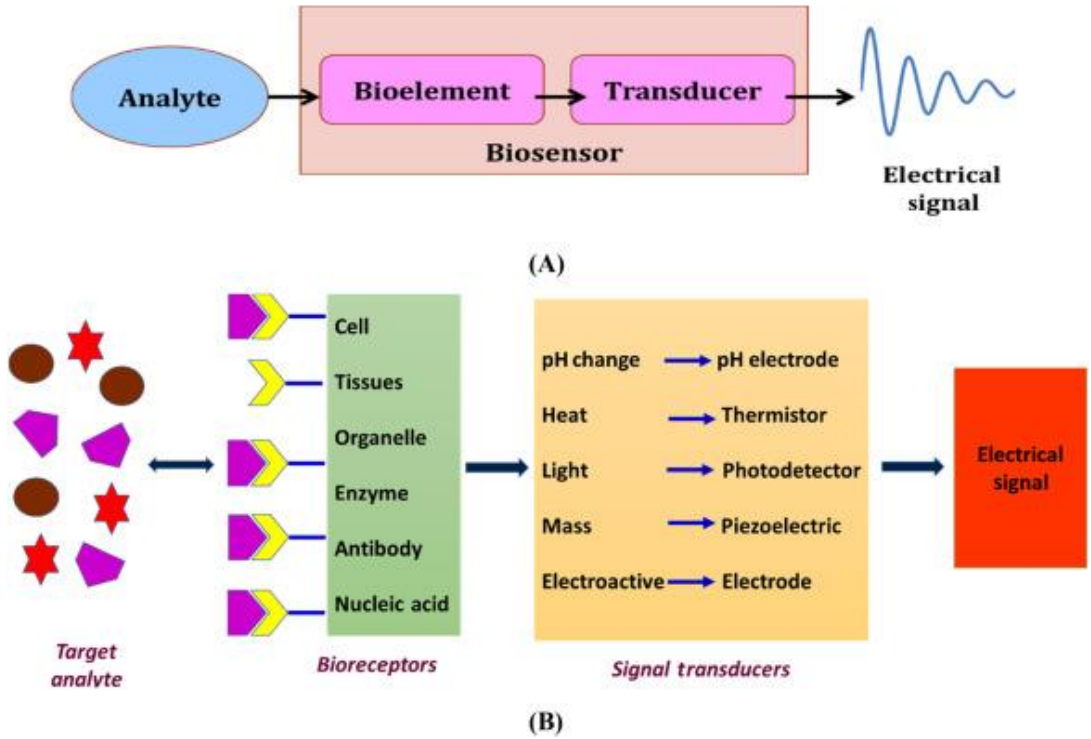


**Figure 1.11** The fundamental components of biosensors, including the mechanism to capture and transduce signal.[105]

Biosensing schemes have the ability to be simple, robust and portable. This has made them an important tool in health crises as widespread diagnosis and monitoring is required. Many diseases such as cancers and autoimmune disorders originate from a fault in the production of certain proteins. [106, 107] Biosensors provide two avenues in which they improve disease analysis. First, through detection of diseases such as antibody-antigen interactions that are found at the central locus of many autoimmune diseases. And second, as a way to better understand the biological pathways of a disease through induced biomolecular changes. They have been employed thoroughly in this capacity for proteomic studies where are they are used to quantify levels of proteins.[108]

Further distinctions of biosensors can be seen through the differentiation of label and label-free biosensing systems. In a label-oriented system, the production of signal is reliant on a molecule outside that is separate from the analyte of interest and must either be conjugated to the analyte before application to biosensor, or can be done after the molecule is captured in the sensor.[109] Common examples of this are fluorometric measurements in which a fluorophore must be attached to the analyte before the binding to the biosensor occurs.[110] These techniques are very sensitive, although they do not directly measure the molecule of interest binding interaction.

In contrast, label free techniques directly measure the analyte of interest, without a secondary component necessary. These frequently rely upon detecting a change in magnetic or electrical field, and include, field effect transistors, quartz crystal microbalances, and optical techniques such as SPR.[111-113] Label-free sensing systems detect the binding interaction directly, and so they provide signal quickly, allowing for integration into systems that require constant real-time monitoring. In addition to this, label-free techniques do not need to add material to the analyte, removing the changes in binding that are caused by labelling. They are also very sensitive to changes in the material at the surface which, while beneficial, requires control of the surface to limit the possible interactions to only those of interest. Therefore, there has been thorough investigation towards preventing non-specific binding events to further the capabilities of label-free techniques. [114]

### 1.6 Plasmon Based Biosensing

Plasmons allow for the conversion of incident photons into high strength, localized electromagnetic fields that can be taken advantage of as part of a biosensing device to either enhance or generate signal. This requires the biosensing device to be optically coupled in some manner, with a plasmonic material designed to match the optical light source. The plasmonic nature can either be used as the sensing system, such as in SPR biosensing or can be used as an enhancement of already present signal such as in surface enhanced Raman scattering (SERS). The plasmonic substrate can be customized to best suit the system requirements, for example metallic thin films for usage in SPR and gold nanoparticles for usage in SERS.

### 1.6.1 SPR Based Biosensing

SPR biosensors were first demonstrated in 1983, wherein the binding of IgG and an anti-IgG antibody was detected using a 60 nm silver film.[115] This then opened up the possibilities of SPR to be used as a real-time, label free biosensor. Through SPR-biosensors, multiple avenues arose, from environmental detection to bioanalyte detection for the purposes of disease analysis.[116-118] Similarly, the SPR sensogram can be used to empirically determine the association, steady state and dissociation kinetics of a given interaction. Therefore, one of the main applications for SPR has been towards drug candidate discovery through affinity measurements.[119] Further exploration of SPR has been towards expanding bioconjugation to metals and subsequent conjugation to functionalized surfaces. [120, 121]

Common functionalization of gold, the most common plasmonic metal used for SPR, include the strong bond between gold and thiols. Alkanethiols deposited onto a gold

surface will form a self-assembled monolayer, this layer has two-fold benefits.[122] First, it can have a secondary functional group, on the opposite end of the thiol, that can be used for further conjugation, and second, it provides anti-fouling capabilities, as the hydrophobic alkane layer repels unwanted non-specific interactions. In addition to alkanethiols, biologically relevant molecules can be modified with thiol groups or contain already present thiol groups. This can be used with a variety of systems, including aptamers, biotin, and EDC/NHS, depending on what is needed for the system.[123, 124] In addition to thiols, polymers can be used.

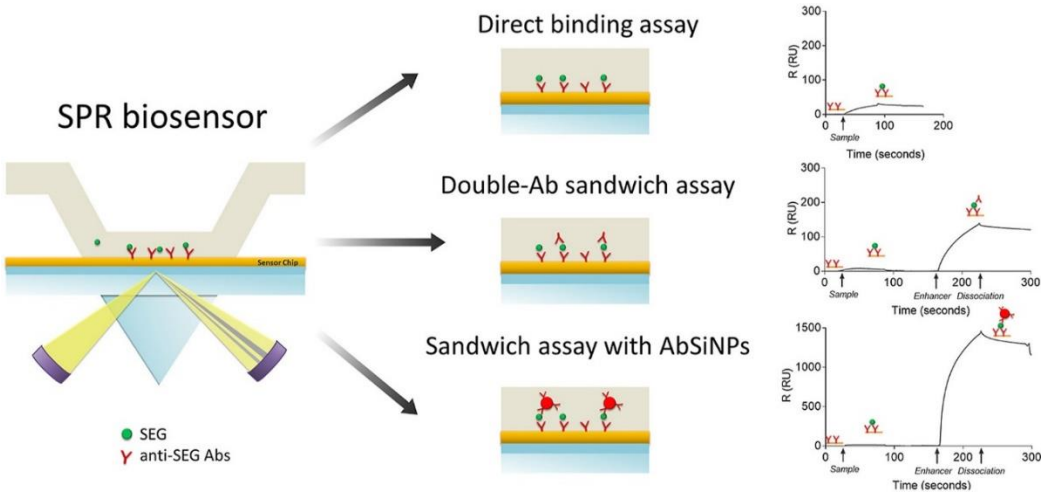


**Figure 1.12** A variety of assays and the expected sensogram from them for biosensing.[125]

Dextran polymer are frequently used in commercialized SPR chip manufacturing as they provide a high concentration of active carboxymethyl groups which allow for binding to free aminos, as well as providing an anti-fouling surface layer.[126] However, these large polymers while providing a variety of binding sites, reduce SPR sensitivity as

their thickness is on the order of 100 to 200 nm, and the SPP loses sensitivity as it propagates from the surface. This causes alternatives to polymer systems that maintain the anti-fouling and functional properties, without the aforementioned thickness, to be attractive options.

An additional common method first requires a silica layer be deposited onto the gold substrate.[127] This layer can then subsequently be modified through silane chemistry to produce the binding system needed. This has similar applications to the thiol chemistries, however other applications for silicated SPR chips exist.[128] Lipid bilayers will spontaneously form from vesicles onto the silica surface under aqueous conditions. As these vesicles can be modified to contain functional groups, they can be used as biomimetic systems in biosensing SPR studies. Further, biologically relevant molecules that are specific to the analyte of interest can be incorporated into the lipid vesicles and will therefore be transferred to the SPR surface. This approach takes advantage of the surface-based sensing to best mimic the true systems present in cellular systems, while also providing an anti-fouling layer that can be applied on-line without prior chemical modification.[129-132]

To further the limits of sensing of SPR, amplification techniques are employed through the binding of additional material. This is commonly achieved through the usage of an antibody that is specific to the analyte and they can be conjugated to other methods of amplification such as nanoparticles or biotin.[20, 133-138] As these will provide an increase in mass, the signal will subsequently increase lowering the limits of quantification. In the specific case of plasmonic nanoparticles, a coupling effect between the particle and the

surface can further enhance the signal provided by the nanoparticle. This effect caused by the coupling of the surface plasmon and the localized plasmon of the nanoparticle causes a much larger shift in the incident light referred to as "back-bending." [139] This effect in combination with the large mass of gold nanoparticles have made them a common method of amplification for SPR biosensing. [140]

### 1.6.2 Surface Enhanced Raman Scattering Biosensing

SERS takes advantage of weak Raman scattering and amplifies it to allow for analyte identification and detection. SERS has been documented to provide enhancement of up to $10^8$ allowing for the normally low Raman scattered signal to be detected. There are two main approaches regarding using SERS as a biosensor, either the biomolecule of interest is detected based upon its signature Raman fingerprint, or a well-documented Raman tag is used whose spectrum will change upon binding of the specified analyte. This is referred to as intrinsic and extrinsic sensing respectively. [141]

Intrinsic SERS biosensing is advantageous as it can provide specific chemical information regarding the biomolecule as well as being a label-free technique akin to SPR. Whereas extrinsic sensing requires less data analysis as the changes in the well-defined Raman reporters and sharp Raman bands cause deconvolution of complex data to be comparably simple.[142-145] However, problems still arise when applying SERS to biosensing applications. First, is the fundamental nature of SERS. For SERS fabrication to be sufficiently useful for biosensing applications, the substrates must consistently reproducible as well as simple to fabricate. A large portion of SERS research has been

towards reducing the variance from substrate to substrate for this very reason. In addition to this, in complex samples interfering Raman spectra cause the signal from the analyte to be masked. This has been recently overcome through using surface-based binding techniques or through sample processing to separate for the analytes of interest. [146-148]

### 1.7 Aims and Scopes of Dissertation

The goal of this dissertation is to improve plasmonic sensing capabilities from a fundamental materials standpoint. This is done through either improving the sensitivity of the materials and optimization of them through novel materials, such as aluminum thin films and gold nanoparticle arrays, or through methods to improve material conjugation to sensing molecules. The applications that this will be primarily focused on is SPR, in addition to SERS, the advantages and limitations of which have been discussed in this chapter. In these subsequent chapters methods to improve the sensitivity and diversification of materials available for SPR and SERS will be discussed, as well as how using theoretical models can allow for more efficient optimization. The overall scope of this is for furthering the materials development of plasmonics for biosensor applications, as understanding and taking advantage of the fundamental plasmonic properties can improve the methods and systems with which biological interactions are understood.

Chapter 2 begins with exploring aluminum and the natural oxide formed for the purposes of SPR. Focusing on changes to the AlOx layer as well as exploring one of the strengths of Al, that it is plasmonically active under the entirety of the UV-vis EM spectrum. In this work, a custom modeling system was made that allowed for simultaneous determination of the optimal thickness of AlOx and incident wavelength of light. In

addition to this, waveguiding behavior was discovered wherein s-polarized light created a plasmonic shift. Through taking advantages of both these effects, the efficacy of these "thick" AlOx films on Al as a self-referential sensor was determined. In this way, the sensor can differentiate between the bulk changes to the refractive index and changes to the refractive index of the surface.

Chapter 3 begins with the discussion of aluminum as a thin film plasmonic material, and its potential applications as a biosensing substrate. Fundamental benefits of Al thin films are explored as well as compared to the standardized Au substrates. In this Al films were first theoretically modelled and then subsequently fabricated. Notably, the Al films were found to be more sensitive to refractive index changes than Au and also demonstrated antifouling properties due to the formation of AlOx layer. This AlOx layer is responsible for not only the antifouling of Al, but also for the stability and possible future conjugation of the surface to other sensing molecules.

Chapter 4 applies the Al thin films towards a biological disease detection scheme. In this work to improve the conjugation abilities of the surface, a SiOx layer is deposited onto the Al substrate. This then allows for techniques that are well established to be applied, namely the formation of hydrophobic surface using perfluorinated silanes, and a subsequent self-insertion of lipids to the surface. These DGS functionalized lipids are then used to build our sensing surface with a histidine tagged Myeline-associated glycoprotein (MAG). This is then used with SPRi for the detection of the anti-MAG antibody, which is associated with demyelinating neuropathy, an autoimmune disorder. To more readily

demonstrate the systems capabilities in biological media, artificial urine is spiked with anti-MAG and used to determine the efficacy for a real biological system.

Chapter 5 explores gold nanofilm substrates and their potential for SERS. In this chapter, the development of self-assembled monolayers of Au nanoparticles using an interfacial glue molecule, dibenzotetrathiafulvalene, is demonstrated and characterized. This forms a self-healing mirror-like droplet known as Au metallic liquid-like droplet or Au MeLD. This Au MeLD can then be transferred to a solid substrate and then used for sensing purposes. The first application was towards SPR, where it demonstrates limited usage, however, it is the optimal substrate for SERS. The Au MeLD causes Au nanoparticles to form a hexagonally closed packed structure with a consistent distance between molecules due to the interfacial glue. This makes it an ideal surface for SERS. To demonstrate the systems capability as a SERS substrate, PCB-126, a known environmental toxin, was detected using the Au MeLD surface.

## 1.8 References:


1. Raether, H., *Surface Plasmons on Smooth and Rough Surfaces and on Gratings* Springer Tracts in Modern Physics, ed. G. Hohler. Vol. 111. 1988: Springer.

2. Tanabe, I., et al., *Aluminum Film Thickness Dependence of Surface Plasmon Resonance in the Far- and Deep-ultraviolet Regions.* Chemistry Letters, 2017. **46**(10): p. 1560-1563.

3. T. W. Ebbesen, H.J.L., H. F. Ghaemi, T. Thio, P. A. Wolff, *Extraordinaryoptical transmissionthrough sub-wavelengthhole arrays.* NATURE 1998. **391**.

4. Wu, L., et al., *Reflection and Transmission Modes in Nanohole-Array-Based Plasmonic Sensors.* IEEE Photonics Journal, 2012. **4**(1): p. 26-33.

5. Mattheyses, A.L. and D. Axelrod, *Direct measurement of the evanescent field profile produced by objective-based total internal reflection fluorescence.* J Biomed Opt, 2006. **11**(1): p. 014006.

6. Pilot, R., et al., *A Review on Surface-Enhanced Raman Scattering.* Biosensors (Basel), 2019. **9**(2).

7. Born, M.A.X.W., E., *,CHAPTER III - FOUNDATIONS OF GEOMETRICAL OPTICS*, in *In Principles of Optics (Sixth Edition)*, B. , M. A. X.; Wolf, E., Eds. Pergamon, Editor. 1980. p. pp 109-132.

8. Addanki, S., I.S. Amiri, and P. Yupapin, *Review of optical fibers-introduction and applications in fiber lasers.* Results in Physics, 2018. **10**: p. 743-750.

9. Sapsford, K.E., *Total-internal-reflection platforms for chemical and biological sensing applications*. Optical guided-wave chemical and biosensors I. 2010: Springer.

10. Pospisilova, M., G. Kuncova, and J. Trogl, *Fiber-Optic Chemical Sensors and Fiber-Optic Bio-Sensors.* Sensors (Basel), 2015. **15**(10): p. 25208-59.

11. Ong, B.H., X. Yuan, and S.C. Tjin, *Bimetallic Silver–Gold Film Waveguide Surface Plasmon Resonance Sensor.* Fiber and Integrated Optics, 2007. **26**(4): p. 229-240.

12. Ritchie, R.H., *Plasma Losses by Fast Electrons in Thin Films.* Physical Review, 1957. **106**(5): p. 874-881.

13. Powell, C.J. and J.B. Swan, *Origin of the Characteristic Electron Energy Losses in Aluminum.* Physical Review, 1959. **115**(4): p. 869-875.

14. Pickering, E.C., *Applications of Fresnel's Formula for the Reflection of Light.* Proceedings of the American Academy of Arts and Sciences, 1874. **9**: p. 1-30.

15. Rakic´, A.D., *Algorithm for the determination of intrinsic optical constants of metal films: application to aluminum.* APPLIED OPTICS 1995. **22**.

16. E. KRETSCHMANN, H.R., *Radiative Decay of Non Radiative Surface Plasmons Excited by Light.* Notizen, 1968. **23 a**: p. 2135—2136.

17. Zhao, Y., et al., *Current status of optical fiber biosensor based on surface plasmon resonance.* Biosens Bioelectron, 2019. **142**: p. 111505.

18. Dillen, A., et al., *Integrated Signal Amplification on a Fiber Optic SPR Sensor Using Duplexed Aptamers.* ACS Sens, 2023. **8**(2): p. 811-821.

19. Zhang, Z., et al., *Self-Referencing in Optical-Fiber Surface Plasmon Resonance Sensors.* IEEE Photonics Technology Letters, 2007. **19**(24): p. 1958-1960.

20. Szunerits, S., J. Spadavecchia, and R. Boukherroub, *Surface plasmon resonance: signal amplification using colloidal gold nanoparticles for enhanced sensitivity.* Reviews in Analytical Chemistry, 2014. **33**(3).

21. Linman, M.J.C., Q. J, *Surface Plasmon Resonance: New Biointerface Designs and High-Throughput Affinity Screening*, in *Optical Guided-wave Chemical and Biosensors I*, M.L. Zourob, A, Editor. 2009, Springer.

22. Nguyen, H.H., et al., *Surface plasmon resonance: a versatile technique for biosensor applications.* Sensors (Basel), 2015. **15**(5): p. 10481-510.

23. Schasfoort, R.B.M., *Handbook of Surface Plasmon Resonance*, in *Handbook of Surface Plasmon Resonance*. 2017. p. P001-P004.

24. Altug, H., et al., *Advances and applications of nanophotonic biosensors.* Nat Nanotechnol, 2022. **17**(1): p. 5-16.

25. Svirelis, J., et al., *Accurate Correction of the "Bulk Response" in Surface Plasmon Resonance Sensing Provides New Insights on Interactions Involving Lysozyme and Poly(ethylene glycol).* ACS Sens, 2022. **7**(4): p. 1175-1182.

26. Zhu, L., et al., *Label-free quantitative detection of tumor-derived exosomes through surface plasmon resonance imaging.* Anal Chem, 2014. **86**(17): p. 8857-64.

27. Linda S. Jung, C.T.C., Timothy M. Chinowsky, Mimi N. Mar, Sinclair S. Yee, *Quantitative Interpretation of the Response of Surface Plasmon Resonance Sensors to Adsorbed Films.* Langmuir, 1998. **14**: p. 5636-5648.

28. Willets, K.A. and R.P. Van Duyne, *Localized surface plasmon resonance spectroscopy and sensing.* Annu Rev Phys Chem, 2007. **58**: p. 267-97.

29. *The Mie Theory*. Springer Series in Optical Sciences, ed. T.W. Wolfram Hergert. 2012: Springer.

30. Petryayeva, E. and U.J. Krull, *Localized surface plasmon resonance: nanostructures, bioassays and biosensing--a review.* Anal Chim Acta, 2011. **706**(1): p. 8-24.

31. Amanda J. Haes, R.P.V.D., *A Nanoscale Optical Biosensor: Sensitivity and Selectivity of an Approach Based on the Localized Surface Plasmon Resonance Spectroscopy of Triangular Silver Nanoparticles.* JACS, 2002. **124**: p. 10596-10604.

32. C V Raman, K.S., Krishnan, *A New Type of Secondary Radiation.* Nature, 1928.

33. Smekal, A., *Zur Quantentheorie der Dispersion.* Naturwissenschaften, 1922. **11**: p. 873–875.

34. DAVID L. JEANMAIRE, R.P.V.D., *SURFACE RAMAN SPECTROELECTROCHEMISTRY PART I. HETEROCYCLIC, AROMATIC, AND ALIPHATIC AMINES ADSORBED ON THE ANODIZED SILVER ELECTRODE* J. Electroanal. Chem., 1977. **84**: p. 1-20.

35. González-Fuentes, M.A.M., E.; Saviñon-Flores, F.; Méndez-Albores, A. . *Principles of SERS.* 2021 April 21 2021 [cited 2023; Available from: https://encyclopedia.pub/entry/8851.

36. E. C. Le Ru, E.B., M. Meyer, P. G. Etchegoin, *Surface Enhanced Raman Scattering Enhancement Factors: A Comprehensive Study.* J. Phys. Chem. C 2007. **111**: p. 13794-13803.

37. Ding, S.Y., et al., *Electromagnetic theories of surface-enhanced Raman spectroscopy.* Chem Soc Rev, 2017. **46**(13): p. 4042-4076.

38. Kumar, S., et al., *Experimental Evidence of a Twofold Electromagnetic Enhancement Mechanism of Surface-Enhanced Raman Scattering.* The Journal of Physical Chemistry C, 2020. **124**(38): p. 21215-21222.

39. Trivedi, D.J., B. Barrow, and G.C. Schatz, *Understanding the chemical contribution to the enhancement mechanism in SERS: Connection with Hammett parameters.* J Chem Phys, 2020. **153**(12): p. 124706.

40. Kim, J., et al., *Study of Chemical Enhancement Mechanism in Non-plasmonic Surface Enhanced Raman Spectroscopy (SERS).* Front Chem, 2019. **7**: p. 582.

41. Langer, J., et al., *Present and Future of Surface-Enhanced Raman Scattering.* ACS Nano, 2020. **14**(1): p. 28-117.

42. Jia Denga, J.D., Paul Cohen, *Rapid Fabrication and Characterization of SERS Substrates.* Procedia Manufacturing, 2018. **26**: p. 580–586.

43. Liang, X., et al., *Carbon-based SERS biosensor: from substrate design to sensing and bioapplication.* NPG Asia Materials, 2021. **13**(1).

44. Suresh, V., et al., *Fabrication of Large-Area Flexible SERS Substrates by Nanoimprint Lithography.* ACS Applied Nano Materials, 2018. **1**(2): p. 886-893.

45. Pitt, C.W., et al., *Waveguiding Fresnel Lenses: Modelling and Fabrication.* Journal of Modern Optics, 1988. **35**(6): p. 1079-1111.

46. Hung, K.-Y. and J.-C. Liao, *The application of Fresnel equations and anti-reflection technology to improve inclined exposure interface reflection and develop a key component needed for Blu-ray DVD–micro-mirrors.* Journal of Micromechanics and Microengineering, 2008. **18**(7).

47. Ashley, P.R. and W.S.C. Chang, *Fresnel lens in a thin-film waveguide.* Applied Physics Letters, 1978. **33**(6): p. 490-492.

48. Querry, M.R., *Direct Solution of the Generalized Fresnel Reflectance Equations.* J. Opt. Soc. Am., 1969. **59**: p. 876-877.

49. Henderson, V.A., et al., *Comparative simulations of Fresnel holography methods for atomic waveguides.* New Journal of Physics, 2016. **18**(2).

50. Inampudi, S. and H. Mosallaei, *Fresnel Refraction and Diffraction of Surface Plasmon Polaritons in Two-Dimensional Conducting Sheets.* ACS Omega, 2016. **1**(5): p. 843-853.

51. Yang, W., *Modal Analysis of Slab Optical Waveguides: Fresnel Equations v.s. Wave Equations.* IEEE Southeastcon, 2014.

52. S.T. Chu, W.P.H., S.K. Chaudhuri, *Simulation and analysis of waveguide based optical integrated circuits.* Computer Physics Communication, 1991. **68**: p. 451—484.

53. Radhakrishnan, N. and L.C. Reese, *A Review of Applications of the Finite Element Method of Analysis to Problems in Soil and Rock Mechanics.* Soils and Foundations, 1970. **10**(3): p. 95-112.

54. Belytschko, T., R. Gracie, and G. Ventura, *A review of extended/generalized finite element methods for material modeling.* Modelling and Simulation in Materials Science and Engineering, 2009. **17**(4).

55. Suryanarayana, N.K., et al., *FDTD Analysis of Surface Plasmon Resonance Structure*, in *2021 2nd International Conference for Emerging Technology (INCET)*. 2021. p. 1-4.

56. YEE, K.S., *Numerical Solution of Initial Boundary Value Problems Involving Maxwell's Equations in Isotropic Media.* IEEE TRhTSACTIONS ON AXTEXXAS AND PROPAGATION, 1966. **14**(3).

57. Burger, S., J. Pomplun, and F. Schmidt, *Finite Element Methods for Computational Nano-optics*, in *Encyclopedia of Nanotechnology*, B. Bhushan, Editor. 2012, Springer Netherlands: Dordrecht. p. 837-843.

58. Mihailescu, I.N., *Synthesis and Modification of Nanostructured Thin Films.* Nanomaterials (Basel), 2019. **9**(10).

59. J. SINGH, D.E.W., *Nano and macro-structured component fabrication by electron beam-physical vapor deposition (EB-PVD).* JOURNAL OF MATERIALS SCIENCE, 2005. **40**: p. 1-26.

60. Abbott, W.M., et al., *Comparison of Metal Adhesion Layers for Au Films in Thermoplasmonic Applications.* ACS Appl Mater Interfaces, 2020. **12**(11): p. 13503-13509.

61. Benjamin, P., C. Weaver, and N.F. Mott, *The adhesion of evaporated metal films on glass.* 1961. **261**(1307): p. 516-531.

62. Sobahan, K.M.A., et al., *Nanostructured optical thin films fabricated by oblique angle deposition.* Advances in Natural Sciences: Nanoscience and Nanotechnology, 2011. **1**(4).

63. Boidin, R., et al., *Pulsed laser deposited alumina thin films.* Ceramics International, 2016. **42**(1): p. 1177-1182.

64. Flaherty, D.W., et al., *Low Temperature Synthesis and Characterization of Nanocrystalline Titanium Carbide with Tunable Porous Architectures.* Chemistry of Materials, 2009. **22**(2): p. 319-329.

65. Paik, S., et al., *Near-field sub-diffraction photolithography with an elastomeric photomask.* Nat Commun, 2020. **11**(1): p. 805.

66. Kimberly L. Berkowski, K.N.P., Qing Yu, Jeffrey S. Moore, *Introduction to Photolithography: Preparation of Microscale Polymer Silhouettes.* Journal of Chemical Education, 2005. **82**.

67. Anu Mary Ealia, S. and M.P. Saravanakumar, *A review on the classification, characterisation, synthesis of nanoparticles and their application.* IOP Conference Series: Materials Science and Engineering, 2017. **263**.

68. Mkam Tsengam, I.K., et al., *Transformation of Lipid Vesicles into Micelles by Adding Nonionic Surfactants: Elucidating the Structural Pathway and the Intermediate Structures.* J Phys Chem B, 2022. **126**(11): p. 2208-2216.

69. Alven, S. and B.A. Aderibigbe, *The Therapeutic Efficacy of Dendrimer and Micelle Formulations for Breast Cancer Treatment.* Pharmaceutics, 2020. **12**(12).

70. Aranda-Lara, L., et al., *Drug Delivery Systems-Based Dendrimers and Polymer Micelles for Nuclear Diagnosis and Therapy.* Macromol Biosci, 2021. **21**(3): p. e2000362.

71. Zhang, Y., et al., *Exosomes: biogenesis, biologic function and clinical potential.* Cell Biosci, 2019. **9**: p. 19.

72. Yoon, Y., et al., *Metal-Oxide Nanomaterials Synthesis and Applications in Flexible and Wearable Sensors.* ACS Nanosci Au, 2022. **2**(2): p. 64-92.

73. Mody, V.V., et al., *Introduction to metallic nanoparticles.* J Pharm Bioallied Sci, 2010. **2**(4): p. 282-9.

74. Abid, N., et al., *Synthesis of nanomaterials using various top-down and bottom-up approaches, influencing factors, advantages, and disadvantages: A review.* Adv Colloid Interface Sci, 2022. **300**: p. 102597.

75. Jorg Polte, T.T.A., Friedmar Delissen, Sergey Sokolov, Franziska Emmerling, Andreas F. Thunemann, Ralph Kraehnert, *Mechanism of Gold Nanoparticle Formation in the Classical Citrate Synthesis Method Derived from Coupled In Situ XANES and SAXS Evaluation.* J. AM. CHEM. SOC., 2010. **132**: p. 1296–1301.

76. JOHN TURKEVICH, P.C.S., JAMES HILLI, *A STUDY OF THE NUCLEATION AND GROWTH PROCESSES IN THE SYNTHESIS OF COLLOIDAL GOLD.* Discussion of the Faraday Society, 1951. **11**: p. 55-75.

77. J. Kimling, M.M., B. Okenve, V. Kotaidis, H. Ballot, A. Plech, *Turkevich Method for Gold Nanoparticle Synthesis Revisited.* J. Phys. Chem. B, 2006. **110**: p. 15700-15707.

78. Muriel K. Corbierre, N.S.C., Mark Sutton, Khalid Laaziri, R. Bruce Lennox, *Gold Nanoparticle/Polymer Nanocomposites: Dispersion of Nanoparticles as a Function of Capping Agent Molecular Weight and Grafting Density.* Langmuir, 2005. **21**: p. 6063-6072.

79. Chuanhui Huang, X.C., Zhenjie Xue, Tie Wang, *Effect of structure: A new insight into nanoparticle assemblies from inanimate to animate.* Sci. Adv, 2020. **6**.

80. Lee, M.S., et al., *Nanoparticle Assembly as a Materials Development Tool.* J Am Chem Soc, 2022. **144**(8): p. 3330-3346.

81. Borah, R., et al., *A Review on Self-Assembly of Colloidal Nanoparticles into Clusters, Patterns, and Films: Emerging Synthesis Techniques and Applications.* Small Methods, 2023. **7**(6): p. e2201536.

82. Badilescu, S., et al., *Gold Nano-Island Platforms for Localized Surface Plasmon Resonance Sensing: A Short Review.* Molecules, 2020. **25**(20).

83. Liu, Y., et al., *In situ visualization of self-assembly of charged gold nanoparticles.* J Am Chem Soc, 2013. **135**(10): p. 3764-7.

84. Mishra, B., A. Kumar, and B.P. Tripathi, *Polydopamine mediated in situ synthesis of highly dispersed Gold nanoparticles for continuous flow catalysis and*

*environmental remediation.* Journal of Environmental Chemical Engineering, 2020. **8**(5).

85. Golubina, E.N. and N.F. Kizim, *Interfacial Synthesis: Morphology, Structure, and Properties of Interfacial Formations in Liquid–Liquid Systems.* Russian Journal of Physical Chemistry A, 2021. **95**(4): p. 659-676.

86. Evgeny Smirnov, P.P., Michea´ l D. Scanlon, Hubert H. Girault, *Interfacial Redox Catalysis on Gold Nanofilms at Soft Interfaces.* ACS Nano, 2015. **9**: p. 6565–6575.

87. Liping Song, B.B.X., Qian Cheng, Xiaoyuan Wang, Xiaoning Luo, Xue Chen, Tao Chen, Youju Huang, *Instant interfacial self-assembly for homogeneous nanoparticle monolayer enabled conformal "lift-on" thin film technology.* Sci. Adv, 2021. **7**.

88. Tim, B., P. Blaszkiewicz, and M. Kotkowiak, *Recent Advances in Metallic Nanoparticle Assemblies for Surface-Enhanced Spectroscopy.* Int J Mol Sci, 2021. **23**(1).

89. J. B. Theeten, D.E.A., *ELLIPSOMETRY IN THIN FILM ANALYSIS.* Ann. Rev. Mater. Sci., 1981. **11**.

90. Jalili, N. and K. Laxminarayana, *A review of atomic force microscopy imaging systems: application to molecular metrology and biological sciences.* Mechatronics, 2004. **14**(8): p. 907-945.

91. I. Schmitz, M.S., G. Friedbacher, M. Grasserbauer, *Tapping-Mode AFM in Comparison to Contact-Mode AFM as a Tool for in Situ Investigations of Surface Reactions with Reference to Glass Corrosion.* Anal Chem, 1997. **69**: p. 1012-1018.

92. Korolkov, V.V., et al., *Ultra-high resolution imaging of thin films and single strands of polythiophene using atomic force microscopy.* Nat Commun, 2019. **10**(1): p. 1537.

93. Winey, M., et al., *Conventional transmission electron microscopy.* Mol Biol Cell, 2014. **25**(3): p. 319-23.

94. Kuchenbrod, M.T., et al., *Revisiting staining of biological samples for electron microscopy: perspectives for recent research.* Mater Horiz, 2021. **8**(3): p. 685-699.

95. Cao, B., H. Xu, and C. Mao, *Transmission electron microscopy as a tool to image bioinorganic nanohybrids: the case of phage-gold nanocomposites.* Microsc Res Tech, 2011. **74**(7): p. 627-35.

96. Brodusch, N., et al., *Scanning Electron Microscopy versus Transmission Electron Microscopy for Material Characterization: A Comparative Study on High-Strength Steels.* Scanning, 2021. **2021**: p. 5511618.

97. Mohammad, A., *Scanning electron microscopy (SEM): A review.* Proceedings of 2018 International Conference on Hydraulics and Pneumatics, 2018.

98. Ye, D.X., et al., *Growth of uniformly aligned nanorod arrays by oblique angle deposition with two-phase substrate rotation.* Nanotechnology, 2004. **15**(7): p. 817-821.

99. Xu, X. and Y. Ying, *Microbial Biosensors for Environmental Monitoring and Food Analysis.* Food Reviews International, 2011. **27**(3): p. 300-329.

100. Su, L., et al., *Microbial biosensors: a review.* Biosens Bioelectron, 2011. **26**(5): p. 1788-99.

101. Mohankumar, P., et al., *Recent developments in biosensors for healthcare and biomedical applications: A review.* Measurement, 2021. **167**.

102. MacDonald, H., et al., *Influence of Aptamer Surface Coverage on Small Target Recognition: A SPR and QCM-D Comparative Study.* The Journal of Physical Chemistry C, 2019. **123**(22): p. 13561-13568.

103. James P. Chambers , B.P.A., Leann L. Matta , Alex Weis , James J. Valdes, *Biosensor Recognition Elements.* Curr. Issues Mol. Biol., 2008. **10**: p. 1-12.

104. Naresh, V. and N. Lee, *A Review on Biosensors and Recent Development of Nanostructured Materials-Enabled Biosensors.* Sensors (Basel), 2021. **21**(4).

105. Karunakaran, R. and M. Keskin, *Biosensors: components, mechanisms, and applications*, in *Analytical Techniques in Biosciences*. 2022. p. 179-190.

106. Zhang, X., et al., *Immunosensors for Biomarker Detection in Autoimmune Diseases.* Arch Immunol Ther Exp (Warsz), 2017. **65**(2): p. 111-121.

107. Bohunicky, B. and S.A. Mousa, *Biosensors: the new wave in cancer diagnosis.* Nanotechnol Sci Appl, 2010. **4**: p. 1-10.

108. Guo, Z., et al., *Generalizable Protein Biosensors Based on Synthetic Switch Modules.* J Am Chem Soc, 2019. **141**(20): p. 8128-8135.

109. Gaviria-Arroyave, M.I., J.B. Cano, and G.A. Peñuela, *Nanomaterial-based fluorescent biosensors for monitoring environmental pollutants: A critical review.* Talanta Open, 2020. **2**.

110. Leopold, A.V., D.M. Shcherbakova, and V.V. Verkhusha, *Fluorescent Biosensors for Neurotransmission and Neuromodulation: Engineering and Applications.* Front Cell Neurosci, 2019. **13**: p. 474.

111. Vu, C.A. and W.Y. Chen, *Field-Effect Transistor Biosensors for Biomedical Applications: Recent Advances and Future Prospects.* Sensors (Basel), 2019. **19**(19).

112. Lim, H.J., et al., *Quartz crystal microbalance-based biosensors as rapid diagnostic devices for infectious diseases.* Biosens Bioelectron, 2020. **168**: p. 112513.

113. Peltomaa, R., et al., *Optical Biosensors for Label-Free Detection of Small Molecules.* Sensors (Basel), 2018. **18**(12).

114. McKeating, K.S., et al., *Antifouling Lipid Membranes over Protein A for Orientation-Controlled Immunosensing in Undiluted Serum and Plasma.* ACS Sens, 2019. **4**(7): p. 1774-1782.

115. BO LIEDBERG, C.N., INGEMAR LUNDSTROM, *SURFACE PLASMON RESONANCE FOR GAS DETECTION AND BIOSENSING.* Sensors and Actuators, 1983. **4** p. 299 - 304.

116. Bellassai, N., et al., *Surface Plasmon Resonance for Biomarker Detection: Advances in Non-invasive Cancer Diagnosis.* Front Chem, 2019. **7**: p. 570.

117. Dostalek J, H.J., *SPR Biosensors for Environmental Monitoring*, in *Surface Plasmon Resonance Based Sensors*, J. Homola, Editor. 2006, Springer: Berlin, Heidelberg.

118. Singh, P., *Surface Plasmon Resonance: A Boon for Viral Diagnostics*, in *Reference Module in Life Sciences*. 2017.

119. Olaru, A., et al., *Surface plasmon resonance (SPR) biosensors in pharmaceutical analysis.* Crit Rev Anal Chem, 2015. **45**(2): p. 97-105.

120. Maciej Adamczyk, P.G.M., Kevin Shreder, Zhiguang Yu, *Surface Plasmon Resonance (SPR) as a Tool for Antibody Conjugate Analysis.* Bioconjugate Chem., 1999. **10**: p. 1032−1037.

121. Topor, C.V., M. Puiu, and C. Bala, *Strategies for Surface Design in Surface Plasmon Resonance (SPR) Sensing.* Biosensors (Basel), 2023. **13**(4).

122. Vericat, C., et al., *Self-assembled monolayers of thiols and dithiols on gold: new challenges for a well-known system.* Chem Soc Rev, 2010. **39**(5): p. 1805-34.

123. Jiménez-Monroy, K.L., et al., *Surface plasmon resonance-based DNA microarrays: Comparison of thiol and phosphorothioate modified oligonucleotides.* physica status solidi (a), 2013. **210**(5): p. 918-925.

124. Hutsell, S.Q., et al., *High-affinity immobilization of proteins using biotin- and GST-based coupling strategies.* Methods Mol Biol, 2010. **627**: p. 75-90.

125. Belen, S.M., et al., *Optimized surface plasmon resonance immunoassay for staphylococcal enterotoxin G detection using silica nanoparticles.* Biochem Biophys Res Commun, 2021. **558**: p. 168-174.

126. Li, S., et al., *Dextran hydrogel coated surface plasmon resonance imaging (SPRi) sensor for sensitive and label-free detection of small molecule drugs.* Applied Surface Science, 2015. **355**: p. 570-576.

127. Hinman, S.S., et al., *Calcinated gold nanoparticle arrays for on-chip, multiplexed and matrix-free mass spectrometric analysis of peptides and small molecules.* Nanoscale, 2016. **8**(3): p. 1665-75.

128. Taylor, J.D., K.S. Phillips, and Q. Cheng, *Microfluidic fabrication of addressable tethered lipid bilayer arrays and optimization using SPR with silane-derivatized nanoglassy substrates.* Lab Chip, 2007. **7**(7): p. 927-30.

129. Hinman, S.S., et al., *On-Demand Formation of Supported Lipid Membrane Arrays by Trehalose-Assisted Vesicle Delivery for SPR Imaging.* ACS Appl Mater Interfaces, 2015. **7**(31): p. 17122-30.

130. Hinman, S.S., et al., *Mix and Match: Coassembly of Amphiphilic Dendrimers and Phospholipids Creates Robust, Modular, and Controllable Interfaces.* ACS Appl Mater Interfaces, 2017. **9**(1): p. 1029-1035.

131. Perez, L., et al., *Selective protein recognition in supported lipid bilayer arrays by tailored, dual-mode deep cavitand hosts.* Soft Matter, 2017. **13**(21): p. 3966-3974.

132. Ghang, Y.J., et al., *Labeled protein recognition at a membrane bilayer interface by embedded synthetic receptors.* Langmuir, 2014. **30**(34): p. 10161-6.

133. Liu, Y. and Q. Cheng, *Detection of membrane-binding proteins by surface plasmon resonance with an all-aqueous amplification scheme.* Anal Chem, 2012. **84**(7): p. 3179-86.

134. Huang, Y.Y., H.Y. Hsu, and C.J. Huang, *A protein detection technique by using surface plasmon resonance (SPR) with rolling circle amplification (RCA) and nanogold-modified tags.* Biosens Bioelectron, 2007. **22**(6): p. 980-5.

135. Ferreira de Macedo, E., et al., *Gold Nanoparticles Used as Protein Scavengers Enhance Surface Plasmon Resonance Signal.* Sensors (Basel), 2017. **17**(12).

136. Soelberg, S.D., et al., *Surface plasmon resonance detection using antibody-linked magnetic nanoparticles for analyte capture, purification, concentration, and signal amplification.* Anal Chem, 2009. **81**(6): p. 2357-63.

137. Baek, S.H., A.W. Wark, and H.J. Lee, *Dual nanoparticle amplified surface plasmon resonance detection of thrombin at subattomolar concentrations.* Anal Chem, 2014. **86**(19): p. 9824-9.

138. Matsishin, M., et al., *Selective Amplification of SPR Biosensor Signal for Recognition of rpoB Gene Fragments by Use of Gold Nanoparticles Modified by Thiolated DNA.* Nanoscale Res Lett, 2017. **12**(1): p. 252.

139. Kim, N.H., et al., *How to avoid a negative shift in reflection-type surface plasmon resonance biosensors with metallic nanostructures.* Opt Express, 2014. **22**(4): p. 4723-30.

140. Hong, X. and E.A. Hall, *Contribution of gold nanoparticles to the signal amplification in surface plasmon resonance.* Analyst, 2012. **137**(20): p. 4712-9.

141. Bantz, K.C., et al., *Recent progress in SERS biosensing.* Phys Chem Chem Phys, 2011. **13**(24): p. 11551-67.

142. Savinon-Flores, F., et al., *A Review on SERS-Based Detection of Human Virus Infections: Influenza and Coronavirus.* Biosensors (Basel), 2021. **11**(3).

143. Liu, X., et al., *SERS substrate fabrication for biochemical sensing: towards point-of-care diagnostics.* J Mater Chem B, 2021. **9**(40): p. 8378-8388.

144. Ambartsumyan, O., et al., *SERS-Based Biosensors for Virus Determination with Oligonucleotides as Recognition Elements.* Int J Mol Sci, 2020. **21**(9).

145. Chao, J., et al., *Nanostructure-based surface-enhanced Raman scattering biosensors for nucleic acids and proteins.* J Mater Chem B, 2016. **4**(10): p. 1757-1769.

146. Leong, Y.X., et al., *Surface-Enhanced Raman Scattering (SERS) Taster: A Machine-Learning-Driven Multireceptor Platform for Multiplex Profiling of Wine Flavors.* Nano Lett, 2021. **21**(6): p. 2642-2649.

147. Li, J.Q., et al., *Machine learning using convolutional neural networks for SERS analysis of biomarkers in medical diagnostics.* J Raman Spectrosc, 2022. **53**(12): p. 2044-2057.

148. Zhou, H., et al., *Machine learning-augmented surface-enhanced spectroscopy toward next-generation molecular diagnostics.* Nanoscale Adv, 2023. **5**(3): p. 538-570.

# Chapter 2: Theoretical Exploration of the Plasmonic Properties of Aluminum Thin Films

## 2.1 Introduction

Surface plasmon resonance (SPR) occurs when a photon interacts with a metal, forming a propagating wave along the interface between said metal and a dielectric. SPR detects the refractive index changes of a dielectric medium contacting a thin film metal.[1] Traditionally, gold has been used as the requisite metal due to its high plasmonic activity and relative chemical inertness.[2] Nevertheless, there has been a recent surge in research for alternative metals such as chromium, copper, and aluminum to replace gold as they offer unique benefits that gold lacks.[3, 4] Most notably regarding their availability, affordability, and that they can operate at a broader range and/or different wavelengths than gold, allowing for the investigation of other compounds and the detection of unique features that gold cannot monitor.[5-7]The application of these new materials for SPR sensing may lead to the development of materials with higher plasmonic activity than gold, drastically improving sensitivity and broadening investigation strategies. Recently, we demonstrated that aluminum is ideal for SPR imaging sensing as it is highly sensitive and stable under microfluidic conditions. [1] The stability of aluminum can be attributed to the oxide layer formed when the metal is exposed to air, which also provides unique antifouling properties. Aluminum's higher sensitivity can be attributed to the three electrons in its conduction band, whereas gold is limited to only one. The higher electron density present for aluminum allows for high negative permittivity to be achieved, giving a wider range of wavelengths for aluminum to be plasmonically active in. Aluminum’s manufacturing benefits over gold are centered on its higher abundance and more widely available

integration methods. [8] The most evident advantage regarding manufacturing properties when compared to gold is that aluminum inherently adheres to glass substrates, whereas gold requires an adhesion layer, which can complicate fabrication protocols. [8]

To date, the majority of research related to aluminum in combination with SPR has been limited to nanostructures such as nanorods or nanodiscs.[9] The use of aluminum in the Kretschmann configuration for SPR spectroscopy has only recently been explored.[1, 10] In these cases, these studies focus solely on simple aluminum thin films with native oxide layers. By changing the thickness of the oxide layer and varying the polarization from P to S polarized light, more aspects of the aluminum substrates can be explored. The transition to a waveguide is seen when the SPR response is suppressed by the increasing oxide thickness until the Self-referencing SPR sensors allow for more detailed information about the location of the refractive index changes, which can determine differences between surface and bulk changes in the refractive index.[11] Achieving self-referencing SPR generally requires methods that allow for the measurement of both long and short-range plasmonic waves, which are produced by different signals.[11-13] Short-range plasmons are more sensitive to changes in the refractive index of the surface as they lack the penetration depth into the dielectric that is present in the long-range plasmons. [14] By comparing the response between the long and short range plasmons, bulk changes can be differentiated from surface binding events.[15] These systems have been demonstrated with gold and similar plasmonic materials but not with aluminum.[11-13, 15] In addition, they frequently require additional substrates to layer on the metal, which makes them less accessible.

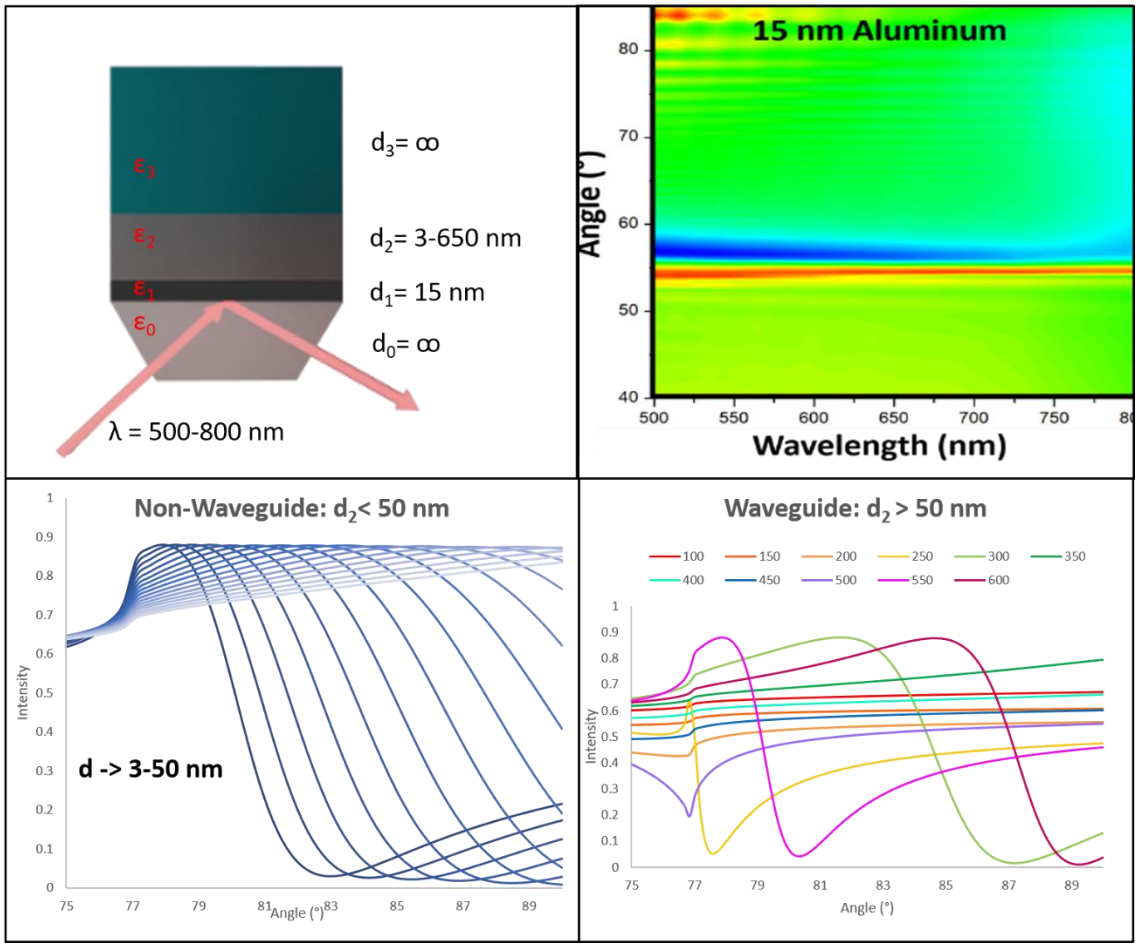


**Figure 2.1.** A scheme depicting the arrangement of the simulation parameters. A contour graphic demonstrating the repeated appearance of the plasmonic dip with increasing thickness of aluminum oxide. As the thickness of the oxide increases, the plasmonic dip disappears, as indicated by the lack of a blue line, but this reappears at a regular interval. This also occurs with both p and s-polarized light.

In the presented work, we explore the capabilities of aluminum as a self-referencing SPR sensor and the effects of thick aluminum oxide layers on the plasmonic behavior of aluminum thin films. By further exploring aluminum thin films, it matures the capabilities

of aluminum as a plasmonic sensor to rival gold even further. Studies were conducted using finite difference time domain (FDTD) and Fresnel calculations. Fresnel equations rely on the assumption that there are homogenous thin films, and they calculates the reflectance and transmission of incident light at an interface of different refractive indexes. FDTD solves for magnetic and electrical fields using Maxwell's equation in well-defined Yee cells. The Yee cell is the individual unit for which Maxwell's equation is solved. The Yee cell defines the resolution of the simulation and when combined, allows for Maxwell's equation to effectively be solved for the entire system. The size of the Yee cell is dependent on the permittivity and permeability of the material, the time step, and the wavelength of the incident light.[16] Previous simulations of aluminum have demonstrated a sharp peak in reflectivity before the well-established plasmonic dip that is common amongst plasmonic metals.[17] This feature of the aluminum plasmonic response can be ascribed to the 3 electrons present in the conducting band.[1, 17]

**2.2 Methods:**

Simulations were conducted with either FDTD or Fresnel calculations. In either case, the n and k values for aluminum and aluminum oxide are procured from. [17, 18] For FDTD calculations, EM Explorer was used. For Fresnel calculations, Winspall was used, as well as a custom Fresnel calculator made in R. FDTD calculations used the following settings: a Yee cell size of 5 nm with an incident wavelength of 650 nm. Original determinations for the waveguide capabilities of the aluminum were conducted with FDTD. However for the larger data sets, Fresnel calculations were used to optimize computational time. For the Fresnel calculations an incident wavelength of 650 nm was

used. The thickness of the aluminum was a constant 15 nm, as that was found to be the optimized thickness in our previous work.[1] The naturally occurring oxide layer on aluminum is approximately 3 nm, this was used as baseline, and the thickness was increased by 1 nm increments until 650 nm was reached. For the sensitivity contour maps, the thickness of the AlOx was increased to 1200 nm, and the wavelength range was also increased from 250-1200 nm. The sensitivity to the refractive index was identified by sequentially increasing the refractive index of the dielectric from 1.333 to 1.342. The minimum angle was found, and the change of angle relative to refractive index was used for the sensitivity. To determine the differences between bulk and surface changes several factors were changed; refractive index of the dielectric by changing the replicating solvent of the bulk system, increasing the thickness of the oxide layer, and changing the composition of the tested material.

**2.3 Results and Discussion:**

Initial analysis of the simulated spectra compared the phase-shifted response of the Al thin film to refractive index changes of the dielectric. Phase-shifted SPR response is calculated based upon the following equation: $\frac{R_p}{R_s} = \tan(\Psi) * e^{\Delta * i}$ wherein $R_p$ is the reflected intensity of p-polarized light, $R_s$ is the reflected intensity of s-polarized light, $\Psi$ is the Psi-shift and $\Delta$ is the phase-shift. Calculations of phase-shifted and Psi-shifted responses have been demonstrated to increase the sensitivity of the plasmonic surfaces.[19] Notably, the shape of the plasmonic dip changes as expected, but any change to refractive index change can be treated similarly to traditional SPR response. Therefore, both fixed

angle and plasmonic dip tracking can be the focus of refractive index sensitivity. The thickness of the oxide layer was increased to better understand the possibilities of the surface and unique plasmonic properties that can be predicted. To optimally simulate the series of Fresnel equations, a homemade program was used that can account for the changes in refractive index with wavelength, based upon experimental data, and can simulate a variety of oxide thicknesses.

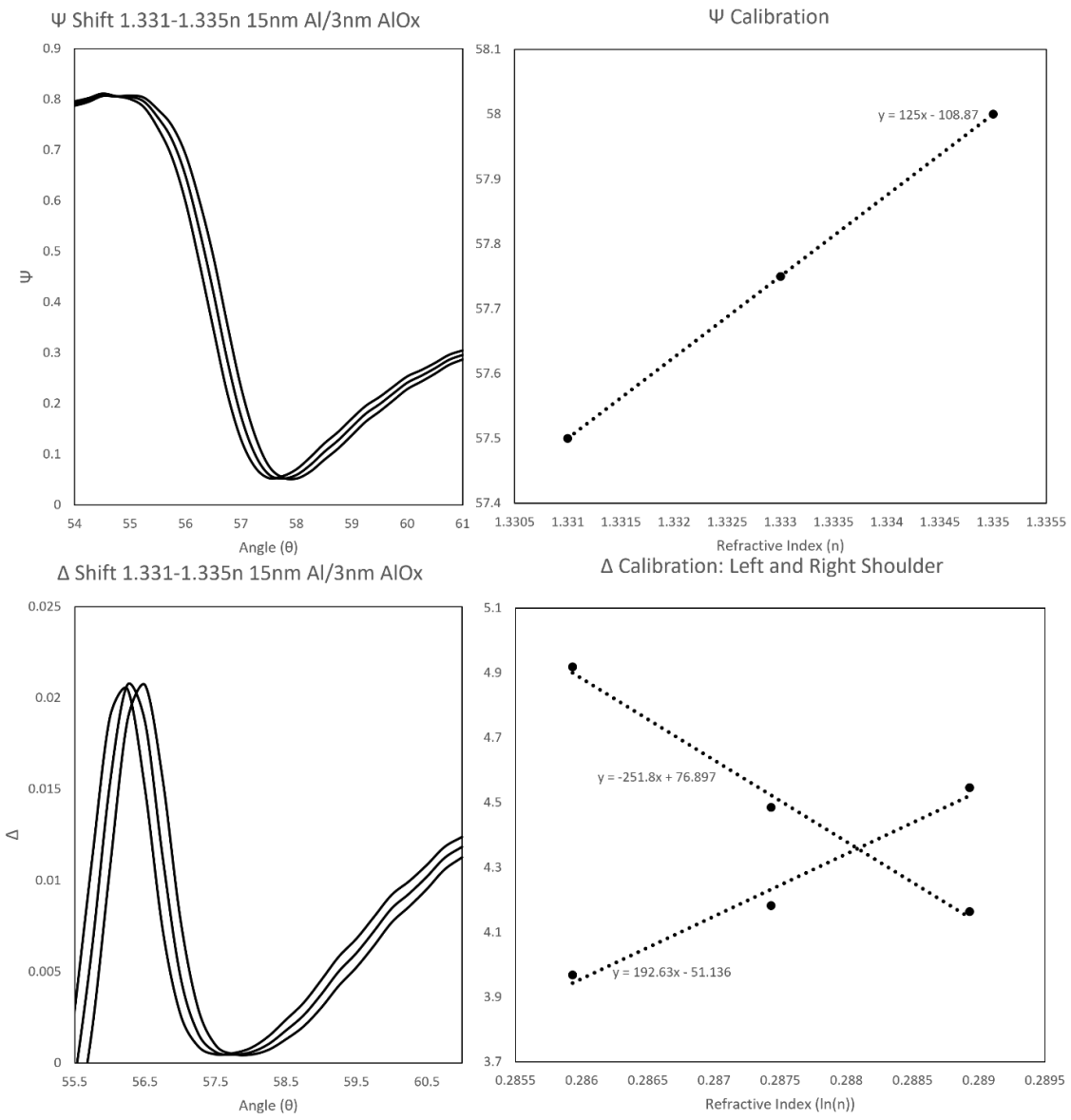


**Figure 2.2** Psi-Shift response and sensitivity to refractive index changes. A calibration curve demonstrating the linear sensitivity to refractive index based upon plasmonic dip tracking. Phase shift response and sensitivity to refractive index changes. Calibration curves are formed with a fixed angle on both sides of the peak.

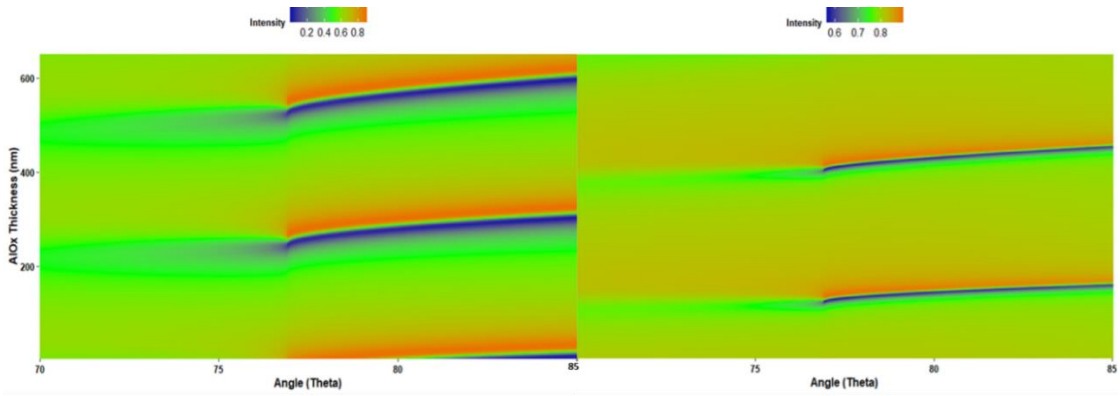


**Figure 2.3** By increasing the aluminum oxide thickness, the disappearance of plasmonic response and the formation of the waveguide can be seen with p-polarized light (left) and with s-polarized light (right). Periodicity is seen, as, after the formation of the waveguide, the signal is lost again until it returns. The s-polarized response produces a much sharper dip in reflectivity than the p-polarized.

By increasing the thickness of the aluminum oxide layer, a pattern in the spectrum can be observed, as shown in Figure 3. The observed pattern in Figure 1 indicates that as the oxide layer's thickness increased, the signature plasmonic dip of aluminum in p-polarized light would disappear. However, at specific thicknesses, the plasmonic response would reappear at the particular thicknesses of interest at 300 and 600 nm**.** A similar trend was observed when s-polarized light was investigated, as shown in Figure 3. Under standard metal-based plasmonic conditions, a plasmonic reflectivity dip is not expected in s-polarized light. However, a dip can clearly be observed at specific aluminum oxide

thicknesses. These effects are indicative of the formation of a waveguide. This is the expected behavior of a thin film with high refractive index material layered on top.[20] The specific thickness with which the plasmonic response is present depends on the wavelength of the incident light.[20] In addition, it can be noted that the thickness with which the dip is observed is correlated to a specific ratio relating to the wavelength. This can be seen when the wavelength varies, and the ratio remains similar amongst both p and s-polarized systems. If we assume that n is the wavelength of light, n-100 is a consistent thickness of aluminum oxide that provides plasmonic dips. With regards to the s-polarized light, if we again assume that n is the wavelength of light then the resonant thickness of aluminum oxide is n*⅔. This can be seen in Figure 3. The presence of a plasmonic dip does not necessarily mean the plasmon is sensitive to refractive index changes. [21] Normally, the range of the plasmon is considered to be approximately equivalent to the wavelength of light used [20] and the plasmon would decay exponentially, so there would be very little or

no change in the spectrum in our system as the aluminum oxide is 600 nm thick. However, we can see in our results that this is not the case, indicating a waveguiding effect.

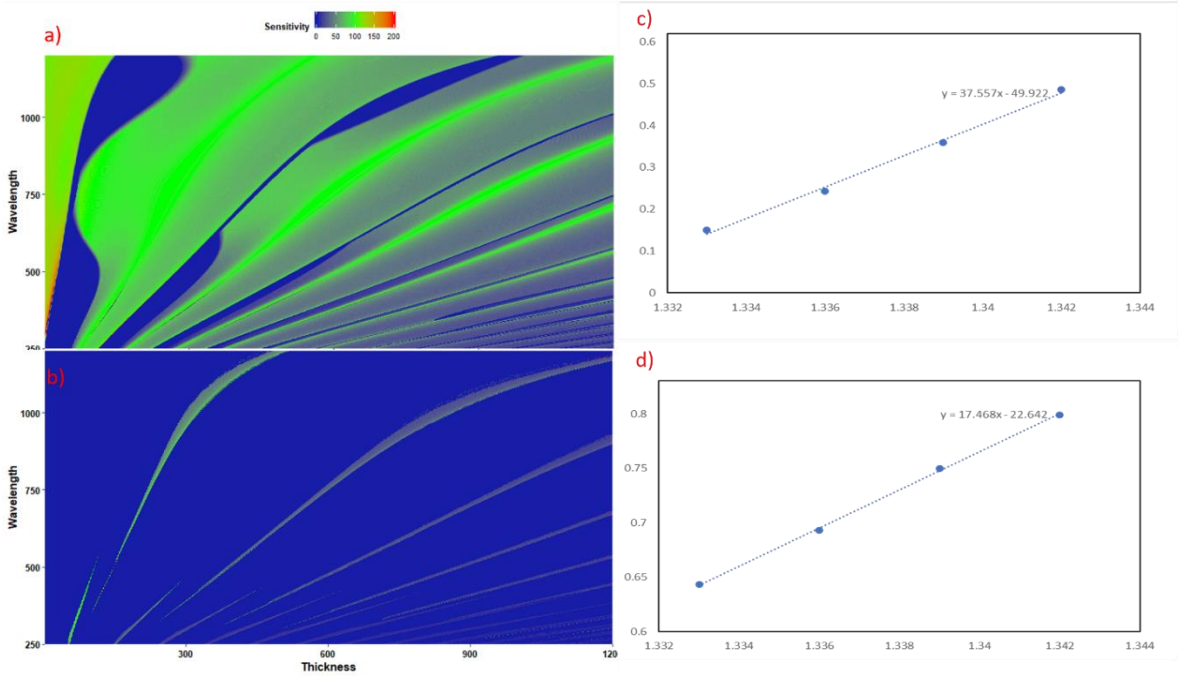


**Figure 2.4** A contour map demonstrating the relationship between sensitivity to refractive index change, the wavelength of the incident light, and the thickness of the aluminum oxide. This is done with p-polarized (a) and s-polarized light (b). A calibration curve of the p-polarized (c) and s-polarized (d) systems at their respective sensitive thicknesses, 600 and 450 nm. The calibration is achieved using a fixed-angle methodology.

Through analysis of both the p and s-polarized sensitivities to refractive index change and varying the wavelength, an optimal thickness for either s or p-polarized light is found. These thicknesses can then be used for further study to explore the ability to be sensitive to refractive index change with both p and s-polarized light. By varying the refractive index of the dielectric above the oxide, as if it were water, we can determine

whether the system was sensitive to refractive index changes. While the high refractive index material distances the area of changing refractive index from the surface of the aluminum, sensitivity to refractive index changes above the oxide are still present. In addition, sensitivity is found with both P and S polarization, allowing for multiple aspects of the plasmonic activity to be taken advantage of for sensing. This is in direct contrast to most plasmonic thin films that do not have waveguide behaviors, where s-polarized light exhibits no plasmonic response. [22] The sensitivity of the surface was determined with a fixed angle methodology for the specific calibration curves and with the minimum intensity for the contour graphs in Figure 4. [1] Through this we determined the sensitivity of the surface to the refractive index. It can be seen in Figure 4 that the p-polarized light is more sensitive to refractive index changes than the s-polarized system. This is because the plasmonic dip in the s-polarized system has less intensity, so any observed changes will be comparatively lower. However, the specific thickness of the aluminum oxide is important to maintain the sensitivity of the surface, as certain thicknesses produce a dampened or non-existent plasmonic dip. The p-polarized light is more sensitive to refractive index changes than the s-polarized light, but the differences in response to refractive index changes can be explored past the sensitivity changes by looking at the overall shape of the plasmonic response curve. Traditionally, the distance that a surface plasmon would be expected to travel is half of the wavelength of light used to excite it.[23] In addition, because the wave decays exponentially, the signal shift further from the surface is decreased substantially.[24, 25] However, in our system, it can be seen that past 600 nm from the

surface, there is still a sensitivity to refractive index changes, and therefore this is indicative of the waveguide effect.[11, 25-28]

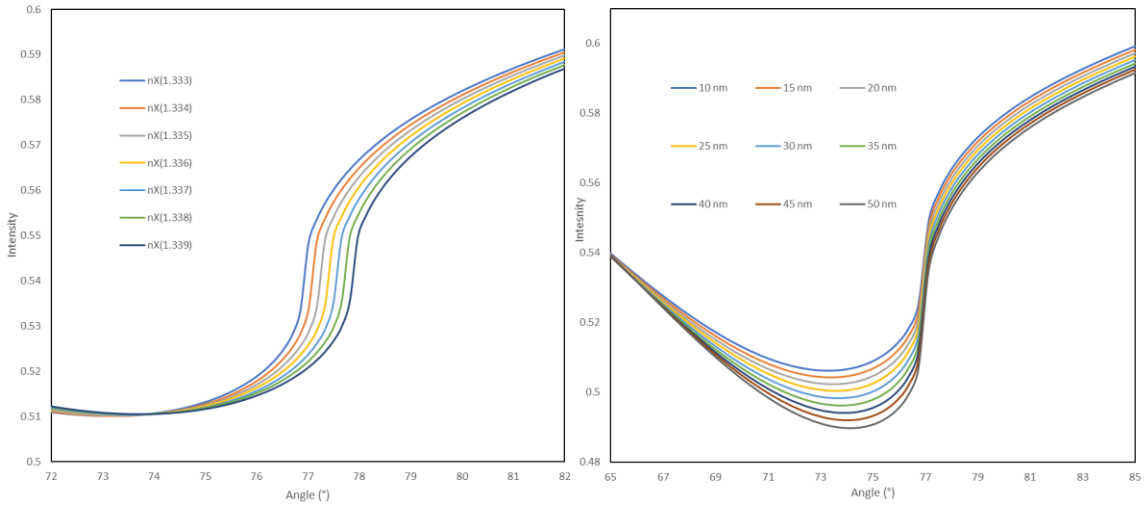


**Figure 2.5** Differences in the bulk (right) and surface (left) refractive index changes with p-polarized light. The thickness of the aluminum oxide is optimal for s-polarized sensing but still allows for the p-polarized differentiation of surface and bulk effects. The bulk changes are replicated by increasing the refractive index of the dielectric, whereas the surface changes are replicated through an increasing thickness of a high refractive index material.

Differences in bulk and surface changes of the material above the oxide coating can be differentiated based on the changes in the shape of the curve with surface and bulk changes. This is caused by the differentiation between long-range and short-range surface plasmon polaritons, so changes in the surface will only affect the shorter-ranged polaritons, causing the plasmonic curve to respond differently.[14] Whereas with bulk changes, both the long-range and short-range polaritons are affected, causing the entire curve to shift.[14]

This is referred to as a self-referential sensor [11, 12], which allows for a way to determine differences between bulk changes and surface binding events.[11-13] In this case, the s-polarized system is agnostic to differences between bulk and surface changes, while the p-polarized system exhibits differing curve structures. These results are obtained at an aluminum oxide thickness at which the significant plasmonic dip is found with s-polarized light, and the p-polarized light has a regressed response. Regardless of this, the p-polarized light still shifts with changes to the refractive index. By comparing the change in the reflectivity intensity of the p-polarized to s-polarized light, a ratio can be determined that represents the relative sensitivity of the p-polarized system. The ratio allows for the determination of the specific sensitivity to surface changes controlled by the aforementioned changes affects to the s-polarized response. By comparing the ratios in the surface case, 0.0722, to the bulk case, .005365, we can see that the relative changes of the p-polarized light compared to the s-polarized light are preferential for surface changes compared to bulk changes because the same thickness of aluminum oxide is used for both the p and s polarization systems, a singular chip can be used for the self-referential sensor. In addition to being a self-referential sensor it is advantageous as it uses a single wavelength, and only the polarizer needs to be shifted 90° [11, 12, 15]. This allows for the chip to be compatible with existing SPR sensing systems, something that to date has not been available.[1, 29]

**2.4 Conclusions:**

In this work, we have demonstrated the capability of aluminum/aluminum oxide plasmonic sensors for use as waveguides and self-referential sensors. The advantages of

aluminum over gold are being more thoroughly explored, as differing functionalities are being found that allow for the sensors to provide more information. By utilizing the unique advantages of aluminum and aluminum oxide, we have demonstrated the ability to create a self-referential sensor that is compatible with already existing SPR instrumentation and deepens the sensing capabilities of said instruments. In addition, we have explored a wide variety of conditions for these chips through analyzing the sensitivity to refractive index changes with changing wavelength and oxide thickness. Further work based upon this data can be performed experimentally, depositing AlOx onto an aluminum thin film, and determining the sensitivity in an applied fashion.

## 2.5 References:


1. Lambert, A.S., et al., *Plasmonic Biosensing with Aluminum Thin Films under the Kretschmann Configuration.* Anal Chem, 2020. **92**(13): p. 8654-8659.
2. Prabowo, B.A., A. Purwidyantri, and K.C. Liu, *Surface Plasmon Resonance Optical Sensor: A Review on Light Source Technology.* Biosensors (Basel), 2018. **8**(3).
3. Rodriguez, R.D., et al., *Aluminum and copper nanostructures for surface-enhanced Raman spectroscopy: A one-to-one comparison to silver and gold.* Sensors and Actuators B: Chemical, 2018. **262**: p. 922-927.
4. Ai, K., et al., *Localized surface plasmon resonance properties and biomedical applications of copper selenide nanomaterials.* Materials Today Chemistry, 2021. **20**.
5. Tanabe, I., et al., *Aluminum Film Thickness Dependence of Surface Plasmon Resonance in the Far- and Deep-ultraviolet Regions.* Chemistry Letters, 2017. **46**(10): p. 1560-1563.
6. Prabowo, B.A., et al., *Nano-film aluminum-gold for ultra-high dynamic-range surface plasmon resonance chemical sensor.* Frontiers of Optoelectronics, 2019. **12**(3): p. 286-295.
7. Pathak, N.K., et al., *Tuning of the surface plasmon resonance of aluminum nanoshell near-infrared regimes.* Phys Chem Chem Phys, 2019. **21**(18): p. 9441-9449.
8. Benjamin, P., C. Weaver, and N.F. Mott, *The adhesion of evaporated metal films on glass.* 1961. **261**(1307): p. 516-531.
9. Lee, K.-L., M.-L. You, and P.-K. Wei, *Aluminum Nanostructures for Surface-Plasmon-Resonance-Based Sensing Applications.* ACS Applied Nano Materials, 2019. **2**(4): p. 1930-1939.
10. Pletincx, S., et al., *In Situ Methanol Adsorption on Aluminum Oxide Monitored by a Combined ORP-EIS and ATR-FTIR Kretschmann Setup.* The Journal of Physical Chemistry C, 2018. **122**(38): p. 21963-21973.
11. Zhang, P., et al., *Self-Referenced Plasmon Waveguide Resonance Sensor Using Different Waveguide Modes.* Journal of Sensors, 2015. **2015**: p. 1-10.
12. Kohandani, R. and S.S. Saini, *Self-Referencing Plasmonic Array Sensors.* Plasmonics, 2020. **15**(5): p. 1359-1368.
13. Brigo, L., et al., *Short and long range surface plasmon polariton waveguides for xylene sensing.* Nanotechnology, 2013. **24**(15): p. 155502.

14. Avner Yanai, U.L., *The role of short and long range surface plasmons for plasmonic focusing applications.* Optics Express, 2009. **17**(16): p. 14270-14280.

15. Fang Yu, W.K., *Immunosensor with Self-Referencing Based on Surface Plasmon Diffraction.* Anal. Chem., 2004. **76**.

16. Schneider, J.B., *Understanding the Finite-Difference Time-Domain Method.* 2021.

17. Rakic, A.D., *Algorithm for the determination of intrinsic optical constants of metal films: application to aluminum.* Applied Optics, 1995. **34**.

18. Boidin, R., et al., *Pulsed laser deposited alumina thin films.* Ceramics International, 2016. **42**(1): p. 1177-1182.

19. Huang, Y.H., et al., *Detecting Phase Shifts in Surface Plasmon Resonance: A Review.* Advances in Optical Technologies, 2012. **2012**: p. 1-12.

20. Raether, H., *Surface Plasmons on Smooth and Rough Surfaces and on Gratings* Springer Tracts in Modern Physics, ed. G. Hohler. Vol. 111. 1988: Springer.

21. Shen, Y., et al., *Plasmonic gold mushroom arrays with refractive index sensing figures of merit approaching the theoretical limit.* Nat Commun, 2013. **4**: p. 2381.

22. Tobing, L.Y.M., et al., *Polarization invariant plasmonic nanostructures for sensing applications.* Sci Rep, 2017. **7**(1): p. 7539.

23. Linda S. Jung, C.T.C., *,† Timothy M. Chinowsky,‡ and a.S.S.Y. Mimi N. Mar, *Quantitative Interpretation of the Response of Surface Plasmon Resonance Sensors to Adsorbed Films.* Langmuir, 1998. **14**: p. 5636-5648.

24. *<24-Nazarova.pdf>*.

25. Vala, M., et al., *Surface Plasmon Resonance Sensing on Naturally Derived Membranes: A Remyelination-Promoting Human Antibody Binds Myelin with Extraordinary Affinity.* Anal Chem, 2018. **90**(21): p. 12567-12573.

26. Ong, B.H., X. Yuan, and S.C. Tjin, *Bimetallic Silver–Gold Film Waveguide Surface Plasmon Resonance Sensor.* Fiber and Integrated Optics, 2007. **26**(4): p. 229-240.

27. Steinberger, B., et al., *Dielectric stripes on gold as surface plasmon waveguides: Bends and directional couplers.* Applied Physics Letters, 2007. **91**(8).

28. Suárez, I., et al., *Propagation length enhancement of surface plasmon polaritons in gold nano-/micro-waveguides by the interference with photonic modes in the surrounding active dielectrics.* Nanophotonics, 2017. **6**(5): p. 1109-1120.

29. Malinick, A.S., et al., *Detection of Multiple Sclerosis Biomarkers in Serum by Ganglioside Microarrays and Surface Plasmon Resonance Imaging.* ACS Sens, 2020. **5**(11): p. 3617-3626.

## Chapter 3: Realization and Optimization of an Aluminum SPR Substrate

### 3.1 Introduction

Surface plasmon resonance (SPR) spectroscopy is a well-established analytical technique for label-free quantification of molecular interactions on a surface.[1] The method relies upon the formation of an evanescent wave which is highly sensitive to refractive index changes at the surface of a thin metallic film from which it resonates.[2] The metal layer used has traditionally been gold due to its high plasmonic activity and inert chemical reactivity. Recently, interest is being invested toward other metals such as chromium, copper, and aluminum as plasmonic materials.[3-6] Aluminum is attractive as it has a high electron density (3 electrons per atom in its conduction band versus 1 electron for gold and silver) and a generally higher negative permittivity than silver or gold.[7] Therefore, aluminum demonstrates a plasmonic resonance in a very large wavelength range, with plasmonic activity from the ultraviolet to infrared range. Aluminum is also appealing for commercial applications due to high abundance, low-cost, and practical integration into manufacturing processes such as CMOS.[3]

Before this work, practical studies of aluminum as a plasmonic material has been delegated almost entirely to nanostructures, with a range of structures explored such as nanorods, nanodiscs and others.[8-15] Aluminum as a surface-enhanced Raman scattering (SERS) substrate has also been reported.[16, 17] The usage of thin film aluminum coupled to an ATR coupler (ie. a prism) in the standard Krestschmann configuration for SPR spectroscopy has not been thoroughly studied. Due to the unique ability of aluminum to

produce plasmonic response under UV excitation, some reports have taken advantage of this to investigate the resonances in the UV region to probe organic and biological systems with strong UV absorptions.[18, 19] Other attempts with aluminum thin film studies suffered due to substrate stability and subsequently failed to produce meaningful results. [20]

In this chapter, plasmonic characterization is presented of Al thin films in ATR mode, employing both FDTD and the Fresnel models to predict the surface plasmon polariton (SPP) behavior on the aluminum film and conducting an extensive experimental study to understand and verify the fundamental SPR characteristics of the metal. The analysis of thin film aluminum broadens the scope of SPR sensors and allows for new surface chemistries as well as increased sensitivity compared to the traditional gold.

## 3.2 Methods and Materials

### Reagents

Aluminum, gold and chromium targets for electronbeam evaporation were acquired as pellets of 0.9999% purity from Kurt J. Lesker (Jefferson Hills, PA). Sodium chloride was obtained from Fisher Scientific (Pittsburgh, PA). BK-7 glass substrates for deposition were obtained from Corning (Painted Post, NY).

### FDTD&Fresnel Simulations

FDTD based simulations were performed using EM Explorer software. Simulations were conducted in a similar manner to previously reported, and parameters were as follows.[21] Real and imaginary parts of the Al and Al2O3 refractive indices across

the wavelength spectrum were obtained from literature.[7, 22, 23] The Al thickness was varied from 9 nm to 18 nm, and Al2O3 was kept at a consistent 3 nm. The Yee cell size was set to be 5 nm cubes. The light was set to be p-polarized. This was then used to probe the plasmonic activity with 500-800 nm wavelength of light with a range of incident angles from 40-85 degrees. Literature sources were used to obtain values of Al and Au, and for value of Al2O3 for the purposes of the Fresnel simulations. [23]Simulation was conducted as previously reported and was based on standard Fresnel multi-layer calculation model.[24] For Au simulation, Al and Al2O3 were replaced with 50 nm Au.

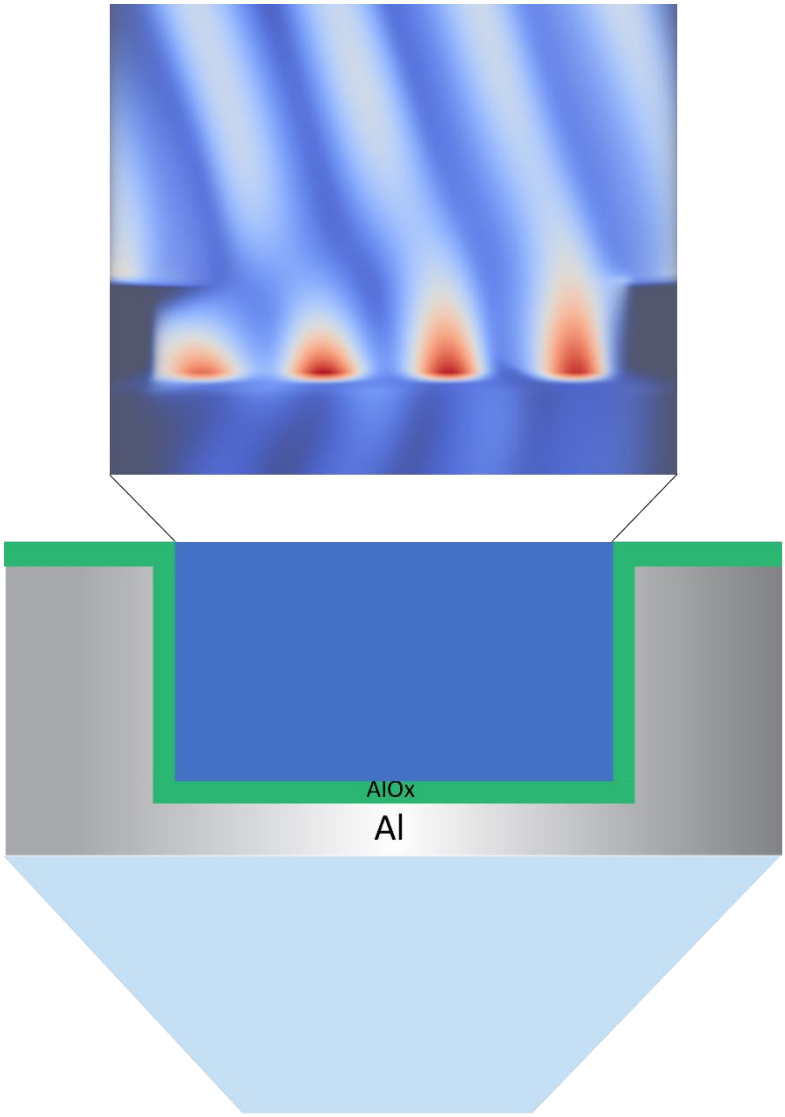


**Figure 3.1.** FDTD simulations of aluminum wells. The formation of the evanescent wave can be seen in the simulation which is contained by the walls of well.

**SPR substrate fabrication**

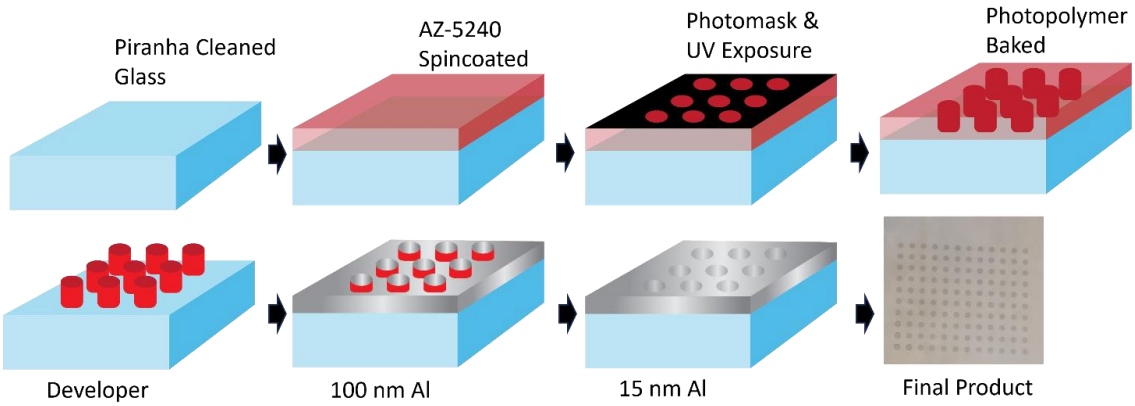


**Fig 3.2.** Step-by-step methodology to fabricate aluminum SPR arrays.

Both SPR and SPR imaging substrates were fabricated using BK-7 glass microscope slides as the initial substrate. Slides were cleaned using boiling piranha solution (3:1 H2SO4:30% H2O2) for 1 hr, followed by rinsing with ultrapure water and ethanol and drying with compressed nitrogen gas. For conventional SPR chips, 15 nm (5.0 Å/s) of aluminum was evaporated onto one side of the slide via electron beam physical vapor deposition. (EBPVD) (Temescal, Berkeley, CA). For Au chips, evaporation instead consisted of 2 nm of chromium (0.5 Å/s) and 50 nm of gold (2.0 Å/s). All EBPVD was conducted at 5 × 10-6 Torr in a Class 1000 cleanroom facility (UCR Center for Nanoscale Science and Engineering). SPR imaging arrays were fabricated in accordance to previously described methods22 with some modification. Cleaned glass slides were spin-coated with hexamethyldisilazane (HMDS) to promote adhesion, followed by AZ5214E, both at 4000 RPM for 45 s. After baking for 1 min at 110° C, the photoresist was patterned by UV exposure using a Karl-Suss MA-6 system and a photomask, followed by development with AZ400K developer and standard protocols. 150 nm of Al (or 2 nm Cr/200 nm Au for gold

microarray) was then evaporated onto the surface via EBPVD to form the well walls. The photoresist well spots were then removed using acetone, after which an additional 15 nm of aluminum (or 2 nm Cr/50 nm Au) was evaporated to form the well surface. The final microarrays consisted of a 10 × 10 array of circular wells that were 165 nm (or 250 nm for gold microarray) deep and 600 μm in diameter. Both SPR and SPRi substrates were stored in air for 3 days prior to use.

**SPR Spectroscopy**

A dual-channel NanoSPR6-321 spectrometer (Nano SPR, Chicago, Il) was used for all spectroscopic measurements for SPR. The device used a GaAs semiconductor laser light source ($\lambda$ = 670 nm), a manufacturer-supplied prism of high refractive index (n = 1.616) and a 30 μL flow cell. Fabricated chips were inserted, and online analysis was conducted in an angular scanning mode that tracked the resonance angle every 5 s while also collecting the angular spectrum at each point. For bulk refractive index testing, 18 MΩ ultrapure water was flowed at a rate of 5 mL/hr as a baseline and NaCl solutions were flowed over the surface. Sodium chloride solutions were diluted from NaCl salt with ultrapure water, and refractive index of each solution was measured with an Abbe refractometer (American Optics, Buffalo, NY). Intensity measurements were extracted from angular spectra at a constant angle at ~20% of the maximum to ensure maximum sensitivity for both Al and Au chips.

**3.3 Results and Discussion**

**AFM**

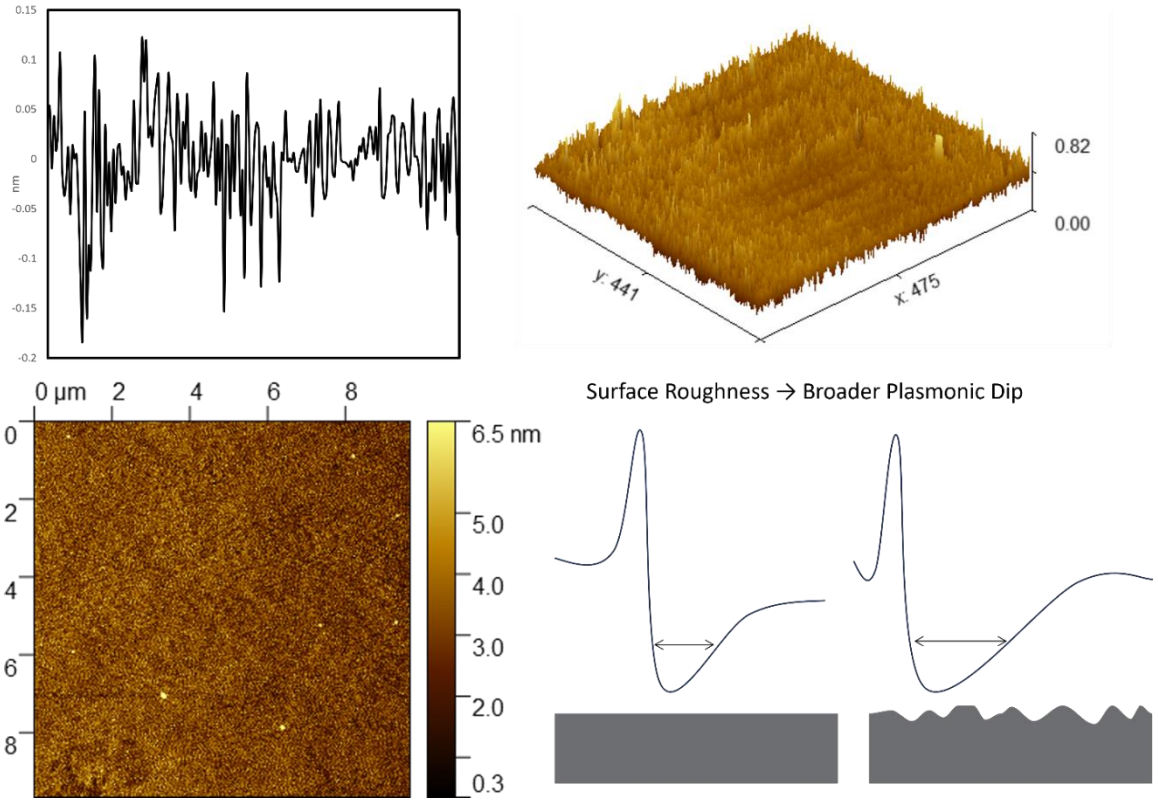


**Figure 3.3** AFM of the thin film aluminum substrate, in 1D, 2D, and 3D representations. In addition, the effects of surface roughness on the plasmonic response.

Surface characterizations through AFM measurements is key in the development of SPR substrates due to the direct correlation between surface roughness and plasmonic response. As the surface roughness increases the overall plasmonic dip broadens due to the wider ranges of matching conditions.[25] The sensitivity of the SPR chip is directly dependent on the width of the dip due to the two main methods, minima tracking and fixed angle modes, being effected. As the dip broadens the specific determination of the minima increases in difficulty due to a broader base leading to lower sensitivity. In the fixed angle

mode, the slope of the plasmonic dip is shallower and therefore less sensitive to a change in refractive index. Due to the inherent oxidation of aluminum under atmospheric conditions, the oxide layer was of concern with regards to the surface roughness of the sensor chips. The AFM of the aluminum thin film demonstrated a surface roughness of 1.5 nm RMS which is comparable to the surface roughness of the conventional SPR substrate of gold. The AFM indicates that surface stability of the aluminum substrate is not a concern as the oxide is smooth and protects the underlying metal from further oxidation. The smooth oxide also supports the simulation results which would assume ideal conditions leading to fewer differences between the computed and experimental cases.

**SPR Analysis**

Initial SPR simulations of aluminum were performed with FDTD simulations to determine the optimal thickness of the aluminum substrate as well as the range of wavelengths that provide optimal plasmonic response. This was performed through iterative measurements of the reflected light through a series of angles and aluminum thicknesses. In the construction of the simulation parameters, Yee cell size is set, with limitations based upon the wavelength of the incident light.[26] The dimensions of the Yee cell must be small enough to resolve the incident light in the specified time intervel, as well to resolve the modeled structures. In traditional gold SPR substrates, a thickness between 45-50 nm is ideal for the gold, with a ~2 nm adhesion layer, of either chromium or titanium.[27] However, in the aluminum system no adhesion layer[28] is needed allowing for the removal of it from the simulation, and due to the higher absorption of aluminum relative to gold, a film of thicknesses between 9-18 nm were explored. In addition to the thickness,

the wavelength of the incident light was probed. Aluminum is predicted to have a broader range of frequencies which will elicit plasmonic response compared to gold which is generally excited with a range of 600-750 nm light.[29] The optimal thickness of the aluminum for 650 nm light was determined to be 12 nm of aluminum with a 3 nm oxide layer assumed. 650 nm was chosen as the wavelength for thickness optimization due to existing SPR instrumentation using such an excitation source.

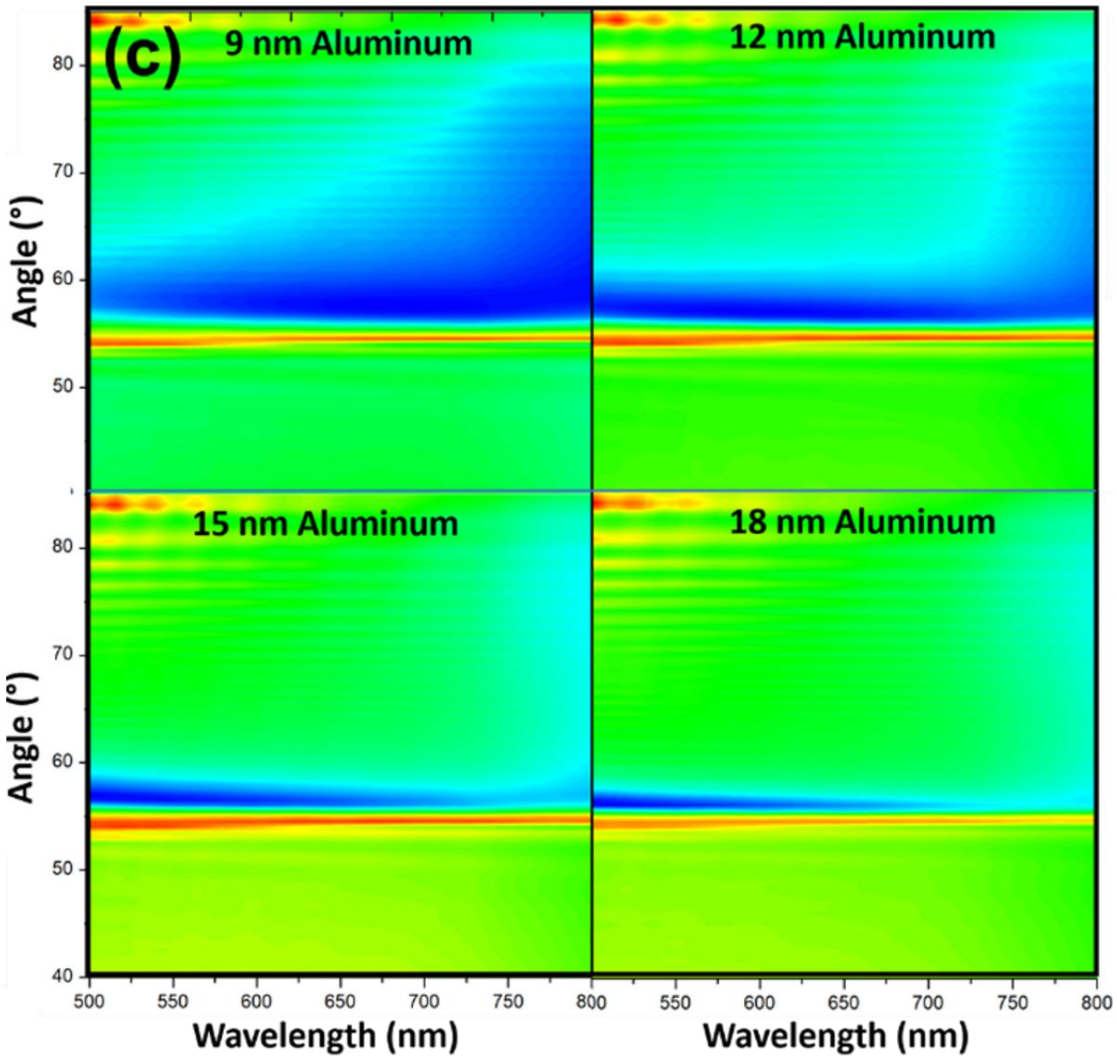


**Figure 3.4** Contour maps demonstrating the formation of the plasmonic response in response to changing angle and wavelength at a variety of thicknesses.

SPR results are compared based upon the Fresnel and FDTD calculations. Gold and aluminum surfaces were compared to each other based upon the sensitivity to refractive index changes, and overall shape of the plasmonic dip. The two main methodologies to

sense refractive index changes with a plasmonic chip in the Krestchmann configuration is either minima tracking or a fixed angle methodology which relies upon the slope of the dip.[30, 31] In the analysis of the Fresnel results it was determined that with minima tracking methods, gold outperformed aluminum due to the broader dip in the aluminum plasmonic response as shown in Figure 5. However, aluminum was superior regarding fixed angle sensitivity in two distinct ways. First, the aluminum substrate demonstrated improved sensitivity to refractive index changes as shown in Figure 5, although this effect is dependent upon the starting position on the plasmonic dip. Generally, in the usage of gold SPR substrates, the fixed angle is set to be approximately 20%-30% of the maximum insensity, however in the case of aluminum this differs, and a percentage is still within the linear range of the plasmonic dip.[32] In addition to this, aluminum has a greater linear working range due to the length of the plasmonic dip allowing for a wider range of refractive index changes to be detected. This can be seen through the reflectance spectra and the increased slope of the aluminum response (Fig 5)

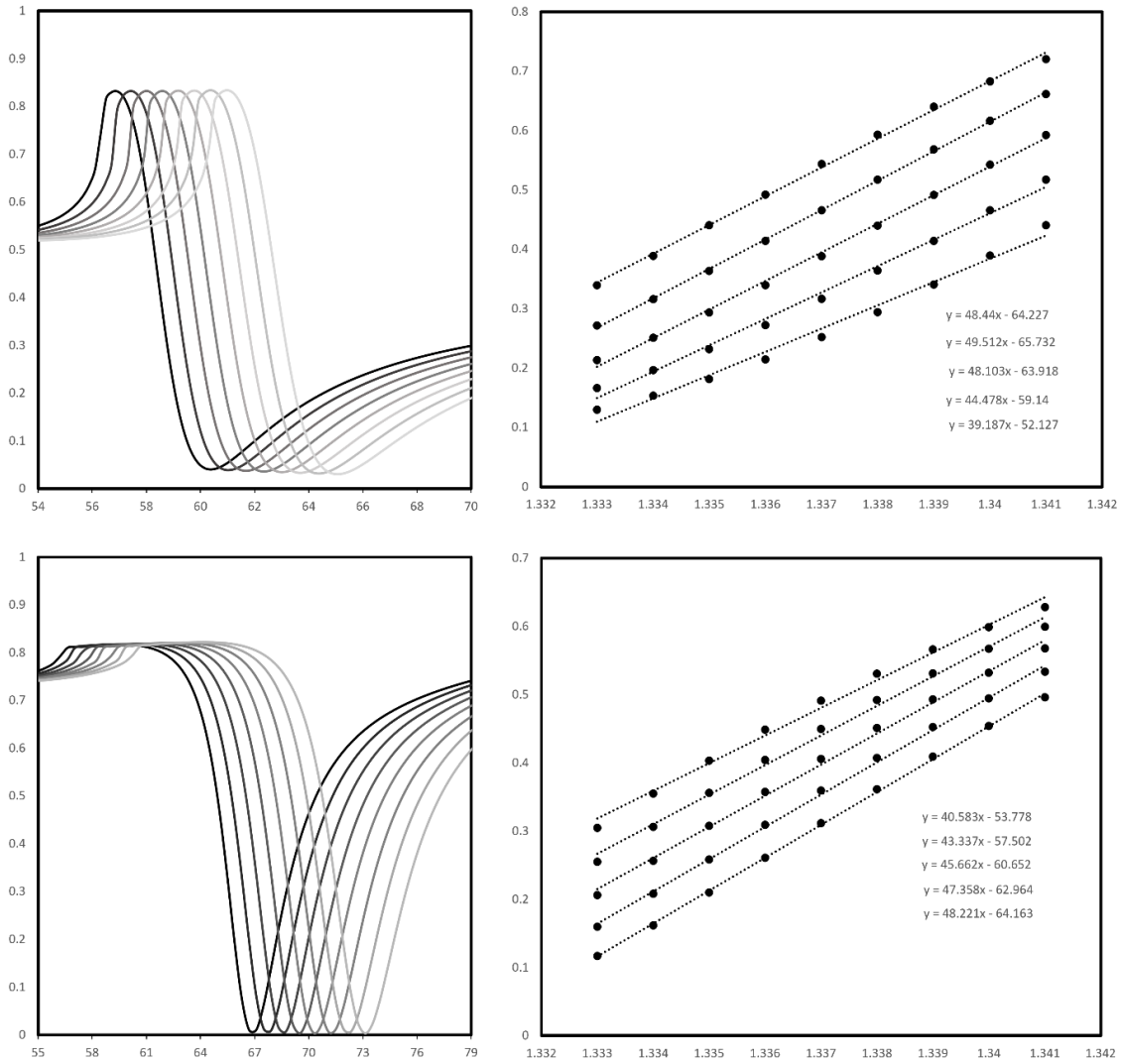


**Figure 3.5** Comparison between gold and aluminum sensitivty to refractive index changes using a fixed angle methodology, and the dependance of fixed angle sensing on the starting angle.

Further SPR analysis was performed experimentally comparing gold and aluminum surfaces. NaCl solutions were used to determine the refractive index sensitivity of the aluminum substrate, which provided a linear response to refractive index changes. Similar to the simulated results, gold has a greater sensitivity to refractive index changes than

aluminum with regards to the minima tracking approach. This is accentuated by the software tracking the minima, as the broader aluminum dip provided to be more difficult to follow. Therefore, the fixed angle methodology was used. With this method, aluminum shows both a higher sensitivity (70041 IU/RIU, 13.9% higher than Au) and a much longer linear range (~0.028 vs ~0.013 RIU) than gold. The sensitivity trends between the fixed angle and the minima tracking data is as predicted based upon the simulations a result of the spectral signal of the plasmonic response.

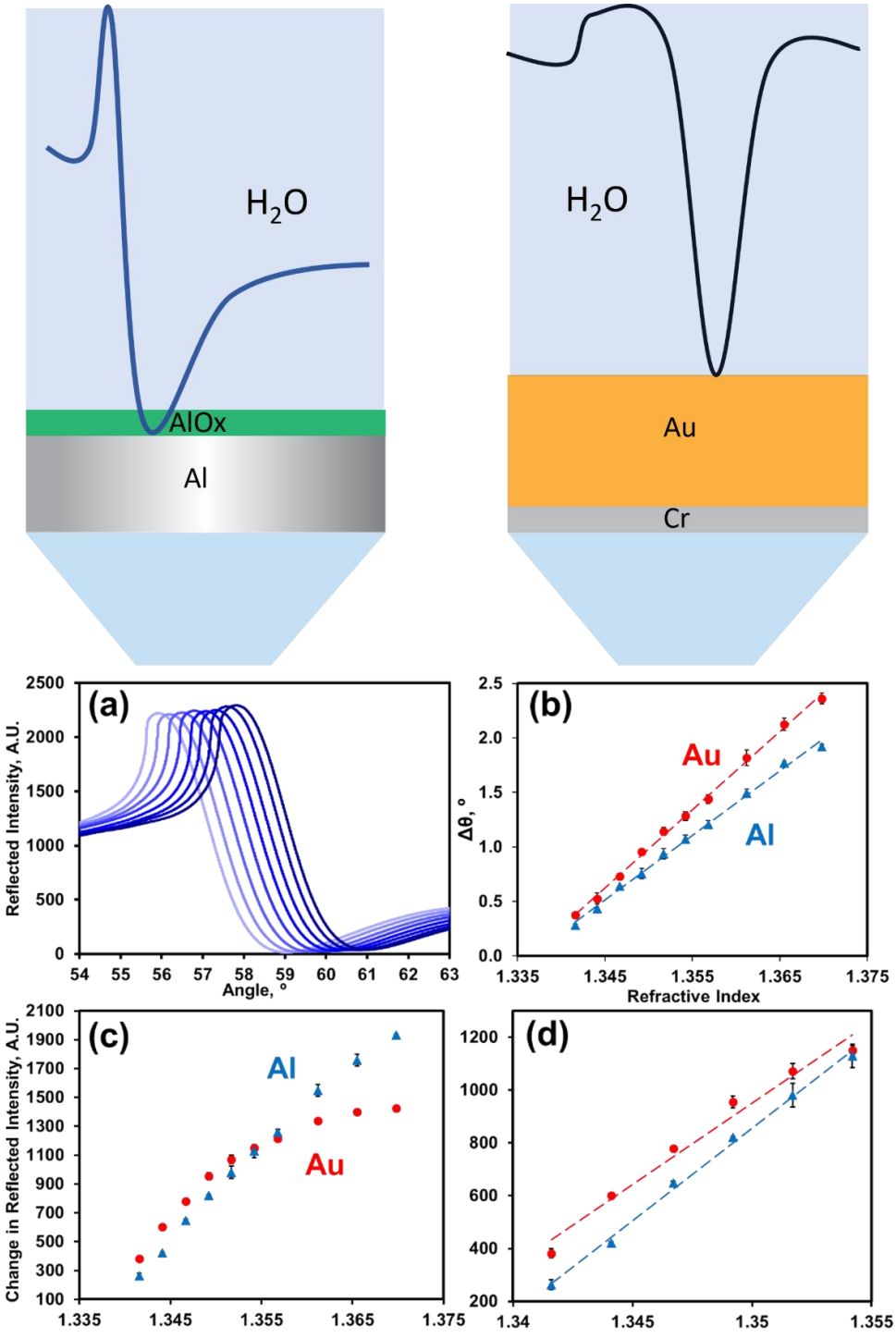


**Figure 3.6.** Experimental results comparing aluminum and gold response to bulk refractive index changes, using both minima tracking and fixed angle methods.

## 3.4 Conclusion

In this work we have demonstrated the necessary steps to produce aluminum substrates for SPR sensors. They demonstrate superior sensitivty to traditional SPR sensors using gold plasmonic substrates. FDTD and Fresnel simulations allow for specific predictions on the differences between aluminum and gold plasmonic responses as well as the benefits of aluminum as a plasmonic sensor. The simulations simplify the fabrication procedures and allow for an optimal selection of thin film thickness for specified instrumentation. The aluminum oxide surface also opens new avenues of surface binding chemistries and has a broad array of established functionalization pathways. This includes, silanization, carboxylation and phosphonylation which are comparable to the thiol binding methods frequently used in gold systems.[33-35] This work demonstrates the possibility of aluminum as an SPR substrate and the advantages of this metal comapred to the commonly used gold.

**3.5** References:


1. Jirı´ Homola , S.S.Y., Gunter Gauglitz *Surface plasmon resonance sensors: review.* Sensors and Actuators B: Chemical, 1999. **54**

2. Homola, J.ı., *Surface Plasmon Resonance Sensors for Detection of Chemical and Biological Species.* Chem. Rev., 2008. **108**: p. 462−493.

3. Mark W. Knight, N.S.K., Lifei Liu, Henry O. Everitt, Peter Nordlander, Naomi J. Halas, *Aluminum for Plasmonics.* ACS Nano, 2013. **8**: p. 834–840.

4. Zhou, M., M. Tian, and C. Li, *Copper-Based Nanomaterials for Cancer Imaging and Therapy.* Bioconjug Chem, 2016. **27**(5): p. 1188-99.

5. Sadeghi, S.M.H., A.; Nejat, A.; Campbell, Q.; Meunier, M *Plasmonic emission enhancement of colloidal quantum dots in the presence of bimetallic nanoparticles.* J. Appl. Phys, 2014. **115**.

6. Gerard, D.G., S. K., *Aluminium plasmonics.* J. Phys. D-Appl, 2015. **48**.

7. Rakic´, A.D., *Algorithm for the determination of intrinsic optical constants of metal films: application to aluminum.* APPLIED OPTICS 1995. **22**.

8. Rodriguez, R.D., et al., *Aluminum and copper nanostructures for surface-enhanced Raman spectroscopy: A one-to-one comparison to silver and gold.* Sensors and Actuators B: Chemical, 2018. **262**: p. 922-927.

9. Arora, P.A., H. V, *Aluminum-Based Engineered Plasmonic Nanostructures for the Enhanced Refractive Index and Thickness Sensing in Ultraviolet-Visible-NearInfrared Spectral Range.* Prog. Electromagn. Res. M, 2019. **79**: p. 167-174. .

10. Liu, J.J.Y., L.; Zhang, H.; Wang, J. F.; Huang, Z., , *Ultraviolet-Visible Chiroptical Activity of Aluminum Nanostructures.* F. Small 2017. **13**.

11. Zhu, Y., et al., *Topologically Enclosed Aluminum Voids as Plasmonic Nanostructures.* ACS Nano, 2017. **11**(11): p. 11383-11392.

12. Yang, K.-Y., et al., *Enhancement Mechanisms of the Second Harmonic Generation from Double Resonant Aluminum Nanostructures.* ACS Photonics, 2017. **4**(6): p. 1522-1530.

13. Lee, K.-L., M.-L. You, and P.-K. Wei, *Aluminum Nanostructures for Surface-Plasmon-Resonance-Based Sensing Applications.* ACS Applied Nano Materials,

2019. **2**(4): p. 1930-1939.

14. Su, M.N., et al., *Ultrafast Electron Dynamics in Single Aluminum Nanostructures.* Nano Lett, 2019. **19**(5): p. 3091-3097.

15. Hobbs, R.G., et al., *High-Energy Surface and Volume Plasmons in Nanopatterned Sub-10 nm Aluminum Nanostructures.* Nano Lett, 2016. **16**(7): p. 4149-57.

16. Aitekenov, S., et al., *SERS for Detection of Proteinuria: A Comparison of Gold, Silver, Al Tape, and Silicon Substrates for Identification of Elevated Protein Concentration in Urine.* Sensors (Basel), 2023. **23**(3).

17. Mogensen, K.B., et al., *Surface-enhanced Raman scattering on aluminum using near infrared and visible excitation.* Chem Commun (Camb), 2014. **50**(28): p. 3744-6.

18. Tanabe, I., et al., *Aluminum Film Thickness Dependence of Surface Plasmon Resonance in the Far- and Deep-ultraviolet Regions.* Chemistry Letters, 2017. **46**(10): p. 1560-1563.

19. Tanabe, I., et al., *Far- and deep-ultraviolet surface plasmon resonance sensors working in aqueous solutions using aluminum thin films.* Sci Rep, 2017. **7**(1): p. 5934.

20. Oliveira, L.C., et al., *Surface Plasmon Resonance Sensing Characteristics of Thin Aluminum Films in Aqueous Solution.* IEEE Sensors Journal, 2017. **17**(19): p. 6258-6267.

21. Li, H., et al., *Highly sensitive detection of proteins based on metal-enhanced fluorescence with novel silver nanostructures.* Anal Chem, 2012. **84**(20): p. 8656-62.

22. Dodge., I.H.M.a.M.J., *Refractive Index and Birefringence of Synthetic Sapphire.* J Opt Soc Am, 1972.

23. Hagemann, H.J.G., W.; Kunz, C, *Optical constants from the far infrared to the x-ray region: Mg, Al, Cu, Ag, Au, Bi, C, and Al2O3.* J. Opt. Soc. Am., 1975.

24. Tanabe, I., et al., *Direct optical measurements of far- and deep-ultraviolet surface plasmon resonance with different refractive indices.* Opt Express, 2016. **24**(19): p. 21886-96.

25. Treebupachatsakul, T., S. Shinnakerdchoke, and S. Pechprasarn, *Analysis of Effects of Surface Roughness on Sensing Performance of Surface Plasmon*

*Resonance Detection for Refractive Index Sensing Application.* Sensors (Basel), 2021. **21**(18).

26. YEE, K.S., *Numerical Solution of Initial Boundary Value Problems Involving Maxwell's Equations in Isotropic Media.* IEEE TRhTSACTIONS ON AXTEXXAS AND PROPAGATION, 1966. **14**(3).

27. Abbott, W.M., et al., *Comparison of Metal Adhesion Layers for Au Films in Thermoplasmonic Applications.* ACS Appl Mater Interfaces, 2020. **12**(11): p. 13503-13509.

28. Benjamin, P., C. Weaver, and N.F. Mott, *The adhesion of evaporated metal films on glass.* 1961. **261**(1307): p. 516-531.

29. Gryczynski, I., et al., *Surface Plasmon-Coupled Emission with Gold Films.* J Phys Chem B, 2004. **108**(33): p. 12568-12574.

30. Puiu, M. and C. Bala, *SPR and SPR Imaging: Recent Trends in Developing Nanodevices for Detection and Real-Time Monitoring of Biomolecular Events.* Sensors (Basel), 2016. **16**(6).

31. Lobry, M., et al., *HER2 biosensing through SPR-envelope tracking in plasmonic optical fiber gratings.* Biomed Opt Express, 2020. **11**(9): p. 4862-4871.

32. Hinman, S.S., et al., *On-Demand Formation of Supported Lipid Membrane Arrays by Trehalose-Assisted Vesicle Delivery for SPR Imaging.* ACS Appl Mater Interfaces, 2015. **7**(31): p. 17122-30.

33. Simunin, M.M., et al., *Features of Functionalization of the Surface of Alumina Nanofibers by Hydrolysis of Organosilanes on Surface Hydroxyl Groups.* Polymers (Basel), 2021. **13**(24).

34. Alexander, S., V. Gomez, and A.R. Barron, *Carboxylation and Decarboxylation of Aluminum Oxide Nanoparticles Using Bifunctional Carboxylic Acids and Octylamine.* Journal of Nanomaterials, 2016. **2016**: p. 1-8.

35. Kun Qian, J.W., Fang Liu, Hubert H. Girault, Baohong Liu, and Chengzhong Yu, *A Phospho-Directed Macroporous Alumina¿Silica Nanoreactor with Multi-Functions.* Acs Nano, 2009. **3**.

## Chapter 4: Detection of anti-Myelin Associated Glycoprotein using Aluminum-Based SPR Imaging

### 4.1 Introduction

Anti-MAG demyelinating neuropathy is an auto-immune disorder that affects the peripheral nervous system leading to tingling and numbness in the patient's extremities. It differs from other similar chronic inflammatory demyelinating polyradiculoneuropathies (CIDP) in that the disease is not inflammatory and treatment must therefore differ.[1] This leads to diagnosis of anti-MAG neuropathy to be important to properly treat the disease. However, solely symptom-based diagnosis is not sufficient as CIDP-like diseases have similar symptoms.[2] Therefore, biomarker-based diagnosis techniques of anti-MAG are used to differentiate anti-MAG neuropathy from other CIDP-like diseases.[3]

MAG contains 5 extracellular immunoglobulin-like domains, a singular transmembrane domain, and two cytoplasmic domains. MAG is also highly conserved among vertebrates with 95% of the extracellular domains being conserved between mouse and human.[4] The production of MAG is limited to oligodendrocytes in the central nervous system (CNS) and Schwann cells in the peripheral nervous system (PNS). Compounding upon this, the abundance of MAG is relatively low in the cells that produce it, comprising 1% of myelin protein in the CNS and 0.1% in the PNS.[5] MAG promotes stability between the neuronal axon and myelin sheath. In a MAG-null mouse model, myelin was abundant but so was the degree of unmyelinated axons. In addition to supporting the interactions between axon and myelin sheath, MAG also inhibits axon growth. [6]

There are two main binding partners for MAG that facilitate both its myelin support and axon growth suppression, sialoglycans and Nogo receptors.[7, 8] The sialoglycan binding of MAG was predicted due to the similarities in structure between the IG like domains of MAG and the family of sialic acid binding proteins known as Siglecs.[9] Recombinant MAG has further been demonstrated to bind to cell surface sialoglycans, with a preference towards two specific gangliosides, GD1a and GT1b.[10] When compared to the other common gangliosides, GM1 and GD1b which lack MAG binding it was predicted that a GalNAc-Galactose-NeuAc is the required moiety for MAG binding.[11] Due to prevalence of both GD1a and GT1b in the brain, it is thought that the ganglioside binding is the main mediator of axon-myelin stabilization. The Nogo receptor was found to be a common moiety between a variety of axon regenerative inhibitors and this binding is predicted to control that aspect of MAG.[12] The direct effect of MAG activity loss has been demonstrated in a variety of animal studies. In a mouse model, the synthesis of gangliosides with the necessary binding moiety was limited through knockout of the *B4galnt1* gene.[13] This induces axon degeneration in aging mice with a similar phenotype, between MAG knockouts and double gene knockouts.[14] In mouse models with differing ganglioside synthesis deficiencies the same phenotype was not seen as the MAG binding moiety was maintained.[15]

Current techniques to detect anti-MAG neuropathy rely upon fluorescent based detection through ELISA.[16] In this way, the relative amount of anti-MAG IgG can be determined through comparison to the overall antibody count of a patient. The anti-MAG is detected through immobilization of MAG and subsequent fluorescence from the

secondary antibody. Cross reactivity amongst antibodies is further controlled through the usage of immobilized ganglioside. The binding region of anti-MAG to MAG is at a carbohydrate moiety, specifically an HNK-1 modification, and therefore gangliosides are used as controls.[17] The Buhlmann titer is the testing methodology used to perform these ELISA measurements and uses Buhlmann titer units, with 1000 Buhlmann titer units being considered a positive case of anti-MAG neuropathy. However, the validity of this technique around the value of 1000 Bulhmann titer units has been found to detect false positives.[18] Alternative methods have been developed that focus on other antibodies such as anti-HNK1.[19] These still rely upon ELISA to detect and do not give quantitative information on the concentration of antibody in the sample. In addition to this they are more prone to off target effects due to the nature of ELISA sensing.[20-22]

Surface plasmon resonance (SPR) is a label-free technique that allows for direct detection of analytes by detecting refractive index changes at a surface.[23] Quantitative determinations of analyte can be found based upon changes in SPR response. SPR imaging is used as a high throughput multiplex detection method, and has been used for drug discovery, disease detection, protein kinetics, and cell profiling.[24-27] Arrays can also be made on SPRi that allow for controls and account for the non-specific binding and cross reactivity present even in monoclonal antibodies. While gold has traditionally been used for SPR sensors, alternative metals such as aluminum have recently gained popularity, due to increased sensitivity, and inherent antifouling properties.[28]

In this work we report a sensor array capable of quantitative detection of anti-MAG antibodies in biological media using an aluminum SPRi array. The array was built using a

silicated aluminum substrate modified with PFDTS wherein lipids can self-insert while providing a near super hydrophobic surface that has been demonstrated to have antifouling properties. On this array, GM1 ganglioside is used to account for cross-reactivity of the anti-MAG antibody, while a DGS-NTA lipid is used to bind a His-tagged MAG. This is then tested in both buffer, to confirm the efficacy of the technique, and subsequently in an artificial urine media to determine the stability of the system in biological systems. This system can then be further expanded to include antibodies with co-morbidity with anti-MAG such as anti-HNK1.

### 4.2 Materials and Reagents

*H,1H,2H,2H*-Perfluorodecyltrichlorosilane (PFDTS) was obtained from Fisher Scientific (Pittsburgh, PA). Monoganglioside $GM_1$ was obtained from Matreya (Pleasant Gap, PA). Myeline associated glycoprotein (MAG) was purchased from Sino Bioligical (Wayne, PA). Anti-Myelin associated glycoprotein was purchased from Biolegend (San Diego, CA).

### Artificial Urine Preparation

Artificial urine matrix for biosensing experiments was prepared according to a previously published protocol.[29] Component chemicals were added as solids at the concentrations provided to ultrapure DI H2O held at 38 ° C under constant stirring. Anti-MAG was spiked into the artificial urine to replicate biological conditions.

### Fabrication and Modification of SPR chips

Microarray substrates used for SPR imaging were fabricated along previously reported procedures. [30] In brief, piranha-cleaned glass slides were spincoated at 4000 RPM for 45 s with hexamethyldisilazane (HMDS) and AZ5214E in succession, followed by a 1 min bake at 110 ° C. Photopatterning via UV exposure was conducted with a photomask and Karl-Suss MA-6 system followed by AZ400K development using standard protocols. 150 nm Al was deposited by EBPVD, followed by removal of wells with acetone. An additional deposition of 18 nm Al was lastly added to generate the plasmonically active layer in the wells. The final array was a 10 × 12 set of 600 μm diameter circular wells. Silica was deposited by plasma enhanced chemical vapor deposition using a Unaxis Plasmatherm 790 system (Santa Clara, CA). For both conventional and imaging substrates, chips were stored under vacuum until experimental use. Perfluorination was performed wherein the chips were submerged in 1 mM PFDTS in toluene and incubated for 30 minutes. Chips were subsequently cleaned with toluene, ethanol and ultrapure water and dried with nitrogen. 1.5 μL of either 100 μg/mL DGS-NTA or GM1 ganglioside solutions in chloroform were pipetted into specific rows on the chip, to allow for multiplexed information when attached to the flow system. The final chip contains a control row with bare PFDTS, a DGS-NTA row for MAG his-tag binding, and a GM1 row for specific control.

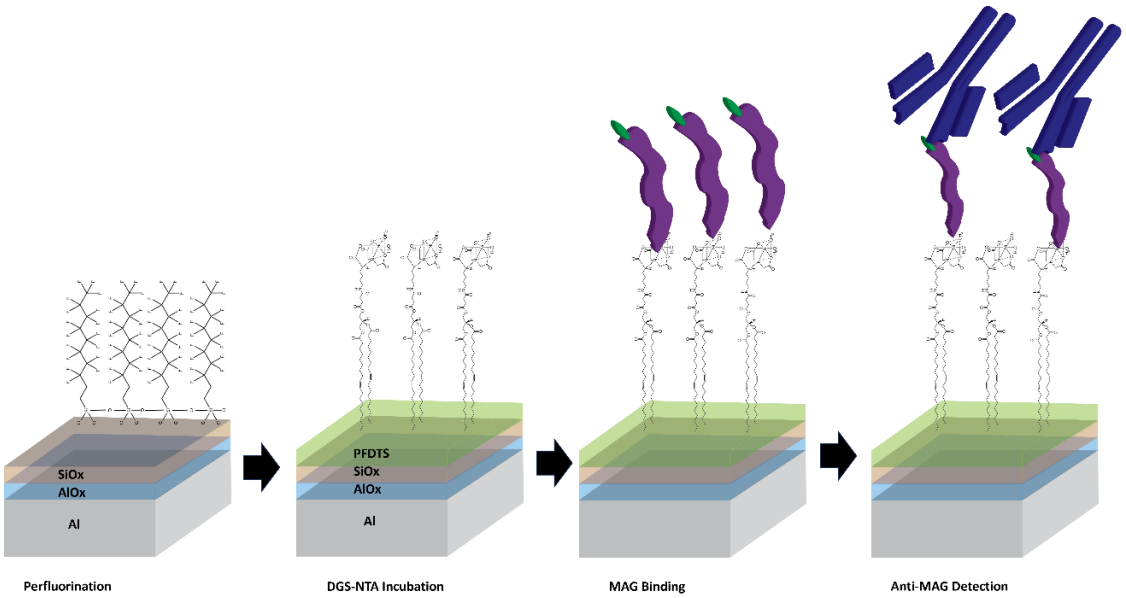


Figure **4.1**. Surface functionalization scheme, and detection steps.

**Surface Characterization**

AFM was performed with an AIST-AFM. 300 kHz cantilever tips were used for AFM measurements with a 1.5 $\mu m^2$ scan size. Contact angle measurements were imaged with 12-bit CCD camera.

**SPR imaging analysis**

For SPR imaging, measurements were conducted on a home-built experimental setup, a detailed description of which was reported previously. [31] Briefly, aluminum substrate microarrays were mounted onto an SF2 glass 25 mm equilateral triangular prism (n = 1.648) with a layer of high-refractive index matching fluid to facilitate even contact.

A 3D printed optical stage and flow-cell holder allowed mounting of a 300 μL S-shaped flowcell that covered four rows of wells. The optical stage was fixed atop a goniometer that could be manually rotated to tune the incident angle of incoming light from an incoherent light emitting diode (LED) source ($\lambda$ = 648 nm) that could be either p- or s-polarized by a rotatable polarizer. Reflected images from the array were captured with a cooled 12-bit CCD camera (QImaging Retiga 1300) with a resolution of 1.3 MP (1280 × 1024 pixels) and 6.7 μm × 6.7 μm pixel size. Online experimental data acquisition consisted of recording the p-polarized reflected intensity of each well (regions of interest manually selected) every 300 ms during baselining, injection and incubation of analyte solutions, and rinse cycles, followed by an acquisition of the s-polarized intensity. Intensity data was normalized in two ways. First, the p-polarized intensity was divided by the intensity of s-polarized intensity then multiplied by 100 to generate a percentage value.

### 4.3 Results and Discussion

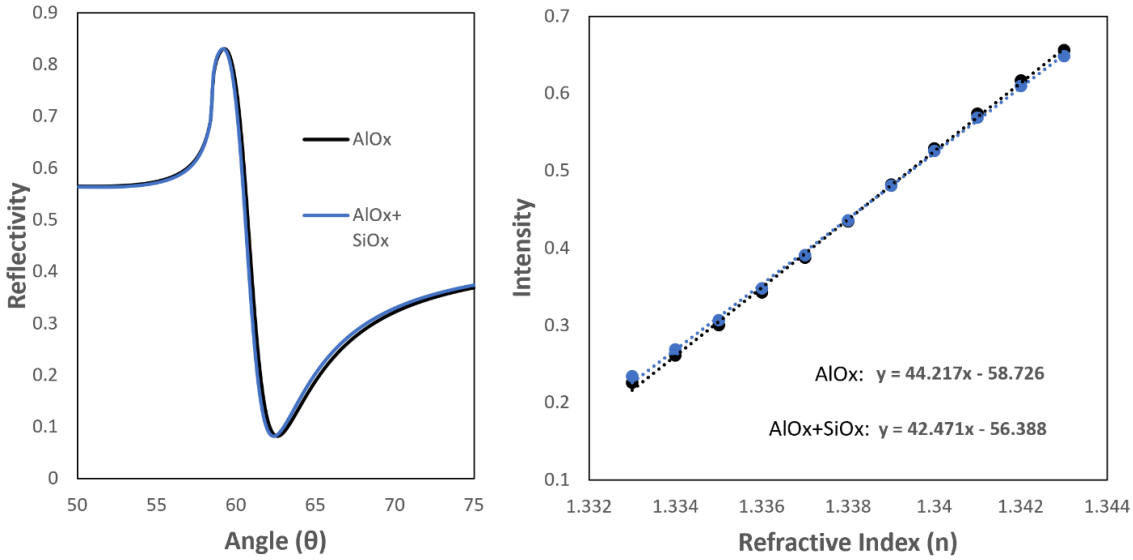


**Figure 2.** Fresnel simulation comparing the effects of SiOx layer on the plasmonic response compared to the native AlOx. Theoretical calibration curve demonstrating any changes to refractive index sensitivity.

Initial surface characteristics were predicted using Fresnel equations to determine the effect of SiOx on the aluminum SPR substrate. The plasmonic dip remained relatively unchanged with the addition of the 3 nm of SiOx, and to further assert this the refractive index sensitivity was examined. The addition of SiOx reduced the sensitivity of the surface by ~4%, and does not significantly impact the overall sensitivity of the sensor. The sensitivity was measured using a fixed angle methodology to properly mimic the SPRi instrument. The surface was further characterized experimentally.

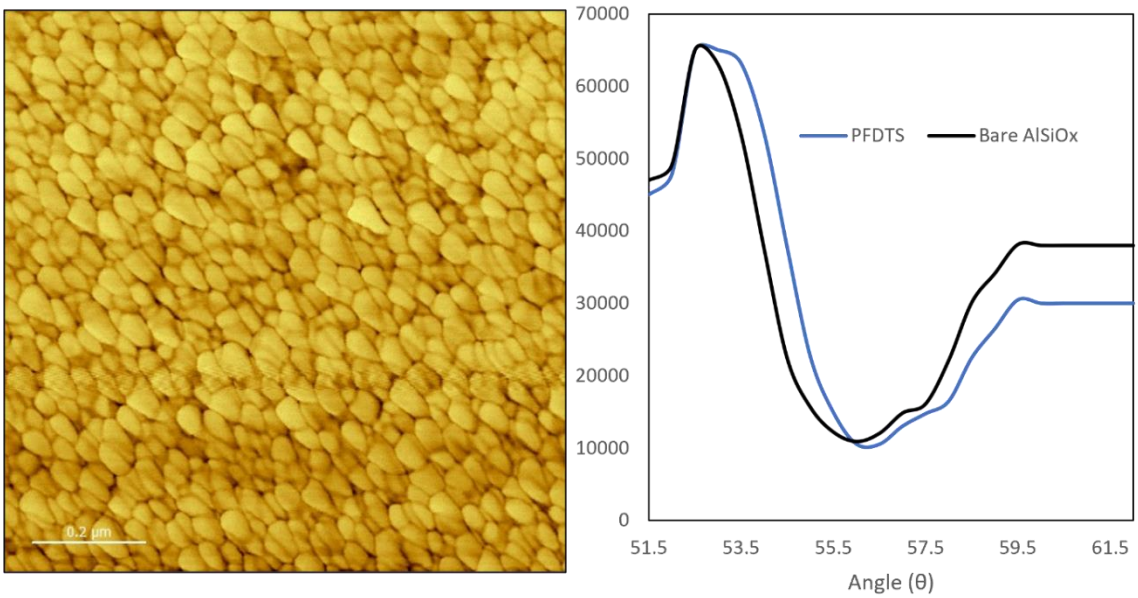


**Figure 3.** AFM of the SiOx surface on an aluminum thin film. SPRi plasmonic curve pre and post functionalization.

AFM of the AlSiOx substrate was performed to analyze the surface roughness. The surface was found to have a root mean roughness (RMS) of 3 nm. This is slightly greater than what is found with bare AlOx but is still well within an optimal range for SPR sensing. The plasmonic response of the bare AlSiOx surface was compared to the perfluorinated surface to elucidate the effects of the increased dielectric layer thickness on the plasmonic response. An expected shift occurs, with minor broadening in the plasmonic dip due to increases in surface roughness.


**Figure 4.** Water droplet contact angle comparisons to confirm the hydrophobicity of the surface.

The silicated surface is further functionalized with PFDTS to increase hydrophobicity (Figure 4) which is an established technique that does not significantly increase the surface roughness. As the perfluorinated surface is further functionalized with either DGS-NTA or GM1, the continuation of the hydrophobicity must be confirmed. The effects of the DGS-NTA are of note as ganglioside induced changes on surface hydrophobicity have been previously studied. The change in contact angle is ~8$^{o}$ which is comparable to the change caused by GM1 maintaining the hydrophobicity required for antifouling properties. The surface can then be further applied towards biological sensing applications.

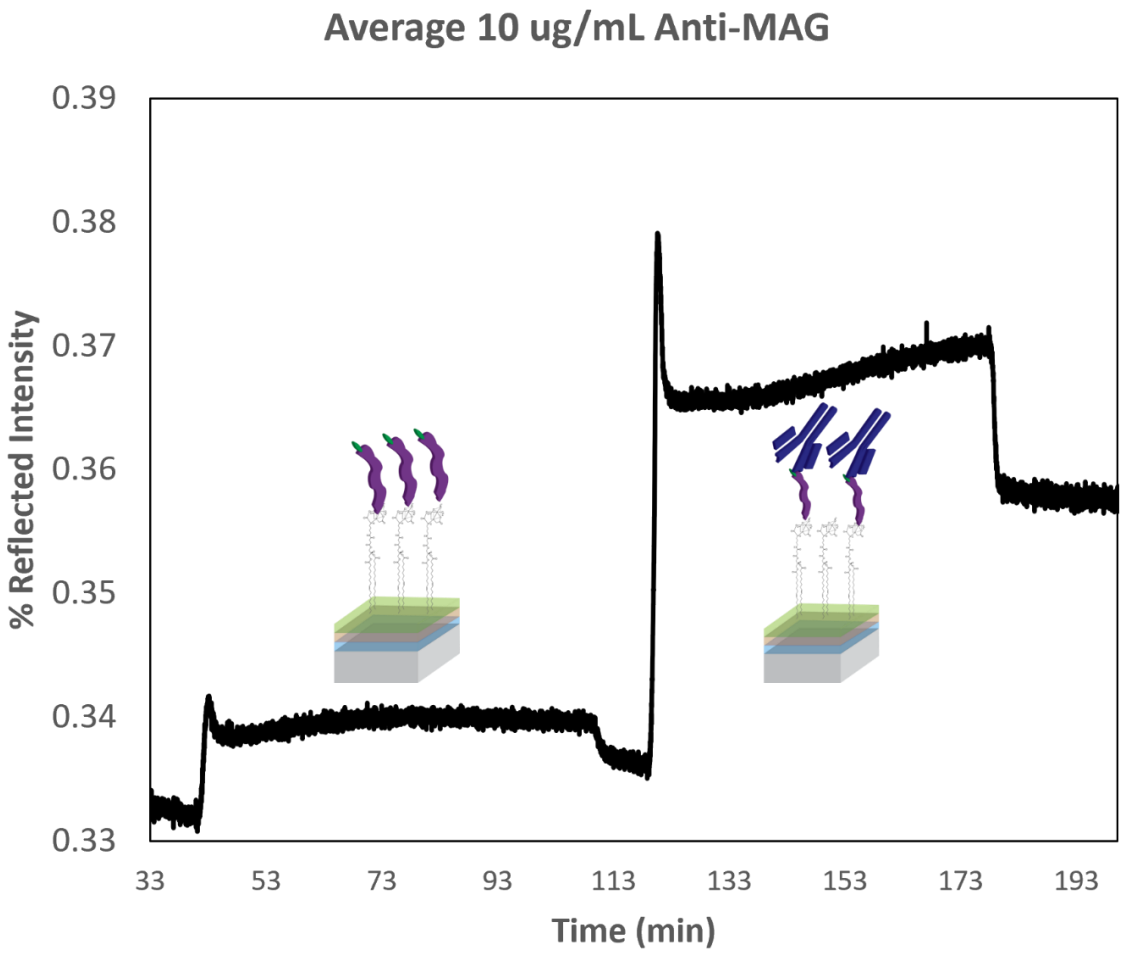


**Figure 5.** Sensogram depicting the binding of MAG to the DGS-NTA surface, and subsequent binding of anti-MAG.

His-tagged MAG, flowed over the surface and bound to the NTA of the DGS-NTA surface. GM1 was used as a control surface due to an established cross-reactivity of the anti-MAG to gangliosides. The cross reactivity is due to the glycan modification of the MAG protein which has been demonstrated to be the antigenic site of the anti-MAG. The His tag of the MAG was positioned to be opposite of the antigenic site, to reduce any

interference caused by binding the protein to the surface. Anti-MAG is injected and binds to the MAG bound. This signal is compared to an unfunctionalized channel, and a GM1 channel to confirm the specific interaction between the anti-MAG and MAG binding. As the analyte of interest, anti-MAG was sequentially diluted (10 µg/mL-0.1µg/mL), and the resulting signal measured to form a calibration curve. (Fig 3) Non-specific binding is prevented due to the antifouling hydrophobic layer provided by the perfluorinated surface.

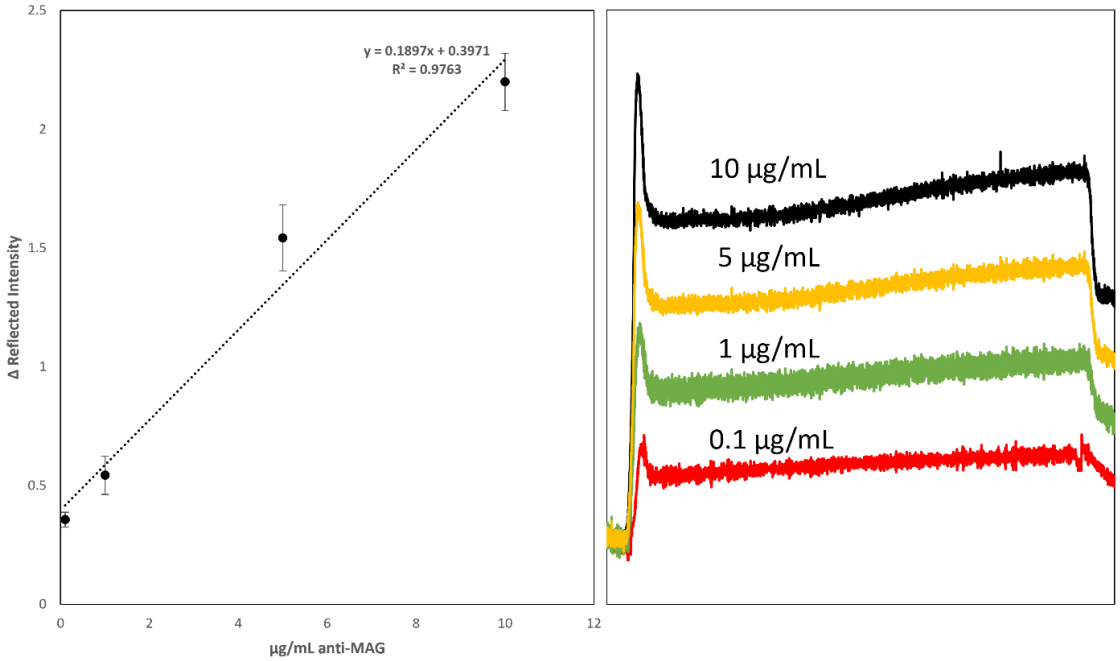


**Figure 4.6.** Calibration curve of anti-MAG SPRi response, and sensograms of the anti-MAG binding

In addition, relatively little binding was found between the GM1 surface and anti-MAG. At the lowest concentration of 0.1 µg/mL anti-MAG induced a reflectivity shift of 0.356% RIU. Notably when compared to other glycogenic antibody binding assays on

SPRi the sensitivity is lower. [32]The lowered sensitivity is likely due to a multitude of factors, the distance induced by the length of the MAG being one. In addition to this MAG can form dimers in solution at the antigenic site, with approximately 20% of MAG forming this native dimer in solution. [33] The dimer would block access to the glycan modification on the MAG, and therefore prevent antibody access. Despite this, the sensor can detect anti-MAG quantitatively whereas the majority of anti-MAG sensors do not detect it directly, instead relying upon a secondary antibody and subsequent ELISA. To further demonstrate the effectiveness of the sensor for biologic applications, a complex media was chosen and tested.

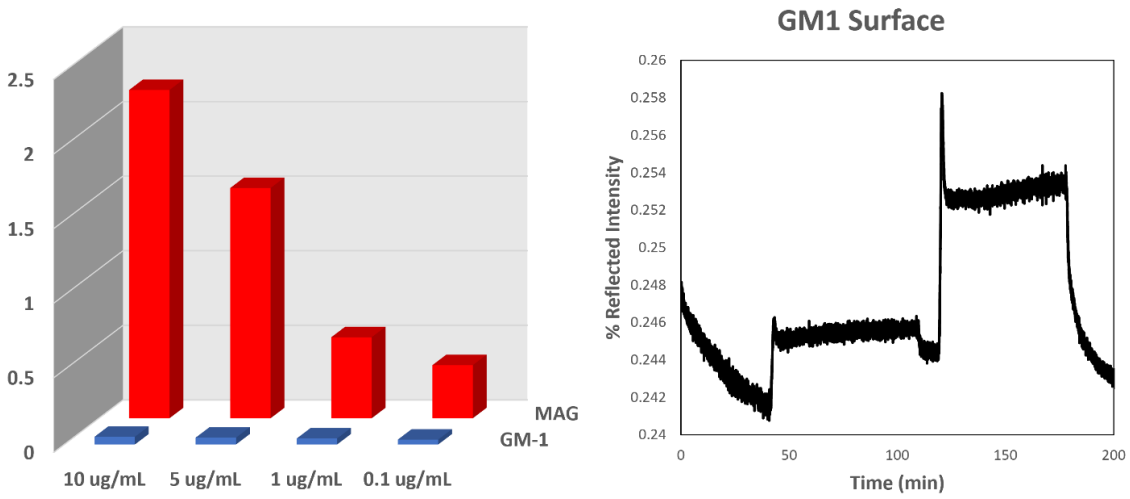


**Figure 4.7.** Comparison of anti-Mag binding to GM1 and MAG and spiked urine sensogram

Urine was the media of choice due to a clinical ease of access and has a found recent promise in the detection of autoimmune disease biomarkers.[34] The procedure that was implemented for the PBS solutions was repeated with urine analysis. The anti-MAG was instead diluted in artificial urine, to replicate a patient sample. As expected, a minor loss in analyte signal was detected, due to interference induced by the urine. However, a significant portion of the non-specific interactions of the biological matrix are blocked due to the perfluorinated hydrophobic surface. In addition, the urine did not induce any significant signal to the GM1 surface.

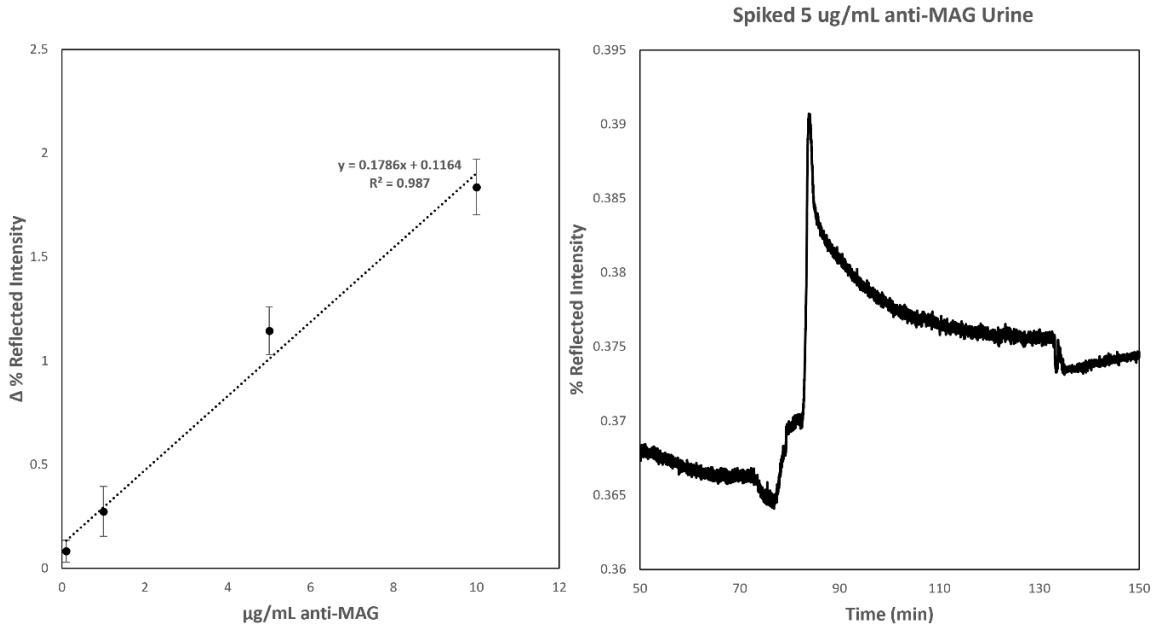


**Figure 4.8.** Calibration curve of anti-MAG SPRi response in artificial urine, and urine sensogram.

### 4.4 Conclusion:

In this work we have fabricated a high-throughput label-free quantitative sensor for anti-MAG. The ability to detect anti-MAG is a powerful tool in the diagnosis and study of MAG neuropathy due to the similar symptomology of MAG neuropathy but differing treatment methods compared to other neuropathy pathologies. The quantitative nature of SPR for anti-MAG is particularly important due to the prevalence of semi-quantitative Buhlmann titers. While Buhlmann titers have found usage as diagnosis tools, further studying would benefit from the quantitative sensor discussed. Further work with the Al SPRi anti-MAG sensing platform could improve the study of anti-MAG neuropathy further. First, studies performed in whole serum would be beneficial as they would allow

comparison to detection schemes of other auto-immune antibodies. The comparison of autoimmune antibodies is a vital field of interest due to the correlation between the specific antibodies and symptoms and therefore treatment options. Development of a multiplexed sensor with a variety of antigens such as MAG, GM1, GT1B and other gangliosides can then be applied to further the understanding interactions between autoimmune neurological diseases.

## 4.5 References


1. Gogia B, R.C.F., Khan Suheb MZ, et al., *Chronic Inflammatory Demyelinating Polyradiculoneuropathy.* StatPearls [Internet]. 2023, Treasure Island (FL): StatPearls Publishing.

2. Allen, J.A., *The Misdiagnosis of CIDP: A Review.* Neurol Ther, 2020. **9**(1): p. 43-54.

3. Pascual-Goni, E., et al., *Clinical and laboratory features of anti-MAG neuropathy without monoclonal gammopathy.* Sci Rep, 2019. **9**(1): p. 6155.

4. MONIQUE ARQUINT, J.R., LOO-SAR CHIA, JIM DOWN, DAVE WILKINSON, HAGAN BAYLEY, PETER BRAUN, ROBERT DUNN, *Molecular cloning and primary structure of myelin-associated glycoprotein.* Neurobiology, 1987. **84**: p. 600-604.

5. Bartsch, U., F. Kirchhoff, and M. Schachner, *Immunohistological localization of the adhesion molecules L1, N-CAM, and MAG in the developing and adult optic nerve of mice.* 1989. **284**(3): p. 451-462.

6. Schachner, M. and U. Bartsch, *Multiple functions of the myelin-associated glycoprotein MAG (siglec-4a) in formation and maintenance of myelin.* 2000. **29**(2): p. 154-165.

7. Yang LJ, Z.C., Shaper NL, Kiso M, Hasegawa A, Shapiro RE, Schnaar RL. , *Gangliosides are neuronal ligands for myelin-associated glycoprotein.* . Proc Natl Acad Sci U S A, 1996. **93**.

8. Aaron W. McGee, S.M.S., *The Nogo-66 receptor: focusing myelin inhibition of axon regeneration.* Trends in Neurosciences, 2003. **26**(4): p. 193-198.

9. Varki, A. and T. Angata, *Siglecs—the major subfamily of I-type lectins.* Glycobiology, 2005. **16**(1): p. 1R-27R.

10. Kelm, S., et al., *Sialoadhesin, myelin-associated glycoprotein and CD22 define a new family of sialic acid-dependent adhesion molecules of the immunoglobulin superfamily.* Curr Biol, 1994. **4**(11): p. 965-72.

11. Collins, B.E., et al., *Binding specificities of the sialoadhesin family of I-type lectins. Sialic acid linkage and substructure requirements for binding of myelin-associated glycoprotein, Schwann cell myelin protein, and sialoadhesin.* J Biol Chem, 1997. **272**(27): p. 16889-95.

12. Mehta, N.R., et al., *Myelin-associated glycoprotein (MAG) protects neurons from acute toxicity using a ganglioside-dependent mechanism.* ACS Chem Neurosci, 2010. **1**(3): p. 215-222.

13. Takamiya, K., et al., *Mice with disrupted GM2/GD2 synthase gene lack complex gangliosides but exhibit only subtle defects in their nervous system.* Proc Natl Acad Sci U S A, 1996. **93**(20): p. 10662-7.

14. Pan, B., et al., *Myelin-associated glycoprotein and complementary axonal ligands, gangliosides, mediate axon stability in the CNS and PNS: neuropathology and behavioral deficits in single- and double-null mice.* Exp Neurol, 2005. **195**(1): p. 208-17.

15. Yamashita, T., et al., *Enhanced insulin sensitivity in mice lacking ganglioside GM3.* Proc Natl Acad Sci U S A, 2003. **100**(6): p. 3445-9.

16. Giuseppe Liberatore, C.G., Blesson Punnen Sajeev, Emanuela Morenghi, Fabrizia Terenghi, Francesca Gallia, Pietro Emiliano Doneddu, Fiore Manganelli, Dario Cocito, Massimiliano Filosto, Giovanni Antonini, Giuseppe Cosentino, Girolama Alessandra Marfia, Angelo Maurizio Clerici, Giuseppe Lauria, Tiziana Rosso, Guido Cavaletti, Eduardo Nobile-Orazio, *Sensitivity and specificity of a commercial ELISA test for anti-MAG antibodies in patients with neuropathy.* Journal of Neuroimmunology, June 08, 2020. **Volume 345**.

17. Herrendorff, R., et al., *Selective in vivo removal of pathogenic anti-MAG autoantibodies, an antigen-specific treatment option for anti-MAG neuropathy.* Proc Natl Acad Sci U S A, 2017. **114**(18): p. E3689-E3698.

18. Steck, A.J., *Anti-MAG neuropathy: From biology to clinical management.* J Neuroimmunol, 2021. **361**: p. 577725.

19. Delmont, E., et al., *Relevance of anti-HNK1 antibodies in the management of anti-MAG neuropathies.* J Neurol, 2019. **266**(8): p. 1973-1979.

20. Terato, K., et al., *Preventing intense false positive and negative reactions attributed to the principle of ELISA to re-investigate antibody studies in autoimmune diseases.* J Immunol Methods, 2014. **407**: p. 15-25.

21. Frese, K., et al., *An automated immunoassay for early specificity profiling of antibodies.* MAbs, 2013. **5**(2): p. 279-87.

22. Bumbaca, D., et al., *Highly specific off-target binding identified and eliminated during the humanization of an antibody against FGF receptor 4.* MAbs, 2011.

**3**(4): p. 376-86.

23. Chiu, N.F., *The Current Status and Future Promise of SPR Biosensors.* Biosensors (Basel), 2022. **12**(11).

24. Li, S., et al., *Dextran hydrogel coated surface plasmon resonance imaging (SPRi) sensor for sensitive and label-free detection of small molecule drugs.* Applied Surface Science, 2015. **355**: p. 570-576.

25. Huo, Z., et al., *Recent advances in surface plasmon resonance imaging and biological applications.* Talanta, 2023. **255**: p. 124213.

26. Malinick, A.S., et al., *Detection of Multiple Sclerosis Biomarkers in Serum by Ganglioside Microarrays and Surface Plasmon Resonance Imaging.* ACS Sens, 2020. **5**(11): p. 3617-3626.

27. Lauren K. Wolf, D.E.F., and Rosina M. Georgiadis, *Quantitative Angle-Resolved SPR Imaging of DNA-DNA and DNA-Drug Kinetics.* JACS, 2005. **127**: p. 17453-17459.

28. Lambert, A.S., et al., *Plasmonic Biosensing with Aluminum Thin Films under the Kretschmann Configuration.* Anal Chem, 2020. **92**(13): p. 8654-8659.

29. Sarigul, N., F. Korkmaz, and I. Kurultak, *A New Artificial Urine Protocol to Better Imitate Human Urine.* Sci Rep, 2019. **9**(1): p. 20159.

30. Abbas, A., M.J. Linman, and Q. Cheng, *Patterned resonance plasmonic microarrays for high-performance SPR imaging.* Anal Chem, 2011. **83**(8): p. 3147-52.

31. Thomas Wilkop, Z.W., and Quan Cheng, *Analysis of μ-Contact Printed Protein Patterns by SPR Imaging with a LED Light Source.* Langmuir, 2004. **20**: p. 11141-11148.

32. Malinick, A.S., et al., *Surface plasmon resonance imaging (SPRi) in combination with machine learning for microarray analysis of multiple sclerosis biomarkers in whole serum.* Biosensors and Bioelectronics: X, 2022. **10**.

33. Pronker, M.F., et al., *Structural basis of myelin-associated glycoprotein adhesion and signalling.* Nat Commun, 2016. **7**: p. 13584.

34. Morell, M., F. Perez-Cozar, and C. Maranon, *Immune-Related Urine Biomarkers for the Diagnosis of Lupus Nephritis.* Int J Mol Sci, 2021. **22**(13)

# Chapter 5: Development and Applications of a Gold Metamaterial for SPR and SERS Sensing with Unique SERS Specificity

## 5.1 Introduction

Development of biosensors has evolved greatly in recent years due to the inclusion of nanomaterials into the sensor's fabrication processes.[1] Biosensors have found a wide variety of applications in SPR, SERS, electrochemistry and other surface-based techniques.[2-5] Specifically, plasmonic sensors are of particular interest due to their high sensitivity and intrinsically label free measurement. Fabrication of these systems requires precise tools and can be both time consuming and difficult while also requiring facilities that are not widely available. Colloidal methods of synthesizing nanoparticles are simple and well understood while also capable of being performed on a benchtop.[6] In the case of SPR and SERS, plasmonic metamaterials have been explored as unique sensors combining the benefits of both nanoscale plasmonics and the simple thin films.[7, 8] For SERS, maximal enhancement occurs when a nanogap is formed between two nanoparticles.[9] Development of metamaterials that have consistent nanogap formation is required for consistent SERS enhancement. While this is commonly performed using clean room technologies such as photolithography and PVD, colloidal nanoparticle synthesis coupled with controlled polymerization of nanoparticles are a popular alternative.[10-12] To do this, interfacial nanoparticle methods through self-assembly process are enticing.

Commonly synthesized AuNP's are citrate capped and therefore highly hydrophilic. Through introduction of organic solvent, the nanoparticles will form a self-assembled layer at the interface.[13] However, these nanoparticle formations are relatively disordered. Hydrophobic dithiols have been introduced to link the nanoparticles together, increasing the ordered nature of them.[14] The dithiol linker is only present in the organic solvent, while the AuNP's in the aqueous, they will agglomerate at the interface. However, the optimal nanogap is much shorter than the distance provided by these linkers, leading to shorter rigid linkers being beneficial in colloidal interfacial nanoparticle agglomeration.[15]Girault *et al* were the first to use a tetrathiafulvalene, a known semiconducting material as a AuNP linker.[12, 16] This linker provides structural stability due to a ring structure while also containing the dithiol groups that bind to AuNP's. Mixing the organic and aqueous layers causes miniscule amounts of linker to enter the aqueous phase and scavenge AuNP's to the interface, forming what they referred to as a AuMeLD. In doing this a highly ordered nanoparticle array can be formed. The potential of AuMeLD as an optimal substrate for SERS sensing has been explored.[17, 18]

SERS detection has found a variety of uses in biological and chemical sensors [19-21]. Of particular interest is the usage of SERS as an environmental sensor for toxicants.[22] PCB's are commonly used as agricultural pesticides and have been found to be carcinogenic. [23] SERS has been utilized to detect PCB's although there was only a limited literature for a select few. Therefore, exploration of a larger variety of PCB's is beneficial to widen the range of detectable toxicants. [24, 25] PCB's are highly hydrophobic and could

therefore preferentially bind to aromatic hydrophobic surfaces. This functionality has been taken advantage of in the design of the PCB sensors. [26]

In this work we will demonstrate the formation of a gold metamaterial substrate/surface, fabricated with benchtop methods and DBTTF linkers. We will then characterize this surface with AFM, SEM, and spectroscopic techniques, and compare it to other AuNP films. FDTD simulations have been used to determine the hotspot formation in the films. The ability to couple the substrates to Krestchmann configuration in SPR instrument was also explored, and the sensitivity to refractive index changes was tested. Finally, the surface was used as a SERS sensor to detect PCB-126 and was compared to other methods that utilized graphene to attract the PCB to the surface.

**5.2 Methods and Materials:**

Gold nanoparticles were fabricated using the Turkovich method.[27] In brief, 1.004 mM $HAuCl_4$ is refluxed. 1% w/v trisodium citrate was added dropwise until all the citrate was used. AuNp's were then spectroscopically measured using UV-Vis to confirm the size and distribution.

AuMeLD's were formed from the mixture of a 3.5 μM Dibenzotetrathiafulvalene (DBTTF) solution and the gold nanoparticle solution. The DBTTF solution is prepared in 3:1 $HCCl_3$:EtOH, as the ethanol was required to act as a carrier for the DBTTF between the aqueous and organic phases. The solutions were added together in a 2.5 mL vial and subsequently alternated between sonication and vortexing for thorough mixing of the organic and aqueous phases. The scavenging of the gold nanoparticles from the aqueous

solution was confirmed through a color change present in the aqueous layer, wherein it transitioned from a deep red color to a blue color. This is due to the starting of agglomeration of the nanoparticles. As the mixing continued, the organic phase developed a distinctive shiny golden color indicating the formation of the metamaterial surface. This process is demonstrated in Figure 1.

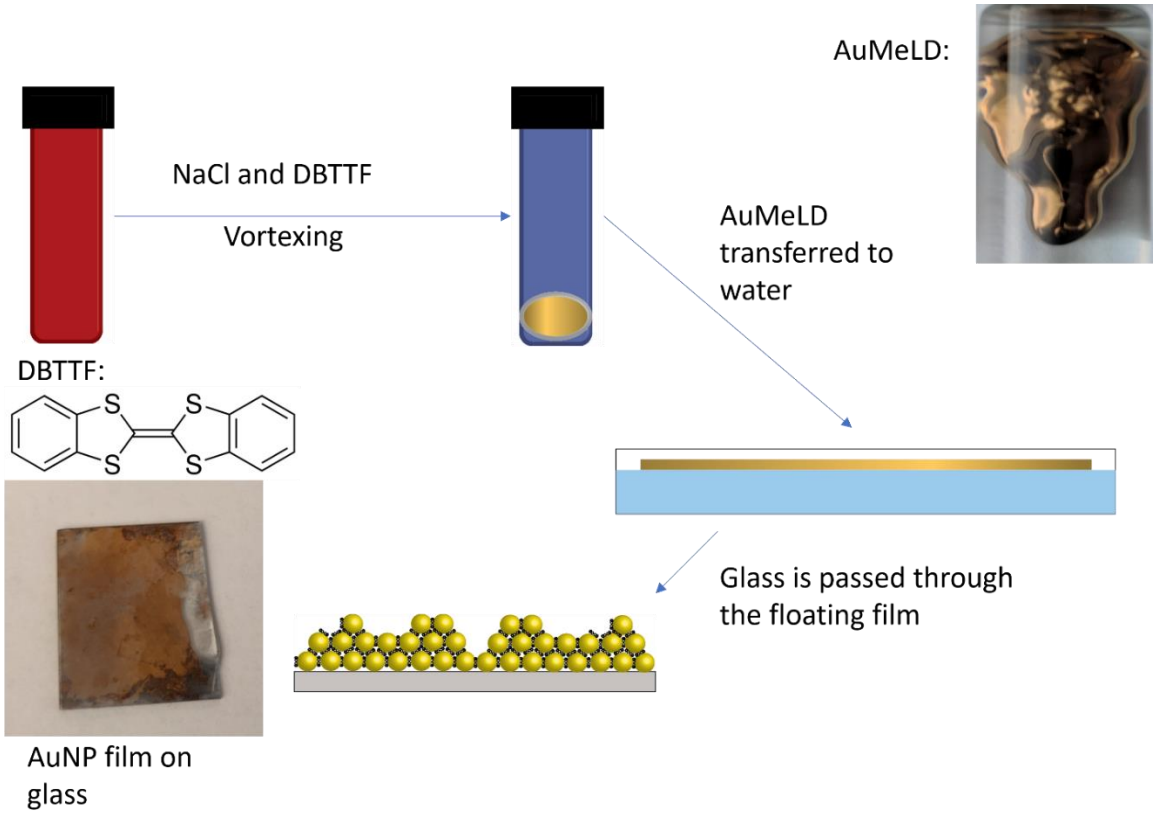


**Figure 5.1** The workflow to fabricate AuMeLDs, from nanoparticles to surface transferal.

The solid substrate was formed by depositing the metamaterial layer, which was selectively pipetted from the organic layer, onto a glass slide. The residual solvent was then air dried and the surface was washed 3 times with alternating ethanol and ultrapure water

washes to remove excess citrate and DBTTF. The structure of the solid-backed AuMeLD metamaterial is confirmed through a Dimension 3100 Nanoman AFM and a ThermoFisher Scientific NNS450.

An alternative method of nanoparticle film formation is achieved through the usage of a polyaniline film, a positively charged polymer. The citrate capped nanoparticles were attracted to the polymer and formed a self-assembled monolayer. In addition, self-assembled AuNP's were also tested on bare glass to confirm the benefits of a rigid linker.

SPR measurements were performed on Nano6 NanoSPR [28]. The sensitivity to refractive index was determined using serially diluted glucose solutions. PCB-126 solutions were prepared to 500 uM concentration in acetone. 1 uL of solution was then drop casted onto the AuMeLD substrate, and subsequently air dried before use. Graphene Oxide was fabricated using established protocols[26] and was drop-casted onto a subset of AuMeLD surfaces for comparison.

FDTD simulations were performed using EM Explorer software. The refractive indexes of Au and BK7 glass were obtained from web databases.[29, 30] Simulations were performed with a Yee cell size of 5 nm, 5 nm, and 1 nm in the *x*, *y* and *z* axis respectively. These results were compared to UV-vis results obtained using ATR dove prism reflection.

Raman measurements were performed using a Horiba LabRam instrument. The 552 nm laser's power was 60mW with 10% laser power being used to prevent surface damage of the substrate. The objective lens was x50 LW. System setting was set with an accumulation time of 5s with 5 accumulations per measurement, with smoothing

performed by the LabSpec6 software. Further fitting was performed, if necessary, with the Othala Raman package software, and further analysis was performed through RamanToolSet.[31]

### 5.3 Results & Discussion:

### Surface Characterization:

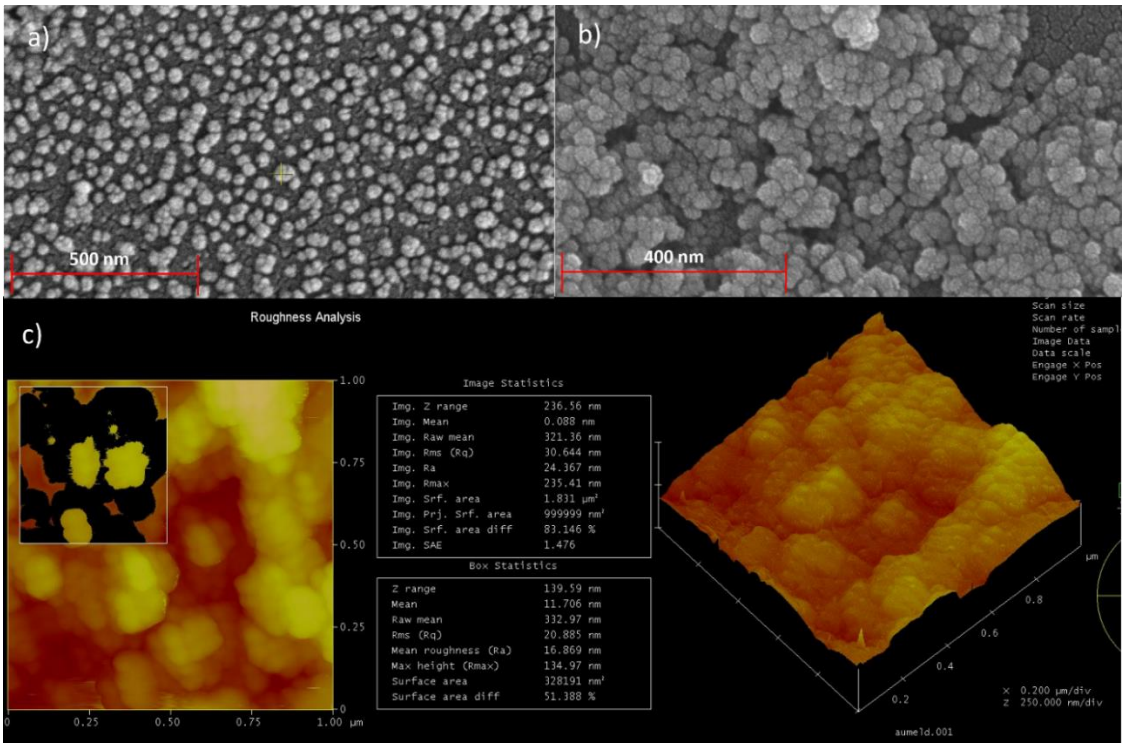


**Figure 5.2** a) SEM image of AuNP's formed onto a PAH surface. b) SEM image of AuMeLD. c) AFM image of AuMeLD including measurements of surface roughness.

SEM and AFM results indicate the structural formation of the nanoparticle film fabricated using the AuMeLD formation. As can be seen in Figure 1, DBTTF as a linker forms a hexagonally close packed structure that is tightly ordered forming the nanogap

necessary for SERS. Conversely, the AuNP film assembled onto the PAH substrate did not form tight structure and therefore lacked the nanogap requirement that facilitates optimal SERS. The AFM further confirmed the packing of the AuNP's as well as the overall surface roughness, which is particularly important for SPR measurements. The thickness of the AuMeLD film was greater than the size of an individual NP, with a trilayer as the predominant formation. This effect is due to the dimensions of the interfacial area between the organic and aqueous phases.

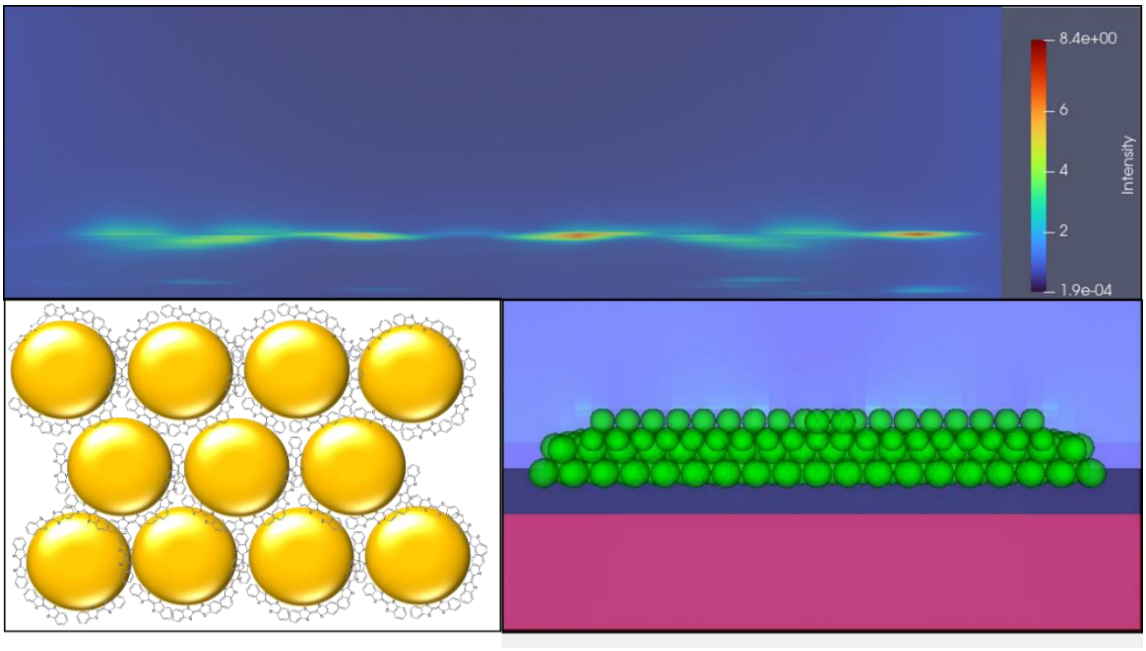


**Figure 5.3.** FDTD of hexagonally packed gold nanoparticles, demonstrating both LSPR and SPR behavior. A scheme depicting the surface packing of AuNP's and coverage of the AuNP's by DBTTF.

Based upon the SEM and AFM results, FDTD was used to simulate the system and confirm the presence of hotspots in the metamaterial necessary for SERS. The spacing and packing of the nanoparticles was determined by the SEM and length of DBTTF. In addition to the hotspot formation that was seen with FDTD, the formation of a larger evanescent wave was also observed. The metamaterial nature is demonstrated in Figure 3, wherein the hot spot formation can be seen on the surface of the nanoparticle assembly, while also a larger evanescent pattern is also formed. This is definitional for a metamaterial as the system demonstrates LSPR and SPR effects. This can then further be confirmed with

UV-vis spectroscopy for the LSPR and with Krestchmann configuration angle dependent spectroscopy for the SPR effect.

**LSPR and SPR:**

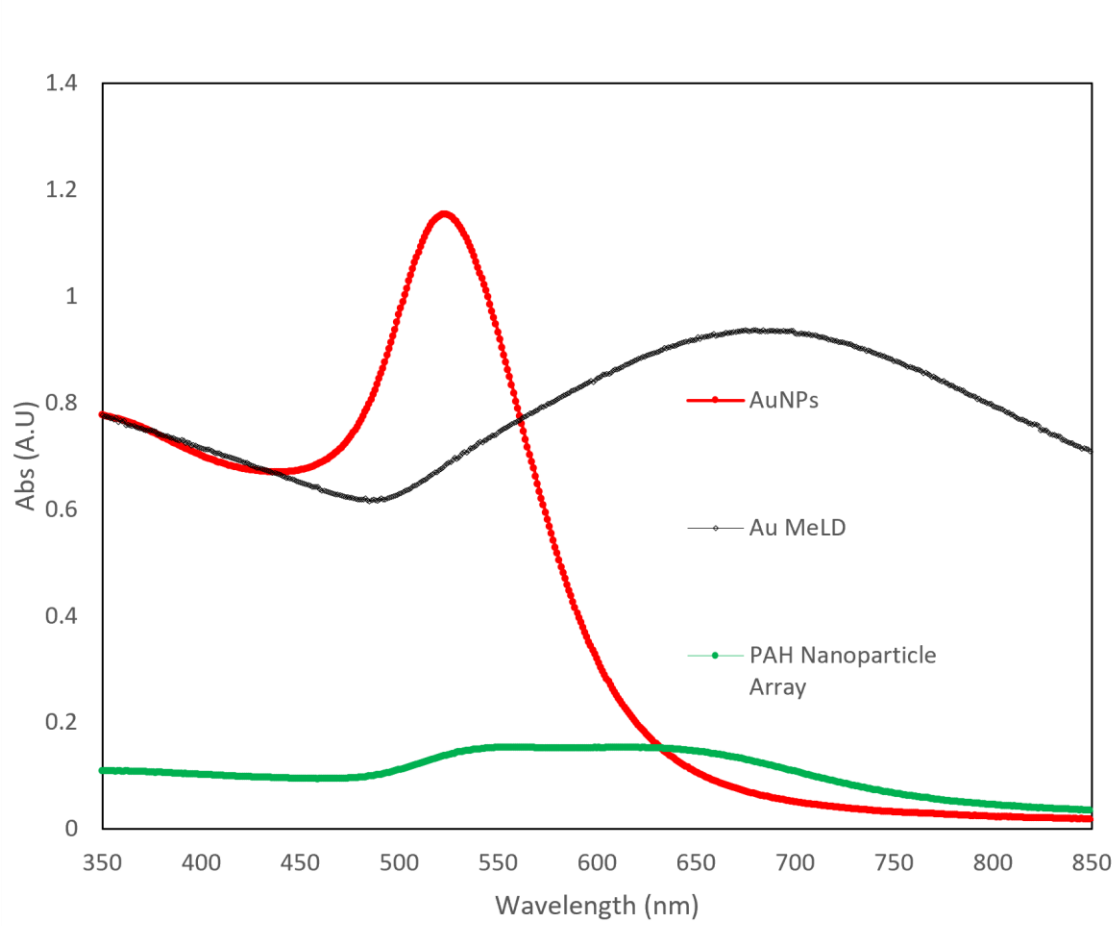


**Figure 5.4.** A comparison in the UV-vis spectra of the AuNP's, and the AuMeLD and PAH nanoparticle fabricated from said AuNP's.

To further confirm the differences between the PAH film and AuMeLD film, UV-vis was performed, and peak intensity and full-width half maximum were compared, as shown in Figure 4. The PAH film lacks surface coverage indicative by the relatively low

absorbance and lacks surface consistency noted by the broad peak width. The peak maximum of the AuNP's also corresponds to the size of NP. Notably, the AuMeLD spectrum was significantly red shifted due to the formation of the nanoparticle array, with a high absorbance indicative of high surface coverage. Further spectroscopic techniques were used for confirmation of the thin film nature of the metamaterial which cannot solely be determined through UV-vis spectroscopy.

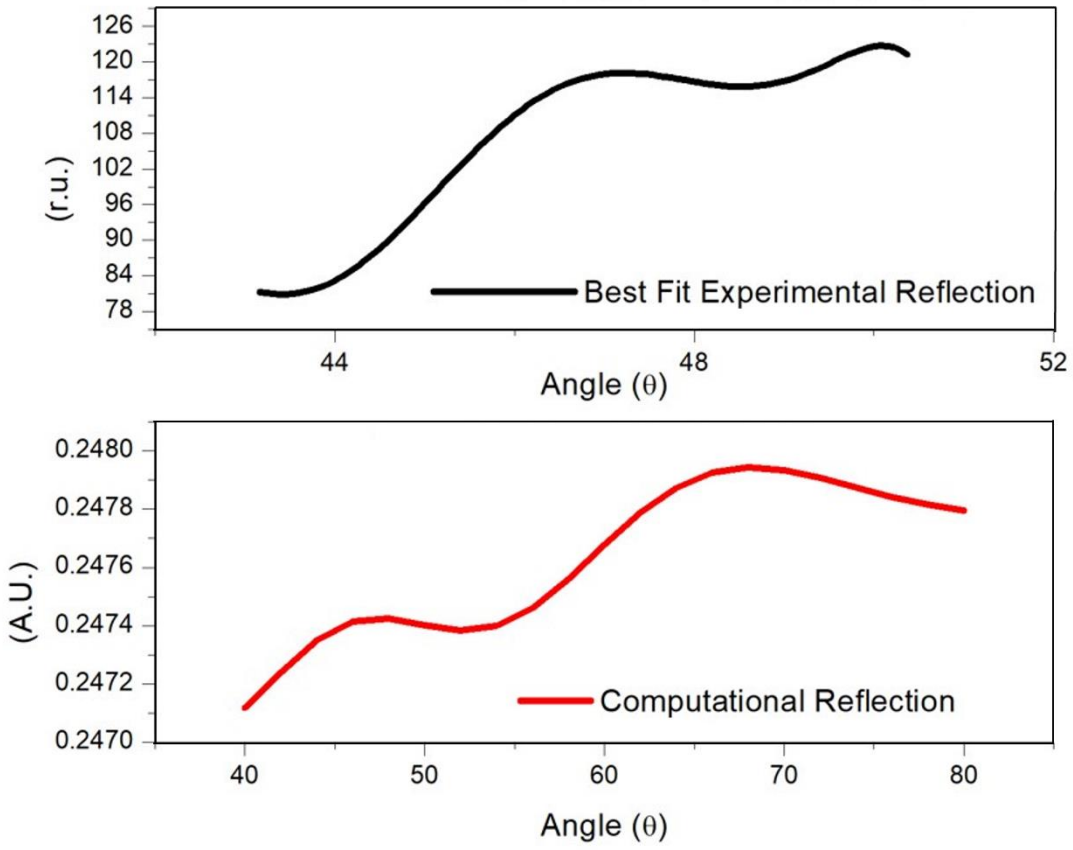


**Figure 5.5.** Comparison of the experimental and theoretical reflection of 650 nm light onto the AuMeLD surface.

To confirm the metamaterial nature of the AuMeLD surface, the macro thin film behavior had to be demonstrated. This is confirmed through reflection measurements, as if solely LSPR behavior was found, the incident angle would not influence the spectra. The structural differences between the simulated ideal and the real system account for the computed reflection differences in the specific plasmonic angle. The angle dependent response indicated a potential usage as a refractive index sensor for SPR applications. The capability as an SPR sensor is further confirmed through a sequential calibration of sensitivity to refractive index using serially diluted glucose solutions as seen in Figure 4. The sensitivity to refractive index changes was greater than what is traditionally found with a 50 nm gold film. However, the error for a system as simple as glucose solutions was too large to demonstrate feasibility as a refractive index sensor. While the thin film nature of the AuMeLD metamaterial is not optimal for usage as an SPR sensor, there are other benefits of metamaterials regarding their ordered structure that allow for increased SERS sensitivity.

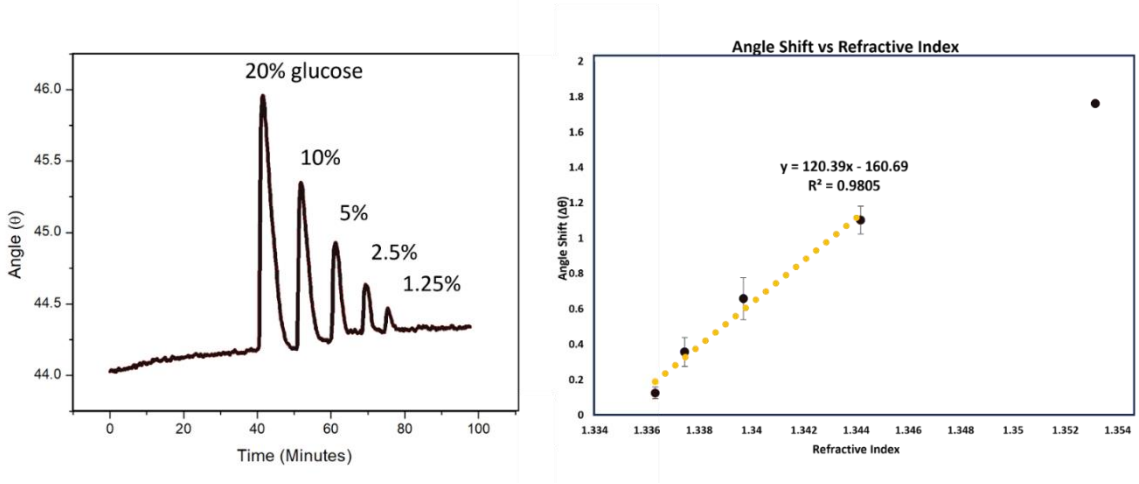


**Figure 5.6.** A sensogram demonstrating the change in reflected angle based upon bulk refractive index change. Calibration curve with triplicate measurements comparing the angle shift to the refractive index of the bulk.

**SERS Sensitivity:**

Initial SERS of the AuMeLD was compared to powdered DBTTF as well as a variety of alternative plasmonic platforms. DBTTF was used as the initial analyte for comparison due to being fundamentally present in the AuMeLD system. The concentration of DBTTF drop-casted onto the substrates was equivalent to the concentration of DBTTF in the solutions used for AuMeLD formation. As can be seen in Figure 7, AuMeLD has the most significant enhancement compared to Al, Au, and self-assembled AuNP's. Whereas Al and Au demonstrated almost no SERS signal, self-assembled AuNP's did due to the presence of LSPR hotspots, although they are not comparable to the enhancement of the AuMeLD. This confirmed the enhancement effect in the simplest case, of the already

present interfacial glue, and therefore a continuation of evidence demonstrating SERS enhancement was performed using a model compound.

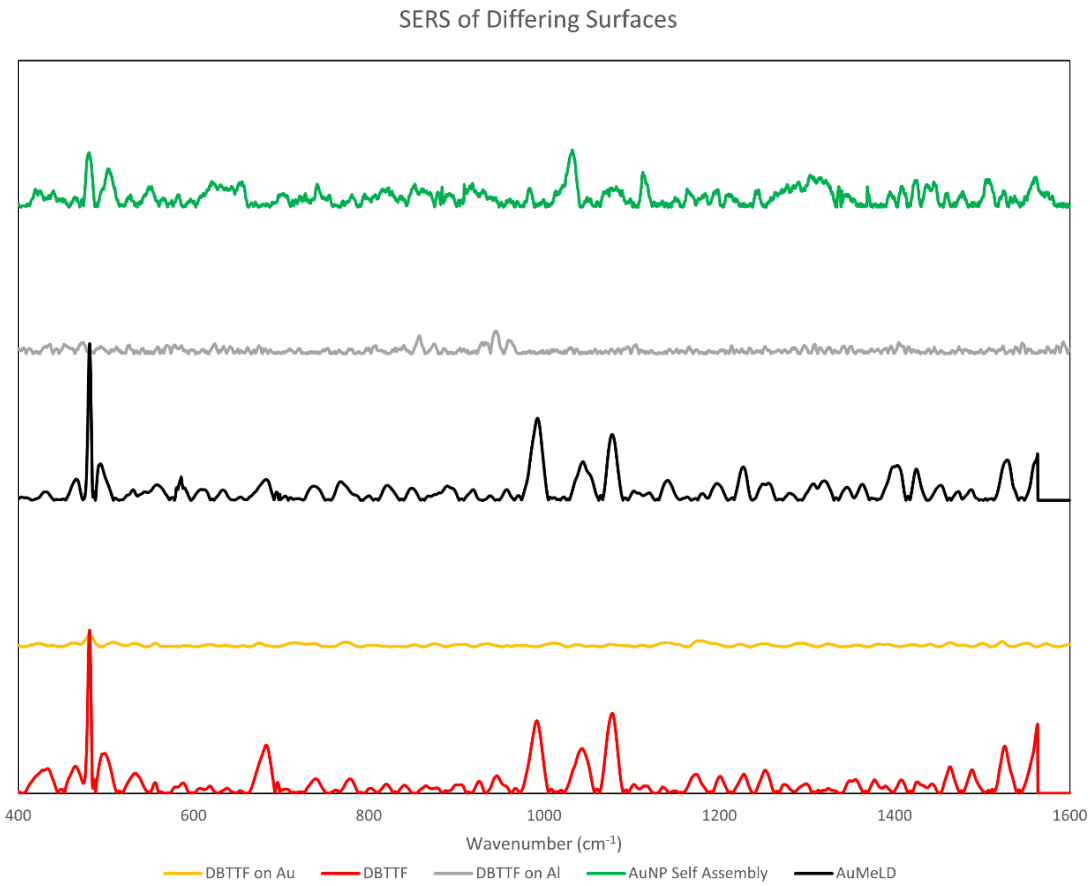


**Figure 5.7.** Comparison of the SERS signal of 3.5 µM DBTTF on a variety of plasmonic substrates (Al, Au, AuNP self-assembly, and AuMeLD) to the powdered DBTTF.

Lipoamide was chosen to confirm the viability of the surface as a sensor, a well-controlled surface binding paradigm as well as a biologically relevant metabolite. [32] The covalent binding of the dithiol to the Au surface allowed for direct proximity to the hotspots necessary for SERS. The concentrations of lipoamide deposited onto the AuMeLD surface were serially diluted to determine the overall sensitivity to the analyte. The peak of 1132

$cm^{-1}$ was chosen as the signature peak for lipoamide due to being correlated with lipoic acid in other work and not overlapping with the present DBTTF peaks.[33] The linear range of detection was from mM to aM concentrations. The detectable range is comparable to the detection of lipoic acid using silver SERS substrates, where nM concentrations were found to be the limit of detection.[33] In a gold system the gold-thiol bond is the prominent mediator. However, in this silver system with a lack of gold, the lipoic acid adsorbed using the carboxylate group. This effect explains the increased sensitivity of the Au SERS system towards lipoamide due to the strong covalent nature of the thiol-gold bond. Further SERS testing is still necessary, using an analyte that does not covalently bond to the surface, corroborating the SERS efficacy of the sensor.

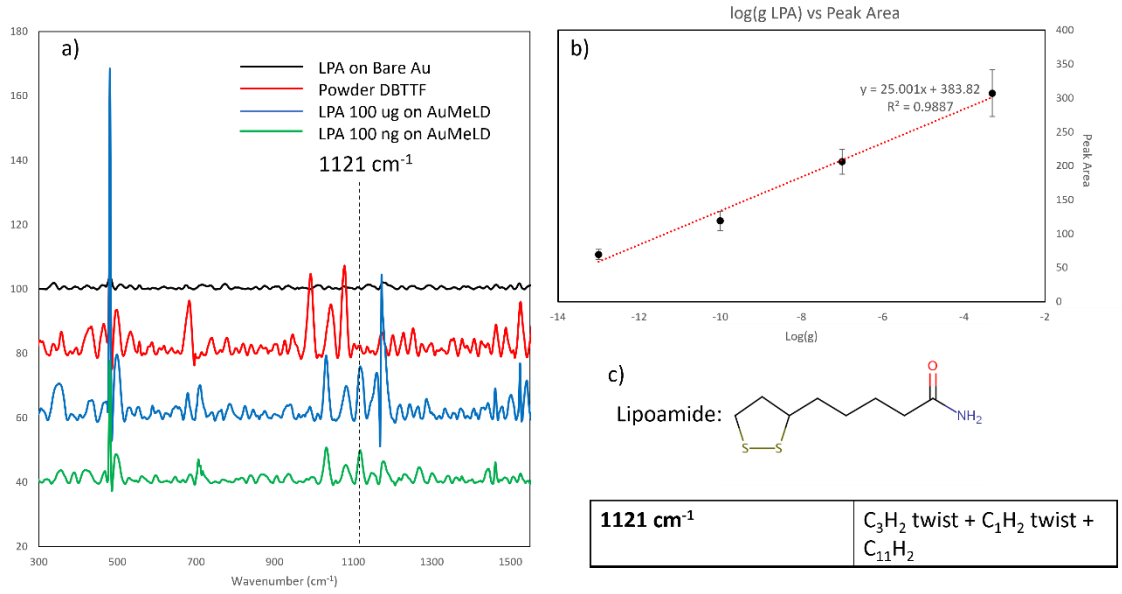


**Figure 5.8**. a) SERS spectra of lipoamide compared to bare DBTTF and bare gold. b) Calibration curve of lipoamide using peak 1121 $cm^{-1}$ c) Peak assignment of 1121 $cm^{-1}$

The SERS analyte chosen was PCB-126 because PCB's are common environmental toxins, and the highly aromatic structure present provides a distinct SERS fingerprint that makes them an ideal substrate to analyze. PCB-126 and other dioxin-like PCB's have been associated with a variety of diseases through binding to aryl hydrocarbon receptors wherein PCB-126 is the strongest binder in the PCB series.[23] Binding to this receptor leads to a variety of health effects, including disrupting inflammation pathways, embryonic development, and effecting gut microbiota.[34-36] In addition to this, detection of PCB-126 has not been fully studied using SERS, whereas other PCB's such as PCB-47 and PCB-77 are well documented.

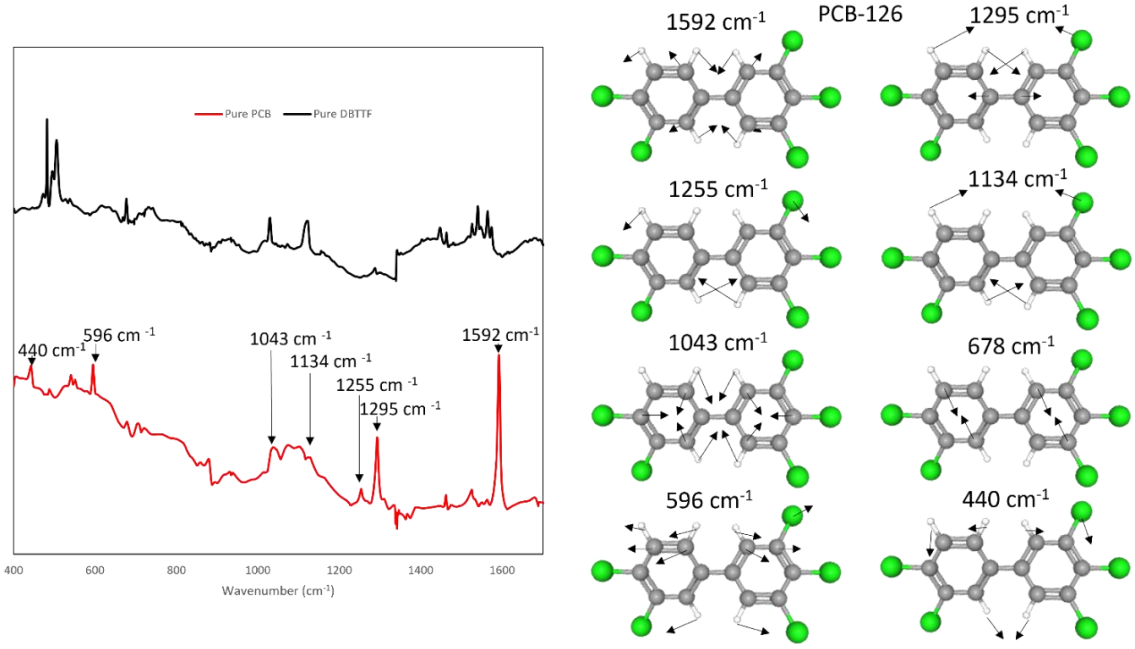


**Figure 5.9.** Specific peaks of PCB-126 can be used that do not overlap with the peaks present in DBTTF and can be used for PCB-126 detection. In addition, the Raman peaks

can be associated with simulated movements of the PCB based upon the work of Lai et al. [37]

Raman spectra for both powdered DBTTF and powdered PCB-126 were compared to determine the spectral peaks that lack overlap. In addition, this work done by Lai et al has predicted the Raman spectra for the entire series of PCB molecules and attributed them to specific vibrational modes.[37] These theoretical results match the results of our experimental pure PCB-126 sample. Based upon the distinct PCB-126 peaks at 1593 $cm^{-1}$, 1300 $cm^{-1}$ and 567 $cm^{-1}$, the analyte was separated from the distinct peaks of the interfacial glue. The distinct peaks of the glue, however, can be used as an internal standard as the concentration of DBTTF on the surface is consistent since it is solely dependent on the loading efficiency of the AuNP's. As these peaks can be attributed to specific vibrational modes in the PCB molecule, an understanding of the chemical enhancement caused by the presence of DBTTF can be determined. Confirmation of the chemical enhancement can be achieved through a multistep comparison in SERS signal between the self-assembled AuNp's on glass, and the AuMeLD. Comparison between the self-assembled AuNP's and the AuMeLD confirms the necessity of the interfacial glue for SERS enhancement, through both the chemical enhancement caused by the DBTTF and the increased SERS enhancement due to the consistent nanogap formation caused by the DBTTF. The concentration of PCB-126 used for this testing is 1.534 µM. The detectable PCB-126 is equivalent to the concentrations detected using other PCB SERS systems. [26]

**SERS Orientation:**

Of note is the difference between the peaks of the powder PCB-126 sample and that of the PCB-126 on AuMeLD. Generally, it would be expected that the highest intensity peak would remain the prominent peak under enhancement. However, this is not the case with this system wherein the most prominent SERS peak is at 560 $cm^{-1}$ and 612 $cm^{-1}$, compared to the powder sample peaks at 1593 $cm^{-1}$ and 1293 $cm^{-1}$ with only minor peaks at 560 $cm^{-1}$ and 600 $cm^{-1}$. This effect has previously been attributed to chemical enhancement caused by SERS. To further explore this the same system was analyzed with a graphene-AuMeLD surface. Both DBTTF and graphene form π-π stacking interactions causing PCB-126 to preferentially bind the parallel to the respective molecule. In this way PCB-126 will be oriented parallel to the nanoparticle as opposed to perpendicular as shown in Figure 10.

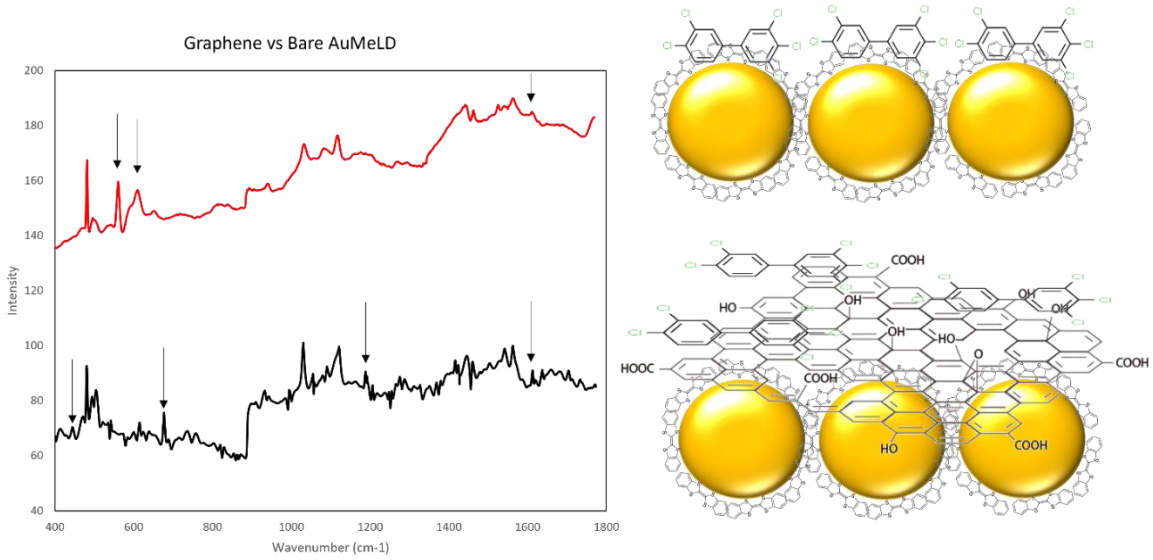


**Figure 5.10**. The differing SERS spectra between a bare AuMeLD surface, and an AuMeLD surface with a layer of graphene. The position of PCB-126 relative to the nanoparticle surface, dependent on the graphene modification.

The differences in the peak enhancement between the graphene system and bare AuMeLD can be correlated to the directionality of PCB-126 on the surface relative to the position of the nanoparticle. SERS is dependent on the cross-section of the molecule relative to the excitation source and the ability of the bonds to vibrate, with both effects being causes of the selective enhancement shown. Similarly, vibrational modes that are normally considered to be Raman forbidden can be seen in SERS systems.[38] Based upon Figure 9, the differing relative peak intensities of PCB-126 can be seen with two differing chemical systems with identical plasmonic structure. The differing signal indicates that there is specific enhancement caused by the DBTTF presence due to the relative positions of the analyte relative to the nanoparticle surface. Notably there is the presence of the 440

$cm^{-1}$, 677 $cm^{-1}$, 1192 $cm^{-1}$, and 1614 $cm^{-1}$ peaks that are present with graphene surface and not with a bare AuMeLD. Similarly, the prominent peaks in the bare AuMeLD sample are not present at all, indicating a distinct difference in the chemical enhancement caused by the SERS. In this way AuMeLD sensors demonstrate a method to distinguish different Raman responses in a molecule through semi-selective enhancement induced by the positional effect. This system is focused towards highly aromatic systems to take advantage of the rigidity of the substrate and specific binding of π systems.

### 5.4 Conclusion

In this work we have demonstrated the fabrication of a SERS metamaterial substrate with an interfacial glue and gold nanoparticles to form an ordered thin film. This film is then used for SERS detection of a dithiol containing metabolite, lipoamide, with a LOD in the aM range which is below previously reported results for similar metabolites using SERS. To further elaborate on the uses of the substrate for SERS detection, an environmental toxin, PCB-126, was detected and distinct changes in the relative intensities of the Raman spectra. This phenomenon spurred further investigation into the chemical enhancement effects caused by SERS through the application of graphene oxide to the AuMeLD surface. Further work with this substrate can explore the effect of the binding position of the analyte on the resulting SERS signal. This effect could be further explored through simulations of the vibrational modes of PCB-126 to then compare it to the experimental results.

## 5.6 References:


1. Holzinger, M., A. Le Goff, and S. Cosnier, *Nanomaterials for biosensing applications: a review.* Front Chem, 2014. **2**: p. 63.

2. Kamal Eddin, F.B. and Y.W. Fen, *The Principle of Nanomaterials Based Surface Plasmon Resonance Biosensors and Its Potential for Dopamine Detection.* Molecules, 2020. **25**(12).

3. Bolduc, O.R. and J.F. Masson, *Advances in surface plasmon resonance sensing with nanoparticles and thin films: nanomaterials, surface chemistry, and hybrid plasmonic techniques.* Anal Chem, 2011. **83**(21): p. 8057-62.

4. Zhu, C., et al., *Electrochemical sensors and biosensors based on nanomaterials and nanostructures.* Anal Chem, 2015. **87**(1): p. 230-49.

5. Squires, T.M., R.J. Messinger, and S.R. Manalis, *Making it stick: convection, reaction and diffusion in surface-based biosensors*. Nat Biotechnol, 2008. **26**(4): p. 417-26.

6. Baek, W., et al., *Recent Advances and Prospects in Colloidal Nanomaterials.* JACS Au, 2021. **1**(11): p. 1849-1859.

7. Lambert, A.S., et al., *Plasmonic Biosensing with Aluminum Thin Films under the Kretschmann Configuration.* Anal Chem, 2020. **92**(13): p. 8654-8659.

8. Salim, A. and S. Lim, *Recent advances in the metamaterial-inspired biosensors.* Biosens Bioelectron, 2018. **117**: p. 398-402.

9. Bantz, K.C., et al., *Recent progress in SERS biosensing.* Phys Chem Chem Phys, 2011. **13**(24): p. 11551-67.

10. Kutrovskaya, S., et al., *Nanocomposite Metamaterials Based on Self-assembled Titanium Dioxide Rolls with Embedded Gold Nanoparticles.* Sci Rep, 2019. **9**(1): p. 7023.

11. Tan, K.H., et al., *Fabrications of Nanocomposite Gold-Polymer Metamaterials Consisting of Periodic Microcavities with Tunable Optical Properties.* Optik, 2017. **150**: p. 54-61.

12. Evgeny Smirnov, M.l.D.S., Dmitry Momotenko, Heron Vrubel, Manuel A. Me´ndez, Pierre-Francois Brevet, and Hubert H. Girault, *Gold Metal Liquid-Like*

*Droplets.* ACS Nano, 2014. **8**: p. 9471–9481.

13. Golubina, E.N. and N.F. Kizim, *Interfacial Synthesis: Morphology, Structure, and Properties of Interfacial Formations in Liquid–Liquid Systems.* Russian Journal of Physical Chemistry A, 2021. **95**(4): p. 659-676.

14. Sokolowska, K., et al., *Dithiol-Induced Oligomerization of Thiol-Protected Gold Nanoclusters.* J Phys Chem C Nanomater Interfaces, 2018. **122**(23): p. 12524-12533.

15. Lee, D. and S. Yoon, *Effect of Nanogap Curvature on SERS: A Finite-Difference Time-Domain Study.* The Journal of Physical Chemistry C, 2016. **120**(37): p. 20642-20650.

16. Evgeny Smirnov, P.P., Michea´ l D. Scanlon, Hubert H. Girault, *Interfacial Redox Catalysis on Gold Nanofilms at Soft Interfaces.* ACS Nano, 2015. **9**: p. 6565–6575.

17. Avni, A., et al., *Single-droplet surface-enhanced Raman scattering decodes the molecular determinants of liquid-liquid phase separation.* Nat Commun, 2022. **13**(1): p. 4378.

18. Tian, L., et al., *Liquid-state quantitative SERS analyzer on self-ordered metal liquid-like plasmonic arrays.* Nat Commun, 2018. **9**(1): p. 3642.

19. Vo-Dinh, T., *SERS chemical sensors and biosensors" new tools for environmental and biological analysis.* Sensors and Actuators B: Chemical, 1995. **29**: p. 183-189.

20. Aitekenov, S., et al., *SERS for Detection of Proteinuria: A Comparison of Gold, Silver, Al Tape, and Silicon Substrates for Identification of Elevated Protein Concentration in Urine.* Sensors (Basel), 2023. **23**(3).

21. Benesova, M., et al., *SERS-Tags: Selective Immobilization and Detection of Bacteria by Strain-Specific Antibodies and Surface-Enhanced Raman Scattering.* Biosensors (Basel), 2023. **13**(2).

22. Bodelon, G. and I. Pastoriza-Santos, *Recent Progress in Surface-Enhanced Raman Scattering for the Detection of Chemical Contaminants in Water.* Front Chem, 2020. **8**: p. 478.

23. Zhang, W., et al., *PCB 126 and other dioxin-like PCBs specifically suppress hepatic PEPCK expression via the aryl hydrocarbon receptor.* PLoS One, 2012.

**7**(5): p. e37103.

24. Cheng, R., et al., *A highly sensitive and selective aptamer-based colorimetric sensor for the rapid detection of PCB 77.* J Hazard Mater, 2018. **341**: p. 373-380.

25. Cheng, J., P. Wang, and X.-O. Su, *Surface-enhanced Raman spectroscopy for polychlorinated biphenyl detection: Recent developments and future prospects.* TrAC Trends in Analytical Chemistry, 2020. **125**.

26. Shanta, P.V. and Q. Cheng, *Graphene Oxide Nanoprisms for Sensitive Detection of Environmentally Important Aromatic Compounds with SERS.* ACS Sens, 2017. **2**(6): p. 817-827.

27. JOHN TURKEVICH, P.C.S., JAMES HILLI, *A STUDY OF THE NUCLEATION AND GROWTH PROCESSES IN THE SYNTHESIS OF COLLOIDAL GOLD.* Discussion of the Faraday Society, 1951. **11**: p. 55-75.

28. McKeating, K.S., et al., *Antifouling Lipid Membranes over Protein A for Orientation-Controlled Immunosensing in Undiluted Serum and Plasma.* ACS Sens, 2019. **4**(7): p. 1774-1782.

29. Shott, C. *SCHOTT Zemax catalog 2017-01-20b*. 2017.

30. P. B. Johnson, R.W.C., *Optical Constants of the Noble Metals.* Phys. REv. B, 1972. **6**.

31. Charron, B., V. Thibault, and J.F. Masson, *Combining multilayered wrinkled polymer SERS substrates and spectral data processing for low concentration analyte detection.* Anal Bioanal Chem, 2022. **414**(18): p. 5719-5732.

32. Shen, W., et al., *Lipoamide or lipoic acid stimulates mitochondrial biogenesis in 3T3-L1 adipocytes via the endothelial NO synthase-cGMP-protein kinase G signalling pathway.* Br J Pharmacol, 2011. **162**(5): p. 1213-24.

33. Rusu, E.A., et al., *Vibrational analysis of α-lipoic acid and its adsorption behavior study by SERS.* Journal of Molecular Structure, 2022. **1248**.

34. Teixido, E., et al., *Cardiovascular Effects of PCB 126 (3,3',4,4',5-Pentachlorobiphenyl) in Zebrafish Embryos and Impact of Co-Exposure to Redox Modulating Chemicals.* Int J Mol Sci, 2019. **20**(5).

35. Wang, C., et al., *PCB 126 induces monocyte/macrophage polarization and inflammation through AhR and NF-kappaB pathways.* Toxicol Appl Pharmacol,

2019. **367**: p. 71-81.

36. Zhang, Y., et al., *Dioxin-like polychlorinated biphenyl 126 (PCB126) disrupts gut microbiota-host metabolic dysfunction in mice via aryl hydrocarbon receptor activation.* Ecotoxicol Environ Saf, 2022. **236**: p. 113448.

37. Lai, Y., et al., *Theoretical evaluation of the configurations and Raman spectra of 209 polychlorinated biphenyl congeners.* Chemosphere, 2011. **85**(3): p. 412-7.

38. Chulhai, D.V. and L. Jensen, *Determining Molecular Orientation With Surface-Enhanced Raman Scattering Using Inhomogenous Electric Fields.* The Journal of Physical Chemistry C, 2013. **117**(38): p. 19622-19631.

# Chapter 6: Conclusion and Future Perspectives

## 6.1 Summary of Dissertation Work

The work discussed in this dissertation focused on the development of plasmonic substrates with initial development focused on simulations to a realized sensor chip for eventual biological and environmental applications. Initially this was performed through optical simulations to best predict the behavior of aluminum thin films as an SPR substrate, which demonstrated increased sensitivity compared to the conventional gold substrates. The aluminum system was then fabricated and a new SPR material was now available for further sensor development. Not only were SPR sensors the sole target, but SERS sensors also were found to be a powerful plasmonic tool, particularly in the detection of small molecules that are common pollutants. The understanding of biological systems through biosensors has grown on the back of bioanalytical devices which require the further development of the fundamental basis of said sensor. Furthering the surface substrate for the purposes of SPR and SERS reveal new possibilities and properties in the understanding of biologically important molecules. There are many directions with which the new surface technologies could follow, but I will be focusing on the usage of aluminum substrate and taking advantage of the novel plasmonic behavior for the purposes of furthering biological sensing.

## 6.2 Potential Future Research Areas

### 6.2.1 Aluminum SPR

In Chapter 2&3 of this work we discuss the development and application of aluminum thin films for SPR. In Chapter 3 there is particular discussion of the effects of thick aluminum oxide on the plasmonic response with regards to excitation light polarization and the specific response to refractive index changes in the bulk versus the surface. In this work the theoretical case is explored and the specific expected response and optimized surface characteristics.

The direct experimental application of the waveguide aluminum/aluminum oxide surface discussed in Chapter 3 with existing instrumentation has not been explored. The formation of the oxide surface would have to be undertaken using RF sputtering.[1] Whereas previous methods of oxide deposition that have been previously discussed such as physical evaporation chemical vapor deposition are powerful tools for silicon oxide, the same are not available for aluminum oxide.[2-4] RF sputtering in particular is required due to the difficulty in the formation of aluminum oxide vapor and the quality of the film. Precision is required in the deposition of the aluminum oxide as waveguide formation has very narrow matching conditions.[5] Furthermore, structural integrity of the oxide layer must be determined as the increased thickness reduces film integrity.[6] This is particularly important when coupled to instrumentation as microfluidic flow-cells induces extra pressure onto the thin film. To take full advantage of the waveguide behavior of the chip, modifications to existing instrumentation is necessary to quickly alternate between s and p polarizations. Automated polarization changes allows for a sensor that takes advantage of the differences in sensitivity between s-polarization sensitivity to bulk and surface refractive index changes equally, and the p-polarized response which differs between the

method with which the refractive index shifts. This effect can be confirmed through classical SPR experiments using polymer growth and bulk shifts with salt solutions.[7] This system could then be applied for more complex chemical studies such as biological systems.

The study of protein conformation changes in real-time is a difficult process, and most methods rely upon fluorescent labels.[8] While fluorescence is a powerful tool, the label can effect the structure of the protein of interest and therefore limit the explorable systems.[9] Specifically, this would allow SPR to detect changes induced by small molecular binder which cause protein conformer changes. Under normal SPR conditions, the minimal changes induced by protein conformer changes would not be detectable due to the bulk shift induced by the small reducing preventing the specific detection of the protein signal.[10] However, the aforementioned SPR sensor with the ability to distinguish between surface and bulk refractive index changes would allow for a more precise measurement said changes in protein structure on the surface of the oxide.

There are a variety of proteins of possible study of their conformer effects. A wide range of proteins can be studies in this method, including Abelson tyrosine kinase, a known cancer related protein with an FDA approved drug, imatinib.[11] This system has been thoroughly studied using molecular dynamics simulations in conjunction with protein crystallography and NMR.[12-14] In this particular system problems can arise due to the relative small conformer changes which may make detection difficult even with the ability to distinguish between bulk and surface changes. A possible method to overcome this, would be to utilize a secondary binder that only binds to drug-protein complex, however

this would require extensive engineering regarding the chemical probe necessary, and would reduce the benefits of SPR as a method that is label free.[15-17] The strength of SPR detection is in the determination of kinetics with real time data acquisition, current protein conformer studies frequently focus on chemical specific changes using NMR, FTIR or mass spectrometry, the addition of SPR would provide supplemental information to these techniques.[18-21] Another example protein of interest is epidermal growth factor receptor (EGFR), although this demonstrates another difficulty of many of protein systems, their reliance upon sufficient cell mimicry (such as the presence of a lipid bilayer) for native protein folding. [22-25]

### 6.2.2 Autoimmune Disease Detection

As discussed in chapter 4, wherein anti-MAG is detected for the purposes of eventual use as a biomarker for diagnosis of anti-MAG associated neuropathy this platform could be similarly applied for other similar diseases. This would be achieved by taking advantage of the multiplexed nature of the SPRi platform, that can have an array of surface bound antigens associated with autoimmune diseases. Work similar to this has been done, focusing on the study of multiple sclerosis, although I propose that it could be expanded to more autoimmune diseases as there is frequently comorbidity among them.[26, 27]

The development of the array could contain a variety of antigens including but not limited to, GM1, GA1, GT1B, GQ1B, MAG etc.[28-31] The cross reactivity of the auto-immune antibodies for these can then be tested and compared, as well as eventual use in a mixed sample. To further distinguish between analyte responses, machine learning can be

employed with the large amount of information obtained by the array. Due to noted antifouling effects of perfluorinated surfaces, analyte detection could occur in whole serum. This could then be applied to patient samples for further understanding of these auto-immune neurological diseases. Through comprehensive analysis of a variety of auto-immune conditions and comparison between them accurate diagnosis based upon antibody levels is a possibility.

### 6.2.3 SERS

SERS is a powerful tool in the detection and understanding of the chemistry of molecular vibrations. SERS greatest strength, the ability to detect the presence of many chemical bonds, is also its downside due to the overlap between a variety of bonds and the inconsistencies induced by the enhancing surface.[32] In the work discussed in Chapter 5, an interesting effect is observed wherein based upon the surface chemistry and subsequent interactions with the analyte of choice, specific SERS peaks can be more selectively enhanced. Further data analysis to process and interpret SERS data would be very beneficial to better understand this effect.

To properly take advantage of the benefits of SERS and more modern analysis techniques, machine learning becomes a powerful tool in SERS analysis.[33-36] Random forest machine learning models not only support the identification of whole SERS spectra from each other, but can also establish significant peaks allowing for a better understanding of how the spectra separation occurs.[37, 38] This can be applied to systems that are very similar, such ones with minor surface chemistry differences, to determine which Raman

bands are being enhanced by SERS upon specific molecular orientation relative to the surface. The amount of data provided by SERS and the aforementioned complexity of the data makes machine learning an ideally suited technique in the data analysis process.

## 6.3 References:


1. Pletincx, S., et al., *In Situ Methanol Adsorption on Aluminum Oxide Monitored by a Combined ORP-EIS and ATR-FTIR Kretschmann Setup.* The Journal of Physical Chemistry C, 2018. **122**(38): p. 21963-21973.

2. M. D. Groner, F.H.F., J. W. Elam, and S. M. George, *Low-Temperature Al2O3 Atomic Layer Deposition.* Chem. Mater., 2004. **16**: p. 639-645.

3. Hom-on, C., et al., *Surface roughness of aluminum oxide thin films deposited by DC and RF reactive magnetron sputtering.* Materials Today: Proceedings, 2018. **5**(7): p. 15228-15232.

4. Chen, S., et al., *RF Magnetron Sputtering Aluminum Oxide Film for Surface Passivation on Crystalline Silicon Wafers.* International Journal of Photoenergy, 2013. **2013**: p. 1-5.

5. Tuniz, A., et al., *Plasmonic Sensors beyond the Phase Matching Condition: A Simplified Approach.* Sensors (Basel), 2022. **22**(24).

6. Lin, S.C., et al., *Fabrication of Aluminum Oxide Thin-Film Devices Based on Atomic Layer Deposition and Pulsed Discrete Feed Method.* Micromachines (Basel), 2023. **14**(2).

7. Walter, J.G., et al., *SPR Biosensor Based on Polymer Multi-Mode Optical Waveguide and Nanoparticle Signal Enhancement.* Sensors (Basel), 2020. **20**(10).

8. Harroun, S.G., et al., *Monitoring protein conformational changes using fluorescent nanoantennas.* Nat Methods, 2022. **19**(1): p. 71-80.

9. Arsic, A., et al., *Minimal genetically encoded tags for fluorescent protein labeling in living neurons.* Nat Commun, 2022. **13**(1): p. 314.

10. Mitchell, J., *Small molecule immunosensing using surface plasmon resonance.* Sensors (Basel), 2010. **10**(8): p. 7323-46.

11. Ayaz, P., et al., *Structural mechanism of a drug-binding process involving a large conformational change of the protein target.* Nat Commun, 2023. **14**(1): p. 1885.

12. Sonja Lorenz, P.D., Oliver Hantschel, Giulio Superti-Furga, and John Kuriyan, *Crystal structure of an SH2-kinase construct of c-Abl and effect of the SH2 domain on kinase activity.* Biochem J., 2015. **468**: p. 283-291.

13. Skora, L., et al., *NMR reveals the allosteric opening and closing of Abelson tyrosine kinase by ATP-site and myristoyl pocket inhibitors.* Proc Natl Acad Sci U S A, 2013. **110**(47): p. E4437-45.

14. Meng, Y., et al., *Predicting the Conformational Variability of Abl Tyrosine Kinase using Molecular Dynamics Simulations and Markov State Models.* J Chem Theory Comput, 2018. **14**(5): p. 2721-2732.

15. *A conversation on using chemical probes to study protein function in cells and organisms.* Nat Commun, 2022. **13**(1): p. 3757.

16. Licciardello, M.P. and P. Workman, *The era of high-quality chemical probes.* RSC Med Chem, 2022. **13**(12): p. 1446-1459.

17. Serafim, R.A.M., et al., *Covalent chemical probes for protein kinases.* Current Research in Chemical Biology, 2023. **3**.

18. Shoff, T.A. and R.R. Julian, *Fragment Ion Abundance Reveals Information about Structure and Charge Localization in Highly Charged Proteins.* J Am Soc Mass Spectrom, 2023. **34**(8): p. 1778-1788.

19. Usoltsev, D., et al., *Systematic FTIR Spectroscopy Study of the Secondary Structure Changes in Human Serum Albumin under Various Denaturation Conditions.* Biomolecules, 2019. **9**(8).

20. Jain, S. and A. Sekhar, *Elucidating the mechanisms underlying protein conformational switching using NMR spectroscopy.* J Magn Reson Open, 2022. **10-11**: p. 100034.

21. Petrotchenko, E.V. and C.H. Borchers, *Protein Chemistry Combined with Mass Spectrometry for Protein Structure Determination.* Chem Rev, 2022. **122**(8): p. 7488-7499.

22. Lee, N.Y., T.L. Hazlett, and J.G. Koland, *Structure and dynamics of the epidermal growth factor receptor C-terminal phosphorylation domain.* Protein Sci, 2006. **15**(5): p. 1142-52.

23. Carpenter, E.P., et al., *Overcoming the challenges of membrane protein crystallography.* Curr Opin Struct Biol, 2008. **18**(5): p. 581-6.

24. Lin, S.H. and G. Guidotti, *Purification of membrane proteins.* Methods Enzymol, 2009. **463**: p. 619-29.

25. Marinko, J.T., et al., *Folding and Misfolding of Human Membrane Proteins in Health and Disease: From Single Molecules to Cellular Proteostasis.* Chem Rev, 2019. **119**(9): p. 5537-5606.

26. Malinick, A.S., et al., *Detection of Multiple Sclerosis Biomarkers in Serum by Ganglioside Microarrays and Surface Plasmon Resonance Imaging.* ACS Sens, 2020. **5**(11): p. 3617-3626.

27. Nociti, V. and M. Romozzi, *Multiple Sclerosis and Autoimmune Comorbidities.* J Pers Med, 2022. **12**(11).

28. Herrendorff, R., et al., *Selective in vivo removal of pathogenic anti-MAG autoantibodies, an antigen-specific treatment option for anti-MAG neuropathy.* Proc Natl Acad Sci U S A, 2017. **114**(18): p. E3689-E3698.

29. Zhu, W., et al., *Detection of anti-ganglioside antibodies in Guillain-Barre syndrome.* Ann Transl Med, 2023. **11**(7): p. 289.

30. Wu, X., Y. Wang, and Z.Q. Xi, *Clinical and antibodies analysis of anti-GQ1b antibody syndrome: a case series of 15 patients.* Acta Neurol Belg, 2023. **123**(3): p. 839-847.

31. A S Bansal, B.A.-K., R A Malik, P Goulding, R S H Pumphrey, A J M Boulton, P L J Holt, P B Wilson, *IgM ganglioside GM1 antibodies in patients with autoimmune disease or neuropathy, and controls.* J Clin Pathol, 1994. **47**.

32. Sitjar, J., et al., *Challenges of SERS technology as a non-nucleic acid or -antigen detection method for SARS-CoV-2 virus and its variants.* Biosens Bioelectron, 2021. **181**: p. 113153.

33. Leong, Y.X., et al., *Surface-Enhanced Raman Scattering (SERS) Taster: A Machine-Learning-Driven Multireceptor Platform for Multiplex Profiling of Wine Flavors.* Nano Lett, 2021. **21**(6): p. 2642-2649.

34. Bantz, K.C., et al., *Recent progress in SERS biosensing.* Phys Chem Chem Phys, 2011. **13**(24): p. 11551-67.

35. Ciloglu, F.U., et al., *SERS-based sensor with a machine learning based effective feature extraction technique for fast detection of colistin-resistant Klebsiella pneumoniae.* Anal Chim Acta, 2022. **1221**: p. 340094.

36. Ju, Y., et al., *Identifying Surface-Enhanced Raman Spectra with a Raman Library Using Machine Learning.* ACS Nano, 2023. **17**(21): p. 21251-21261.

37. Seifert, S., *Application of random forest based approaches to surface-enhanced Raman scattering data.* Sci Rep, 2020. **10**(1): p. 5436.

38. Li, J.Q., et al., *Machine learning using convolutional neural networks for SERS analysis of biomarkers in medical diagnostics.* J Raman Spectrosc, 2022. **53**(12): p. 2044-2057.

## Appendix

### A.1 Example Code for Large Scale Fresnel Simulations

This code was written in R and can be used for large scale Fresnel calculations. It requires refractive indexes for the materials of interest over the wavelength selected. Fitting is performed ahead of time to solve the equations of the refractive indexes. This data will calculate the sensitivities for a variety of wavelengths and thicknesses of a selected material. In the process the plasmonic curves will also be determined.

```
packages = c("writexl","plyr")

## Now load or install&load all

package.check <- lapply(

  packages,

  FUN = function(x) {

    if (!require(x, character.only = TRUE)) {

      install.packages(x, dependencies = TRUE)

      library(x, character.only = TRUE)

    }

  }

)
```

```
angleslist = (read.csv("angles.csv", header = TRUE))

angles <- (angleslist)

Angle = angles*(180/pi)

Thickness = seq(15,100,.5)

finalslopedata2 = data.frame(1)

for (number in seq(1,1900,1)){

finalslopedata2add = number

finalslopedata2 = cbind(finalslopedata2,finalslopedata2add)

}

finalsensidata = data.frame(1)

RIlist = read.csv("RIs.csv" , header = TRUE)

RIs <- (RIlist)

for (alox in seq(15,100,.5)){

  finaldata = data.frame(Angle)

  finalmindata = data.frame(1)

  for (x in seq(650,650,.5)){

    for (RI in seq(1.333,1.342,.003)){
```

```
k0 = pi/(x)

n2 = -2.58398831E-16*(x)^6 + 1.21889598E-12*(x)^5 - 2.23625478E-09*(x)^4 +
2.01168212E-06*(x)^3 - 9.23109586E-04*(x)^2 + 2.06035486E-01*(x) -
1.72850081E+01

k2 = -6.40631981E-17*(x)^6 + 2.18495660E-13*(x)^5 - 2.32544679E-10*(x)^4 +
5.07210538E-08*(x)^3 + 4.40788366E-05*(x)^2 - 9.96258026E-03*(x) +
2.52441859E+00

k3 =  -3.8241746E-17*(x)^6 + 2.3737886E-13*(x)^5 - 5.8454572E-10*(x)^4 +
7.2129006E-07*(x)^3 - 4.5999094E-04*(x)^2 + 1.3764291E+01*(x) - 1.3359111E+01

n3 =  1.7079390E-17*(x)^6 - 1.2009652E-13*(x)^5 + 3.4148543E-10*(x)^4 -
4.9932119E-07*(x)^3 + 3.9189581E-04*(x)^2 - 2.06035486E+01*(x) +
1.72850081E+01

 for (angle in angles){

  #polarization = TM

  n1 <- 1.456

  k1 <- 0

  N1 = complex(re=n1,im=k1)

  sin1 <- complex(re=sin(angle), im=0)

  cos1 <- (sqrt(1-(sin1^2)))
```

```
epsilon1.1 = ((n1)^2)-((k1)^2)

epsilon2.1 = 2*n1*k1

epsilon3.1 = complex(re=epsilon1.1,im=epsilon2.1)

k1 = (N1*k0*(cos1))

thick1 <-0

N2 = complex(re=n2,im=k2)

sin2 = (sin1*N1)/N2

cos2 <- (sqrt(1-(sin2^2)))

epsilon1.2 = ((n2)^2)-((k2)^2)

epsilon2.2 = 2*n2*k2

epsilon3.2 = complex(re=epsilon1.2,im=epsilon2.2)

k2 = (N2*k0*cos2)

thick2 <- 13

N3 = complex(re=n3,im=k3)

sin3 = (sin1*N1)/N3

cos3 <- (sqrt(1-(sin3^2)))

epsilon1.3 = ((n3)^2)-((k3)^2)
```

```
epsilon2.3 = 2*n3*k3

epsilon3.3 = complex(re=epsilon1.3,im=epsilon2.3)

k3 = (N3*k0*cos3)

thick3 <- alox

n4 <- RI

k4 <- 0

N4 = complex(re=n4,im=k4)

sin4 = (sin1*N1)/N4

cos4 <- (sqrt(1-(sin4^2)))

epsilon1.4 = (( n4)^2)-((k4)^2)

epsilon2.4 = 2*n4*k4

epsilon3.4 = complex(re=epsilon1.4,im=epsilon2.4)

k4 = (N4*k0*cos4)

thick4 <- 0

r12 = ((k1/epsilon3.1-k2/epsilon3.2)/((k1/epsilon3.1)+(k2/epsilon3.2)))

r23 = ((k2/epsilon3.2-k3/epsilon3.3)/((k2/epsilon3.2)+(k3/epsilon3.3)))

r34 = ((k3/epsilon3.3-k4/epsilon3.4)/((k3/epsilon3.3)+(k4/epsilon3.4)))
```

```
        layer2 = exp(complex(re=0, im=4)*k2*complex(re=thick2,im=0))

        layer3 = exp(complex(re=0, im=4)*k3*complex(re=thick3,im=0))

        layer4 = exp(complex(re=0, im=4)*k4*complex(re=thick4,im=0))

        r123 = (r12+(r23*layer2))/((complex(re=1,im=0)+(r12*r23*layer2)))

        r234 = (r23+(r34*layer3))/((complex(re=1,im=0)+(r23*r34*layer3)))

        r1234.1 = (r12+r234*layer2)

        r1234.2 = (complex(re=1,im=0)+(r12*r234*layer2))

        r1234.3 = (r1234.1/r1234.2)

        rconj = ((Conj(r1234.3)))

        reflection = (r1234.3*rconj)

        reflectionabs = abs(reflection)

        angledegree = angle*(180/pi)

        alldata <- data.frame(reflectionabs)

        finaldata <- cbind2(finaldata, alldata)

      }

   }

}
```

```
write.csv(finaldata, "results.csv")

compileddata = (read.csv("results.csv", header = TRUE))

for (column in seq(3,7606,1)){

  spectra = compileddata[, c(column)]

  minimum <- 49.95+.05*which.min(spectra)

  mindata <- data.frame(minimum)

  finalmindata <-cbind2(finalmindata, mindata)



}

  write.csv(finalmindata, "minresults.csv")

 mindata =(read.csv("minresults.csv"))

 finalslopedata = data.frame(1)

for (column2 in seq(3,7602,4)){

  mini = unlist(mindata[, c(column2,column2+1,column2+2,column2+3)])

  refractiveindex <- c(1.333,1.336,1.339,1.342)

  minimums <- c(mini)
```

```
    mod <- lm(minimums ~ refractiveindex)
    slope <- coef(mod)[2]
    slopedata <- data.frame(slope)
    finalslopedata <- cbind2(finalslopedata, slopedata)
  }
  names(finalslopedata2) <- names(finalslopedata)
  finalslopedata2 <- rbind2(finalslopedata2, finalslopedata)
}
write.csv(finalslopedata2, "auresults.csv")
```

**A2. Terahertz Simulations and Chip Fabrication**

Terahertz simulations were performed as a possible alternative plasmonic material for sensing purposes. The sensor chips were designed to take advantage of the far-IR capabilities of commercial FTIR instruments, while also having a unique THz microstructure design. All simulations for this were performed using CST studio.

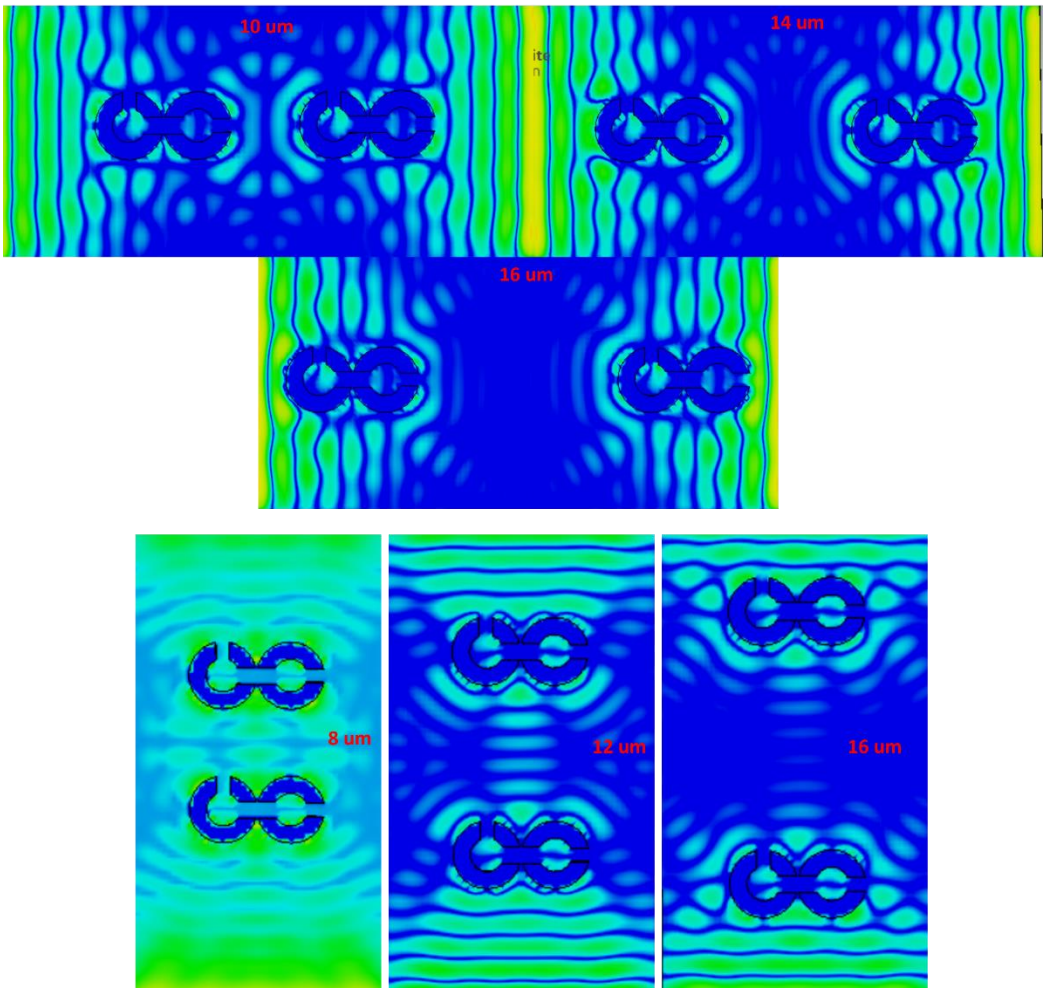


**Figure A2.1** Structural simulation of the "UC" chip, as dual split ring resonators are optimal for THz response.

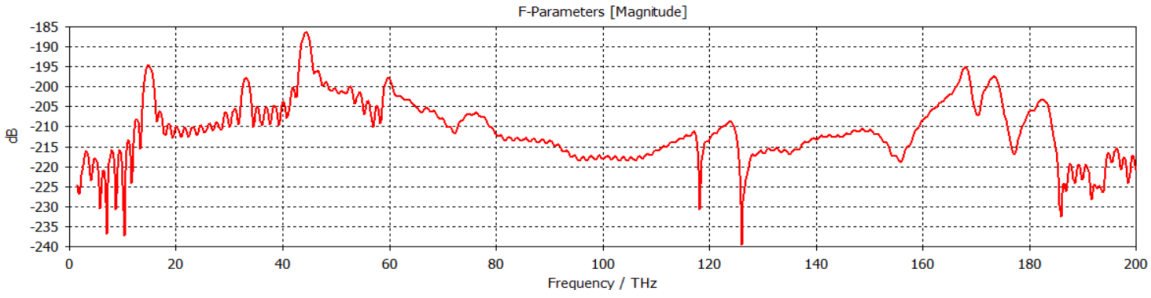


**Figure A2.2** Spectral response of the UC chip with noted areas of high absorption.

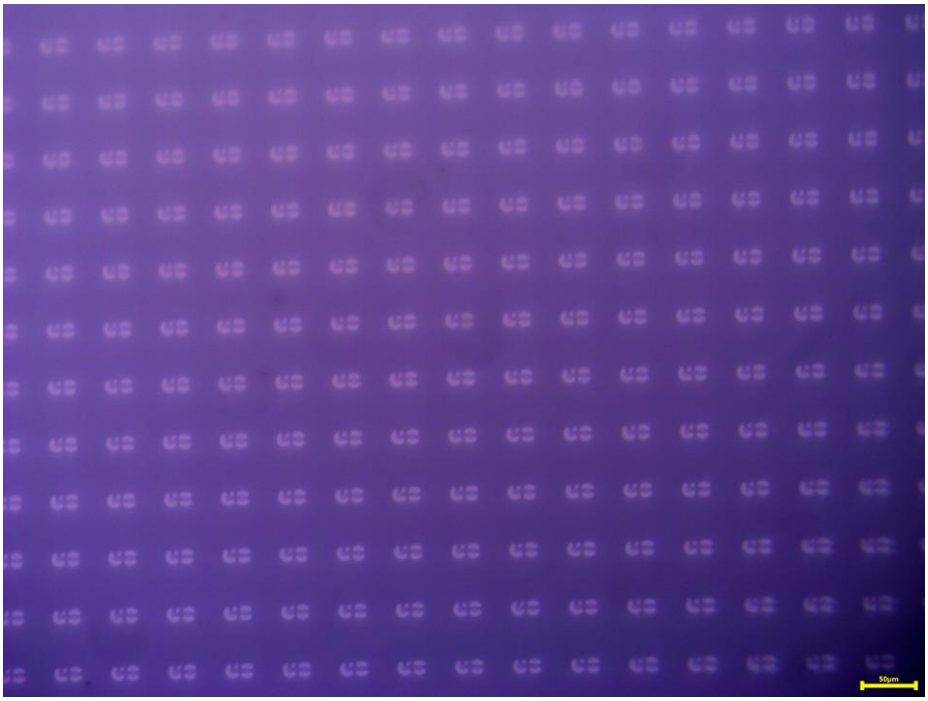

**Figure A2.4** Fabricated UC chips based upon the specifications simulated.